



University of Kentucky
UKnowledge

Theses and Dissertations--Physics and
Astronomy

Physics and Astronomy

2023

Design of the Highly Uniform Magnetic Field and Spin-Transport Magnetic Field Coils for the Los Alamos National Lab Neutron Electric Dipole Moment Experiment

Jared Brewington

University of Kentucky, jaredbrewington94@gmail.com

Author ORCID Identifier:

 <https://orcid.org/0000-0001-7061-1358>

Digital Object Identifier: <https://doi.org/10.13023/etd.2023.226>

[Right click to open a feedback form in a new tab to let us know how this document benefits you.](#)

Recommended Citation

Brewington, Jared, "Design of the Highly Uniform Magnetic Field and Spin-Transport Magnetic Field Coils for the Los Alamos National Lab Neutron Electric Dipole Moment Experiment" (2023). *Theses and Dissertations--Physics and Astronomy*. 113.

https://uknowledge.uky.edu/physastron_etds/113

This Doctoral Dissertation is brought to you for free and open access by the Physics and Astronomy at UKnowledge. It has been accepted for inclusion in Theses and Dissertations--Physics and Astronomy by an authorized administrator of UKnowledge. For more information, please contact UKnowledge@lsv.uky.edu.

STUDENT AGREEMENT:

I represent that my thesis or dissertation and abstract are my original work. Proper attribution has been given to all outside sources. I understand that I am solely responsible for obtaining any needed copyright permissions. I have obtained needed written permission statement(s) from the owner(s) of each third-party copyrighted matter to be included in my work, allowing electronic distribution (if such use is not permitted by the fair use doctrine) which will be submitted to UKnowledge as Additional File.

I hereby grant to The University of Kentucky and its agents the irrevocable, non-exclusive, and royalty-free license to archive and make accessible my work in whole or in part in all forms of media, now or hereafter known. I agree that the document mentioned above may be made available immediately for worldwide access unless an embargo applies.

I retain all other ownership rights to the copyright of my work. I also retain the right to use in future works (such as articles or books) all or part of my work. I understand that I am free to register the copyright to my work.

REVIEW, APPROVAL AND ACCEPTANCE

The document mentioned above has been reviewed and accepted by the student's advisor, on behalf of the advisory committee, and by the Director of Graduate Studies (DGS), on behalf of the program; we verify that this is the final, approved version of the student's thesis including all changes required by the advisory committee. The undersigned agree to abide by the statements above.

Jared Brewington, Student

Dr. Brad Plaster, Major Professor

Dr. Christopher Crawford, Director of Graduate Studies

Design of the Highly Uniform Magnetic Field and Spin-Transport Magnetic Field
Coils for the Los Alamos National Lab Neutron Electric Dipole Moment Experiment

DISSERTATION

A dissertation submitted in partial
fulfillment of the requirements for
the degree of Doctor of Philosophy
in the College of Arts and Sciences
at the University of Kentucky

By
Jared Brewington
Lexington, Kentucky

Director: Dr. Brad Plaster, Professor of Physics
Lexington, Kentucky 2023

Copyright© Jared Brewington 2023
<https://orcid.org/0000-0001-7061-1358>

ABSTRACT OF DISSERTATION

Design of the Highly Uniform Magnetic Field and Spin-Transport Magnetic Field Coils for the Los Alamos National Lab Neutron Electric Dipole Moment Experiment

Charge-Parity (CP) violation is one of Sakharov's three conditions which serve as guidelines for the generation of a matter-antimatter asymmetry in the early universe. The Standard Model (SM) of particle physics contains sources of CP violation which can be used to predict the baryon asymmetry. The observed baryon asymmetry is not predicted from SM calculations, meaning there must be additional sources of CP violation beyond the Standard Model (BSM) to generate the asymmetry. Permanent electric dipole moments (EDMs), which are inherently parity- and time reversal-violating, present a promising avenue for the discovery of new sources of CP violation to resolve this outstanding problem. The SM prediction for the neutron EDM, for example, is multiple orders of magnitude smaller than the sensitivity achieved by modern neutron EDM experiments [1]. The measurement of a non-zero neutron electric dipole moment larger than the SM prediction would be a sure sign of BSM CP violation. A experiment searching for the neutron EDM at Los Alamos National Lab (LANL) has been constructed with the goal of improving the current neutron EDM upper limit $d_n < 1.8 \times 10^{-26} e\text{-cm}$ (90% CL) [2] by approximately one order of magnitude. The work presented in this thesis has been performed in support of the LANL-nEDM experimental effort.

Precise magnetic field control is required to reach the desired measurement sensitivity, specifically a highly uniform B_0 holding magnetic field. A multiple-split solenoid with an octagonal cross section was designed and fabricated to meet the gradient specification $\langle |\partial B_z / \partial z| \rangle < 0.3$ nT/m and address engineering challenges related to assembly and magnetometry. Efficient transport of neutron polarization from the polarizing magnet to the storage cells is also essential to accomplish the sensitivity goal. A series of modified, self-shielding $\cos \theta$ coils have been designed to maximize polarization as neutrons propagate through penetrations in the magnetically shielded room. The spin-transport coils, in conjunction with the simultaneous spin analyzers, will provide a polarization product $\alpha > 0.8$. The series of coils interfaces with the B_0 coil in a pseudo-continuous manner such that the fringe fields do not cause depolarization of the neutrons and do not generate non-uniformities in the storage cell volumes.

KEYWORDS: neutron, electric dipole moment, magnetic field, spin-transport, coil design

Author's signature: Jared Brewington

Date: May 2, 2023

Design of the Highly Uniform Magnetic Field and Spin-Transport Magnetic Field
Coils for the Los Alamos National Lab Neutron Electric Dipole Moment Experiment

By
Jared Brewington

Director of Dissertation: Dr. Brad Plaster

Director of Graduate Studies: Dr. Christopher Crawford

Date: May 2, 2023

Dedicated to my wife Eden and my parents, Scott, Denise, Dean, and Jo Ann.

ACKNOWLEDGMENTS

First and foremost, I would like to thank my advisor, Dr. Brad Plaster, for his support and guidance throughout my graduate career. Although his time as my advisor has come to an end, he will continue to be a professional mentor and trusted friend.

Thank you to my thesis committee for your guidance throughout my research and during the writing of this dissertation: Dr. Susan Gardner, Dr. Christopher Crawford, and Dr. Alexandre Martin.

Thank you to my collaborators for the LANL-nEDM experiment, especially Dr. Steven Clayton. Steven served as my host during my SCGSR award period at LANL, for which I am very grateful.

Thank you to my fellow research group members for providing a necessary support system. I am most thankful for the insights, collaborative effort, and friendship of Lakshya Malhotra and Amara Palamure.

Thank you to my family for supporting me through this challenging time. I cannot imagine attempting to accomplish such a feat without having my family behind me. A special thank you to my wife, Eden, who has been patient and always believed in me. I could not ask for a better partner in life.

This material is based upon work supported by the U.S. Department of Energy, Office of Science, Office of Nuclear Physics, under Award Number DE-SC0014622, the NSF under Award Number PHY-1828568, the LANL LDRD program, and by the U.S. Department of Energy, Office of Science, Office of Workforce Development for Teachers and Scientists, Office of Science Graduate Student Research (SCGSR) program. The SCGSR program is administered by the Oak Ridge Institute for Science and Education for the DOE under contract number DE-SC0014664.

TABLE OF CONTENTS

Acknowledgments	iii
Table of Contents	iv
List of Figures	v
List of Tables	xi
Chapter 1 Introduction	1
1.1 Fundamental Symmetries	1
1.2 Theoretical Motivation for the Neutron EDM Search	5
Chapter 2 The LANL-nEDM Experiment	10
2.1 Measuring the Neutron Electric Dipole Moment	10
2.2 LANL-nEDM Apparatus and Experimental Cycle	18
2.3 Statistical Uncertainty and Sytematic Effects	25
Chapter 3 Highly Uniform B_0 Coil	31
3.1 B_0 Coil Design	31
3.2 Magnetic Field Optimization	35
3.3 Tolerances	41
3.4 Novel Features and Prototyping	49
Chapter 4 Spin-Transport Coils	55
4.1 Spin-Transport Magnetic Field	55
4.2 Spin-Transport Coil Design	57
4.3 Spin-Transport Efficiency Simulation	66
4.4 Prototype coils	74
Chapter 5 Conclusion	79
Appendices	80
Appendix A	80
Appendix B	82
Bibliography	84
Vita	91
Personal Information	91
Educational Institutions	91
Professional Positions	91

LIST OF FIGURES

1.1	The upper limits of the neutron EDM for various experiments. This plot is adapted from T. Ito (personal communication). Also shown are theoretical predictions of the neutron EDM magnitude from the Standard model and two BSM theories [31].	9
2.1	Visualization of the energy splitting due to the neutron magnetic moment and EDM coupling to parallel (\uparrow) and anti-parallel (\downarrow) magnetic and electric fields. [33]	10
2.2	An example Rabi fringe pattern for the case where $\gamma_n B_1 = 1 \text{ s}^{-1}$ (see Eq. 2.21). The x-axis shows the frequency of the oscillating \vec{B}_1 field normalized to the Larmor frequency associated with the \vec{B}_0 excitation field, $\omega_0 = \gamma_n B_0$. The y-axis represents the number of neutrons in the spin-up state N_+ compared to the total number of neutrons $N = N_+ + N_-$ after the application of a π pulse. A resonance is observed at $\omega = \omega_0$. . .	15
2.3	Diagram of Ramsey’s method of separated oscillatory fields. A static field B_0 is applied in the vertical direction, but is not shown in the image. The sinusoidal wave shown on the right represents a reference clock, which is used to apply an oscillating voltage to the coil producing the B_1 field during the two spin-flip pulses. Note that the clock is continuous and coherent throughout the sequence which allows a phase difference between the clock and neutron spin to accumulate during the free precession time. [37]	16
2.4	Plots showing the probability of a neutron transitioning the excited state after the application of Ramsey’s method of separated oscillatory fields. The following assumptions are used: the neutron is initially in the ground state, 50 second free precession period, $ \vec{B}_1 $ is chosen for 2 second $\pi/2$ pulse duration, and $ \vec{B}_0 = 1 \mu\text{T}$. The left plot contains Ramsey fringes over a wide range of normalized frequencies. The right plot show the fringes over a much smaller range so that the structure of the fringes near $\omega = \omega_0$ can be seen clearly.	17
2.5	CAD model of the UCN experimental hall at LANL from [38]. The LANL-nEDM experimental setup is shown on the left side of the image. The neighboring experiments measure the free neutron lifetime (UCN τ) and the neutron β -decay parameter A_0 (UCNA) [39],[40].	19
2.6	Picture of the 5 T superconducting solenoidal polarizing magnet to be used in the LANL-nEDM experiment. [41]	21
2.7	CAD model of the LANL-nEDM magnetically shielded room (MSR). The rendering shows the MSR in the “open” orientation, i.e. the door is removed. The B_0 coil is positioned inside of the MSR, shown with blue-colored panels.	23

3.1	CAD renderings showing the B_0 coil in a 3D view to give perspective of the octagonal shape (TOP) and a 2D view with the labels for gaps and coil sections (BOTTOM).	32
3.2	CAD models of the LANL MSR and the B_0 coil. The LEFT image shows the North side of the MSR, which includes the penetrations corresponding to the neutron guide locations, magnetometry, etc. The RIGHT image shows the interior of the MSR with the B_0 coil in place. In this view, one can see how the placement and dimension of each coil section accommodates the various penetrations.	33
3.3	Color map of $ \vec{B} $ of a large solenoid housed inside the LANL-nEDM MSR. The 2D cross section shown is the $y = 0$ plane. The coil height and diameter are 2.3 m. The volume averaged magnitude of the vertical gradient of the B_z component in the UCN storage volume is $1 \mu\text{T}$ is $\langle \partial B_z / \partial z \rangle = 8.39 \text{ nT/m}$. Note: The gradient calculation is normalized to a central field magnitude $ B_0 = 1 \mu\text{T}$	35
3.4	This set of images shows magnetic flux lines from a solenoid (a), gapped solenoid (b), and double-gapped solenoid (c) calculated using a 2D axis-symmetric finite element simulation—the left side of each image being the axis of symmetry. The green in each image represents the current density oriented into the page. Note that the solenoid field diverges as distance from the center increases. On the other hand, the gapped solenoid field lines converge, up to some point, moving away from the center of the system. Thus, the linear combination of these two fields, given that their magnitudes are approximately equal, will produce straighter flux lines near the center of the system. This effect is represented in (c), where the field is produced by the combination of the solenoid and gapped solenoid coils.	37
3.5	Simplified COMSOL model of B_0 and the LANL-nEDM MSR used for optimization of the B_0 coil parameters. This simplified geometry does not include penetrations in the B_0 coil faces or the MSR walls. Without these penetrations, the system has a $\pi/4$ rotational symmetry about the z axis and a mirror symmetry about the $z = 0$ plane. In this case the system can be simulated in just one octant with the application of proper boundary conditions.	38
3.6	Color maps of fractional change in $ \vec{B} $ from the central value $ B_0 = 1 \mu\text{T}$ produced by the optimized B_0 coil within the LANL-nEDM MSR. The top image shows a plot of the field profile with a scale of $\pm 5\%$. The bottom image shows a plot of the same values with a smaller scale: $\pm 0.1\%$	39
3.7	Table of gradients extracted from the optimized B_0 COMSOL model.	40
3.8	Plot of $\langle \partial B_z / \partial z \rangle$ normalized to the central value of \vec{B}_0 for different current ratios. The dashed red line represents the upper limit of the gradient specification $\langle \partial B_z / \partial z \rangle < 0.3 \text{ nT/m}$. The gradient produced by the modeled B_0 coil design satisfies the gradient specification for the range of current ratios $1.814 \leq I_{out} / I_{in} \leq 1.828$	42

3.9	Plots showing the \vec{B} field profile in a $y = 0$ cross section of the upper UCN storage cells for current ratios 1.81, 1.82, and 1.83 (from TOP to BOTTOM). Since the model is symmetric across $z = 0$, one can infer the field behavior in the lower cell. The color map shows fractional change from the central $ \vec{B} $ value. The vector plots show \vec{B} projected onto the $y = 0$ plane. The z component of the vectors has been scaled by 10^{-4} to visualize the divergence/convergence of the fields. The optimal current ratio 1.82 is tuned such that there is very little deviation in the B_x component of the vector plot.	43
3.10	Plot of volume averaged magnitude of fractional B_z vertical gradient versus vertical offset of the B_0 coil. Note that the vertical offset on the x -axis is applied to all the B_0 coil sections. The dashed red line represents the upper limit of the gradient specification. The gradient specification is satisfied for offsets up to 0.25 mm.	45
3.11	Color maps showing effect of vertical offsets on the B_0 field profile. The offset listed in each plot title is applied to the z position of the B_0 coil sections. Note that larger offsets result in larger field variation across the cell volumes, represented by the small rectangles at the center of each plot.	46
3.12	Plot of volume averaged magnitude of fractional B_z vertical gradient versus relative permeability μ_r of the MSR layers. The gradient specification $\langle \partial B_z / \partial z \rangle < 0.3$ nT/m—the upper limit of which is shown by the dashed red line—is satisfied for the range of permeability $21800 < \mu_r < 50900$. This analysis was performed without adjustment of current ratio from the nominal value $I_{out}/I_{in} = 1.82$	48
3.13	CAD renderings of the B_0 coil frame and coil. The system is shown standalone (LEFT) and in the MSR (RIGHT).	50
3.14	Picture of the full-scale B_0 coil assembled in the MSR at LANL.	51
3.15	Picture of the half-scale prototype B_0 coil.	52
3.16	Pictures of the half-scale prototype coil in the small MSR at LANL [63].	53
3.17	CAD rendering of the H-frame mapper and the half-scale B_0 . The mapper allows motion of the carriage (shown at the center of the image) along the rail spanning the coil width. This rail is translated perpendicular to its length via synchronous actuation of stepper motors and a timing belt-pulley system (not pictured).	54
3.18	Plots of B_z from the half-scale B_0 prototype field along the axis of the coil. The magnitude of the magnetic field produced by the prototype coil is $ B_0 \approx 2.9 \mu\text{T}$. LEFT: Holding the shim current constant (100 mA), the B_0 outer to inner current ratio is swept to find the minimum second order gradient. RIGHT: At the optimal current ratio of 1.71, the shim current is swept to produce the highest uniformity—i.e. the smallest gradient. The optimal shim current is between 105 mA and 110 mA.	54
4.1	Plot of the maximum value of $ \vec{B} $ in the field taper versus step size in the numerical integration. $ \vec{B} $ is given by numerical integration of Eq. 4.3 for $\kappa = 32$	57

4.2	LEFT: Plot of the magnetic field magnitude given by the field taper between the ambient magnetic field and the B_0 magnetic field. The field taper gradient corresponds to an adiabatic parameter value $\kappa = 32$. A polynomial fit was performed to provide a functional form for the field taper. The value of the fit at discrete locations is plotted on top of the field taper. RIGHT: Plot of the residuals from the aforementioned polynomial fit.	58
4.3	Image of spin-transport coil winding pattern. The coils are as follows: A (black), B(blue), C (red), D (green). The winding pattern is symmetric across the symmetry plane used to divide the cylindrical shell in half. The number of wires shown for each coil is a subset of the total number of wires used since the wire density becomes too high to distinguish detail. .	60
4.4	Contour plot of the magnetic field magnitude in the interior volume of two adjacent coils of the transport system, namely coil B and coil C. The color scale is logarithmic. The contours are nearly vertical, signifying that the magnitude of the field at a given x position is approximately constant, which is consistent with the design objective. The interface between coil B and coil C is located at $x = 1.65$ m. The contours in this region show more noticeable curvature due to the perturbation introduced by the interface. .	62
4.5	Winding pattern (isocontours) of Coil A in COMSOL. The color scale shows the value of the scalar potential.	64
4.6	TOP: COMSOL combined B_0 and spin-transport coil geometry, rendered as a wire frame in one octant. The storage cell volume, B_0 surfaces, and the MSR layers are clearly visible. The high wire density in the spin-transport coils makes it difficult to distinguish winding pattern detail. BOTTOM: Magnetic field magnitude on the $y = 0$ plane generated using the COMSOL model shown above.	65
4.7	Plot comparing field profile generated by COMSOL versus the polynomial field taper. The spin transport coils are positioned between $x = 1.15$ m and $x = 1.90$ m. The designed field taper and COMSOL field are in good agreement up to $x = 1.85$ m. The spin-transport field profile deviates from the designed field taper due to the leakage field from the uncompensated, open end cap of coil D. Since the gradient of the modeled field is less than the polynomial gradient at this deviation, the value of the adiabatic parameter κ would be larger, but the length required to reach the ambient field magnitude is extended.	66
4.8	Show winding pattern of single layer spin-transport system where the effect of the MuMetal on the winding pattern can be seen.	66
4.9	Plot of $ B $ generated by COMSOL on the $y = 0$ plane. This COMSOL model contains a previous iteration of the B_0 and spin-transport coil designs. This plot illustrates the spin-transport field at the MuMetal surface due to the single layer (i.e. not self-shielding) spin-transport coil design. The leakage field around the spin-transport coils should be compared to Fig. 4.6, which plots the same cross section for the modified double $\cos \theta$ spin-transport design.	67

4.10	Plot of the magnetic field magnitude in the spin-transport coil region on the $y = 0$ plane. The color scale is logarithmic. The double $\cos \theta$ coil design is not perfectly self-shielding, as seen by the non-zero field outside of the surface, but, in general, the magnitude of the leakage field is order of magnitude smaller than the nominal applied field inside the coil volume. Local increases in leakage field exist at $x \approx 1.65$ m and $x \approx 1.9$ m. The source of the larger leakage field is the 0.5 mm gap between adjacent coils.	68
4.11	Geometry in PENTrack simulation.	69
4.12	Histogram of initial neutron velocities from PENTrack.	70
4.13	Histogram showing the z -component of the simulated neutron spin vector from Phase 2. Only the detected neutrons are shown in the histogram, and S_z is recorded when the neutrons contact the detector volume.	72
4.14	The plots represent two individual neutrons simulated during Phase 1: particle 2 (LEFT) and particle 13 (RIGHT). These two particles were chosen to show some representative behavior of the simulated neutrons. The top two plots show the x position of the simulated neutron during the full simulation time. The bottom two plots are scatter plots of the spin alignment of the neutron with the magnetic field. The color represents time with $t = 0$ being dark blue and t_{end} being dark red.	72
4.15	These images show the prototype modified $\cos \theta$ coil used to validate the design and fabrication techniques used for the spin-transport coils. The coil was wound using 20 gauge magnet wire placed in grooves to ensure precise placement. The coil was printed in quarters, divided into 90 degree sections. The left image features a misalignment of the upper most quadrant to illustrate the coil construction—note the resulting discontinuity in the groove pattern. In the right picture, a kink in the groove pattern is visible near the mid-plane of the cylinder. The source of the kink is the boundary condition enforced by the presence of a MSR shielding layer in the COMSOL model used to generate the winding pattern.	75
4.16	Plot of B_z along the axis of the prototype modified $\cos \theta$ coil shown in Fig. 4.15. The blue points are measurements of B_z collected via translation of a fluxgate magnetometer. The black line represents the expected result extracted from the COMSOL model of the prototype coil. The physical coil field profile is consistent with the COMSOL prediction.	76
4.17	Plot of the double $\cos \theta$ prototype coil magnetic field magnitude [74]. The magnitude of the field along the coil axis (Red) is large compared to the field magnitude along a line parallel to the coil axis and 1 cm outside of the coil surface (Blue). The ratio of these two plots is the “self-shielding” factor of the coil. The average self-shielding factor from $z = -10$ cm to $z = 10$ cm is 181.	76

4.18	Plots of the magnetic field components near the spin-transport interface [74]. The vertical green lines centered around $z = 10$ cm represent the region spanned by the spin-transport diameter. The red scatter plot is the magnetic field from the stand-in B_0 coil. The blue scatter plot is the magnetic field from the B_0 and spin-transport coil system. The flux-gate magnetometer was translated parallel to the spin-transport interface surface with a 2 cm displacement from the coil surface.	77
4.19	Example 3D coil object produced using the “Printable-coil” python algorithm [75].	78

LIST OF TABLES

1.1	Transformations of physical quantities under C, P, and T operations [10].	2
2.1	A summary of energetic properties of UCNs relevant to the LANL-nEDM experiment.	20
2.2	Expected statistical sensitivity of the LANL-nEDM experiment [41]. T_{cycle} takes into account the time for loading, unloading, free precession period, and dead time associated with a single measurement. It should be noted that the times for achieving the sensitivities are live days/years. Given the operational schedule of the linear accelerator and other considerations, one live year of data taking will take approximately 5 calendar years. . .	25
2.3	Systematic errors reported in the 2020 updated analysis of the ILL neutron EDM experiment [2]. The units of the effects are 10^{-28} e-cm.	26
2.4	The expected experimental parameters for the LANL-nEDM experiment [41]. These values are estimated from previous experimental work in the field [2] [42] as well as research and development conducted at LANL. Note: $\omega_r \equiv \frac{v_\phi}{\rho}$	28
3.1	List of the optimized coil parameters for the B_0 coil. These values were established using parameter sweeps in COMSOL to minimize the volume averaged gradient magnitude $\langle \partial B_z / \partial z \rangle$ in the UCN storage cells. The listed coil section positions correspond to the minimum z position of the section. Only the sections located on the upper half of the coil are shown; the lower section parameters can be derived using mirror symmetry across the $z = 0$ plane.	40
3.2	Table of offsets for each B_0 coil section in mm and the modeled gradient from a design with those offsets applied in nT/m. The nominal design case does not have any position offsets. The offsets are selected at random from a uniform distribution $[-1, 1]$ mm and rounded to the nearest 0.1 mm. Note that Ex. 1 does not meet the gradient specification $\langle \partial B_z / \partial z \rangle < 0.3$ nT/m.	47
4.1	Coefficients of the polynomial fit for the field taper. The degree 10 polynomial provided residual on the order of 1% (see Fig. 4.2). Important to note that the range of this fit is $x = [-0.75, 0]$ where the $1.1 \mu\text{T}$ field magnitude occurs at $x = 0.75$ m.	58
4.2	Dimensions of the four spin transport coils. All four coils have the same inner and outer radii: $R_{inner} = 0.0533$ m and $R_{outer} = 0.0661$ m. See Fig. 4.3 for a visualization of the coil geometry. The relative current values are normalized to the current in coil D. The absolute current values will be tuned to give optimal polarization transport using measurements of polarized UCN on the LANL UCN beamline.	60

Chapter 1 Introduction

The possibility of nonzero permanent electric dipole moments (EDMs) for particles and nuclei was first considered by Purcell and Ramsey in 1950 [3]. The first upper limit of the neutron EDM was $3 \times 10^{-18} e \cdot \text{cm}$, extracted from neutron-electron scattering data published by Haven, Rabi, and Rainwater [4]. Direct searches for a non-zero neutron EDM began in 1951 when Smith, Purcell and Ramsey used a neutron beam method to establish a new upper limit of $5 \times 10^{-20} e \cdot \text{cm}$ [5]. The experiment served as a test of parity and time reversal symmetries, which were considered to be universally conserved at the time. Since the measurement was consistent with zero, and thus consistent with the prevailing notion that parity is indeed conserved, the experimental result was not immediately published [5]. No further progress was made on the neutron EDM measurement until the discovery of parity violation in nuclear beta decay by Wu et al. in 1957 [6], following from an earlier theoretical work proposing that parity may be violated in the weak interaction [3, 7]. Smith, Purcell and Ramsey proceeded to publish their earlier result as the neutron EDM now represented a potential avenue for further exploration of discrete symmetry violation. The neutron EDM search continues to this day, with many methodological and technological advancements leading to the current upper limit of $1.8 \times 10^{-26} e \cdot \text{cm}$ [2]. A broad complementary program on searches for a permanent EDM of the electron is ongoing [8].

This thesis will focus on a neutron EDM experiment that will be conducted at Los Alamos National Laboratory (LANL). Chapter 1 will serve as an introduction to the theoretical background and properties of the neutrons used for modern neutron EDM measurement efforts. Chapter 2 will be an overview of various experimental techniques employed in the LANL neutron EDM (LANL-nEDM) design and systematic errors related to magnetic field control. Chapter 3 will discuss efforts in the design and fabrication of the B_0 coil which provides the uniform holding magnetic field for the LANL-nEDM experiment. Chapter 4 will present coil designs for the spin-transport coils, which maintain neutron polarization, and the B_1 coil, which provides the oscillatory field for the $\pi/2$ pulse, as well as the associated magnetic field design methods. Chapter 5 will present an analysis of the magnet coil system based on spin-tracking particle simulations.

1.1 Fundamental Symmetries

A symmetry is an operation that, when performed on a system, results in a configuration which is indistinguishable from the original. Physicists use symmetries to predict and understand the behavior of physical systems. Perhaps the most famous instance is Noether's Theorem [9]: every differentiable symmetry of a system has a corresponding conservation law, and every conservation law reflects an underlying symmetry. As an example, suppose a system is symmetric under continuous rotations (i.e. the Lagrangian of the system is unchanged). The system must behave in a

manner which results in the conservation of angular momentum. Noether's theorem does not apply to discrete symmetries; however, discrete symmetries play an important role in the Standard Model (SM) of particle physics. Charge-conjugation (C), parity (P), and time-reversal (T) symmetry are discrete symmetries that describe the fundamental forces of the SM. Understanding C, P, and T violation within the SM, and possibly beyond, is a rich area of research in modern-day physics. The details of each symmetry, as well as their connection with the neutron EDM, will be discussed in the following sections.

Table 1.1: Transformations of physical quantities under C, P, and T operations [10].

	C	P	T
position	$\vec{x} \rightarrow \vec{x}$	$\vec{x} \rightarrow -\vec{x}$	$\vec{x} \rightarrow \vec{x}$
momentum	$\vec{p} \rightarrow \vec{p}$	$\vec{p} \rightarrow -\vec{p}$	$\vec{p} \rightarrow -\vec{p}$
energy	$\epsilon \rightarrow \epsilon$	$\epsilon \rightarrow \epsilon$	$\epsilon \rightarrow \epsilon$
angular momentum	$\vec{J} \rightarrow \vec{J}$	$\vec{J} \rightarrow \vec{J}$	$\vec{J} \rightarrow -\vec{J}$
spin	$\vec{s} \rightarrow \vec{s}$	$\vec{s} \rightarrow \vec{s}$	$\vec{s} \rightarrow -\vec{s}$
charge	$Q \rightarrow -Q$	$Q \rightarrow Q$	$Q \rightarrow Q$
electric field	$\vec{E} \rightarrow -\vec{E}$	$\vec{E} \rightarrow -\vec{E}$	$\vec{E} \rightarrow \vec{E}$
magnetic field	$\vec{B} \rightarrow -\vec{B}$	$\vec{B} \rightarrow \vec{B}$	$\vec{B} \rightarrow -\vec{B}$

Charge-Conjugation

C is a transformation that replaces particles with their corresponding antiparticles. The operation is accomplished by reversing the sign of all the internal quantum numbers such as electric charge, lepton number, and strangeness [11].

$$C |p\rangle = |\bar{p}\rangle$$

When C is applied to a particle state twice, the result is the original state as shown in Eq. 1.1.

$$\begin{aligned}
 C^2 |p\rangle &= C(C |p\rangle) \\
 &= C |\bar{p}\rangle \\
 &= |p\rangle \\
 \implies C^2 &= I
 \end{aligned}
 \tag{1.1}$$

Therefore the eigenvalues of C are ± 1 . The implication is that a particle state $|p\rangle$ that is an eigenstate of C must be equivalent to its antiparticle state $|\bar{p}\rangle$ (within a sign), meaning eigenstates of C are the subset of particles which are their own antiparticles. All internal quantum numbers for such particles must be zero since the application of C (i.e. changing the signs of the quantum numbers) does not change the state. Although C symmetry is not directly tested by neutron EDM experiments, C is relevant due to its relationship with the other discrete symmetries. Violation of C symmetry plays a key role in the Sakharov conditions (see subsection 1.2). Table 1.1 has examples showing how various physical observables transform under C.

Parity

P is an inversion of all spatial coordinates. To visualize this operation, consider a vector \vec{r} pointing to a location in three-dimensional space (x, y, z) :

$$P(\vec{r}) = P : \begin{pmatrix} x \\ y \\ z \end{pmatrix} \longrightarrow \begin{pmatrix} -x \\ -y \\ -z \end{pmatrix} = -\vec{r}$$

From this example, it seems that vectors will change sign under the P operation. As a test of this hypothesis, the same operation can be done on the vector \vec{L} representing angular momentum:

$$\begin{aligned} \vec{L} &= \vec{r} \times m\vec{v} \\ P(\vec{L}) &= P(\vec{r} \times m\vec{v}) \\ &= P(\vec{r}) \times mP(\vec{v}) \\ &= -\vec{r} \times -m\vec{v} \\ &= \vec{L} \end{aligned}$$

Although this test disproved the hypothesis that all vectors change sign under the P operation, it demonstrates that there are two types of vectors: those that are inverted (polar vectors) and those that remain invariant under P (axial vectors). In addition to the two vector types, there are two scalar types: scalars and pseudoscalars. Pseudoscalars change sign under the P operation whereas scalars, such as the mass m in the angular momentum example above, are invariant under the P operation.

The neutron EDM search serves as a direct test for P violation. This can be shown via application of the P operator to the term in the Hamiltonian that represents the interaction between the EDM and the electric field:

$$H = -\vec{d} \cdot \vec{E} \xrightarrow{P} \vec{d} \cdot \vec{E} \quad (1.2)$$

where $\vec{d} = d_n \frac{\vec{S}}{S}$ is the EDM and \vec{E} is the electric field. See Table 1.1 for examples of how these physical observables transform under P. The sign change under P indicates that a non-zero neutron EDM d_n would result in P violation.

Time-Reversal

The aptly named time-reversal (T) operation is the transformation of a system corresponding to the inversion of the time coordinate, $t \rightarrow -t$. Although conceptually simple, it is not trivial to design an experiment which can be performed in both “time directions”, as the high level of control over various conditions, such as momenta and reaction rates, is not always feasible. To avoid these difficulties, most experiments testing for T violation are precise measurements of quantities which should be identically zero if T is a perfect symmetry. The neutron EDM is an example of such a quantity, demonstrated by the application of T to the term in the Hamiltonian containing the EDM:

$$H = -\vec{d} \cdot \vec{E} \xrightarrow{T} \vec{d} \cdot \vec{E}$$

Table 1.1 shows the transformations of these quantities under T. Just as with the P operation (Eq. 1.2), the EDM term is T-odd, implying that a non-zero value for the neutron EDM \vec{d} would yield T violation.

Moving from the classical picture to quantum mechanics reveals an important feature of time reversal. Consider applying a T operation on a state $|\psi\rangle$ such that:

$$|\psi\rangle \xrightarrow{T} |\psi_T\rangle \equiv T|\psi\rangle$$

Using the time evolution operator $\exp\left(\frac{-iHt}{\hbar}\right)$, one can evolve the state from $t = 0$ for an infinitesimal time interval δt , resulting in:

$$|\psi(\delta t)\rangle = (1 - iH\delta t) |\psi(0)\rangle$$

The time reversed state of $|\psi(\delta t)\rangle$ is $|\psi_T(\delta t)\rangle$. Assuming time reversal symmetry, evolving the time reversed state by the same infinitesimal time step δt will give a state equivalent to the initial state $|\psi(0)\rangle$.

$$\begin{aligned} (1 - iH\delta t) |\psi_T(\delta t)\rangle &= (1 - iH\delta t)T|\psi(\delta t)\rangle \\ &= (1 - iH\delta t)T(1 - iH\delta t) |\psi(0)\rangle \\ &= |\psi(0)\rangle \end{aligned} \tag{1.3}$$

From Eq. 1.3, it must be true that:

$$T(-i)H = iHT \tag{1.4}$$

If T is a unitary operator, T and H would have an anticommutation relation $TH = -HT$. Given an eigenstate $|\phi\rangle$ of a Hamiltonian H , the energy E_ϕ of the state is found by applying with the Hamiltonian operator:

$$H|\phi\rangle = E_\phi|\phi\rangle$$

The energy of the time reversed state $T|\phi\rangle$ would be:

$$HT|\phi\rangle = -TH|\phi\rangle = -E_\phi T|\phi\rangle$$

The time reversed state has negative energy and the energy spectrum is unbounded from below, which cannot be allowed [12]. Therefore, T must be an antiunitary operator, meaning $Ti = -iT$. In this case, T and H can commute meaning that eigenstates states' energy will remain constant under the T operation:

$$HT|\phi\rangle = TH|\phi\rangle = E_\phi T|\phi\rangle$$

Combined Symmetries

C, P, and T were thought to be conserved by the laws of physics until the discovery of parity violation in 1957 [6]. In order to make sense of this result, V-A theory was proposed by Sudarshan and Marshak [13] and was later published by Feynman and Gell-Mann [14]. V-A allowed for maximal P violation but conserved the combined CP operation. CP is a stronger symmetry of the SM than P, however CP symmetry was also found to be violated just seven years later [15]. Based on this result, one might question why the combination of all three discrete symmetries would not also be violated. Any local quantum field theory with Lorentz invariance and a Hermitian Hamiltonian must be invariant under CPT [16, 17, 18]. Thus, the discovery of CPT violation would imply that at least one of these conditions—locality, Lorentz invariance, or a Hermitian Hamiltonian—need not be included within the theoretical framework.

Although CPT violation may be discovered in the future, the remainder of the work presented here will assume CPT invariance of physical laws. As shown in the previous section, a non-zero neutron EDM violates T and P symmetry, and the invariance of CPT implies that the operation CP must have a corresponding violation. In summary, the neutron EDM is a test of P, T, and CP (via invariance of CPT).

1.2 Theoretical Motivation for the Neutron EDM Search

One might assume that the Big Bang would have resulted in equal amounts of matter and antimatter. Under this assumption, an observer on Earth might be perplexed by observing an abundance of matter relative to antimatter. Where is all of the antimatter? Physicists have hypothesized that perhaps Earth resides in a matter-dominated region of the universe, and the “missing” antimatter exists in an antimatter-dominated region. If this were the case, there would be a border at which the matter and antimatter regions meet, and one would expect to see a radiation signature from the annihilation interactions that must be occurring. However, astrophysical observations do not support the existence of antimatter-dominated regions of space—on the contrary, they indicate that the known universe is all matter [19, 20]. Assuming the universe began in an initially symmetric state (e.g. equal amounts of matter and antimatter), there must have been a mechanism active in the early universe that caused a matter-antimatter asymmetry to form. In order to find a solution to the baryon asymmetry problem, physicists must know where to look. So the question becomes, what properties must this mechanism possess?

In 1967, Sakharov [21] indicated three guidelines which, when simultaneously satisfied, allow for a baryon asymmetry to evolve:

1. Baryon number (B) violating process

If every process conserves baryon number individually, then baryon number will be conserved globally. Therefore, if the initial state is symmetric ($B = 0$) and an asymmetry is produced ($B > 0$), there must exist at least one

process

$$X \rightarrow Y + B \tag{1.5}$$

where X and Y have a baryon number of zero and B represents excess baryons ($B > 0$).

2. Violation of C and CP symmetries

If C were not violated, every process resulting in a positive ΔB (Eq. 1.5) would occur at the same rate as a counterpart process which produces a negative ΔB with equal magnitude. The effect of two such processes would be a net zero change in B, and thus no baryon asymmetry could be generated.

If C is violated but the combined CP symmetry is not, the change of B will be washed out by counteracting processes generating equal amounts of baryons and the corresponding charge-conjugated particles. For example, consider an initial state i with helicity λ which decays into a final state f and the variants under C and P operations:

$$\begin{aligned} \Gamma[i(\lambda) \rightarrow f] &= \Gamma_1 \\ \Gamma[i(-\lambda) \rightarrow f] &= \Gamma_2 \\ \Gamma[\bar{i}(\lambda) \rightarrow \bar{f}] &= \Gamma_3 \\ \Gamma[\bar{i}(-\lambda) \rightarrow \bar{f}] &= \Gamma_4 \end{aligned} \tag{1.6}$$

where Γ represents a rate. If C is violated, the charge-conjugated interactions will occur at different rates: $\Gamma_1 \neq \Gamma_3$ or $\Gamma_2 \neq \Gamma_4$. But if CP holds, which implies $\Gamma_1 = \Gamma_4$ and $\Gamma_2 = \Gamma_3$, then the total rate of interactions resulting in the final state f is equal to the rate at which \bar{f} is produced. Any ΔB resulting from the production of state f is exactly canceled by a ΔB resulting from production of state \bar{f} , resulting in a zero net change of B. Allowing for CP violation, meaning $\Gamma_1 \neq \Gamma_4$ and/or $\Gamma_2 \neq \Gamma_3$, the final states f and \bar{f} are produced at different rates, providing the opportunity to produce excess baryons. Therefore, C and CP violation must occur simultaneously in order to develop a baryon asymmetry.

3. Departure from thermodynamic equilibrium

In thermal equilibrium, a reaction $i \rightarrow f$ is equally likely to occur as $f \rightarrow i$. Additionally, the rate at which a reaction occurs in thermal equilibrium depends on the mass and temperature of the system [22]. Invoking CPT invariance, the masses of baryons and antibaryons are identical, implying that the reactions producing each is the same and resulting in no asymmetry generation. Thus, the B violating processes must occur outside of thermal equilibrium in order for a net change in B to evolve.

The conditions presented by Sakharov are not strict requirements as models exist that generate a BAU without satisfying all three conditions [12, 23]. The remainder of this section will focus on the second condition, specifically the CP violation necessary to generate the Baryon Asymmetry of the Universe (BAU).

CP Violation in the Standard Model

The Standard Model (SM) contains two potential sources of CP violation: the electroweak sector and the strong sector. Violation of CP symmetry in the weak interaction was discovered via the observation of 2π decay of the K_2^0 meson by Cronin and Fitch in 1964 [15]. The observed CP violation is parameterized in the Cabibbo-Kobayashi-Maskawa (CKM) matrix (Eq. 1.7). The CKM matrix represents the mixing of u -type quarks and d -type quarks in charged weak interactions.

$$V_{CKM} = \begin{pmatrix} V_{ud} & V_{us} & V_{ub} \\ V_{cd} & V_{cs} & V_{cb} \\ V_{td} & V_{ts} & V_{tb} \end{pmatrix} \quad (1.7)$$

A standard parameterization [24] of the CKM matrix is shown in Eq. 1.8, containing three real mixing angles θ_{12} , θ_{23} , and θ_{13} and a complex phase δ :

$$V_{CKM} = \begin{pmatrix} c_{12}c_{13} & s_{12}c_{13} & s_{13}e^{-i\delta} \\ -s_{12}c_{23} - c_{12}s_{23}s_{13}e^{i\delta} & c_{12}c_{23} - s_{12}s_{23}s_{13}e^{i\delta} & s_{23}c_{13} \\ s_{12}s_{23} - c_{12}c_{23}s_{13}e^{i\delta} & -c_{12}s_{23} - s_{12}c_{23}s_{13}e^{i\delta} & c_{23}c_{13} \end{pmatrix} \quad (1.8)$$

where $c_{ij} = \cos(\theta_{ij})$ and $s_{ij} = \sin(\theta_{ij})$. The complex phase δ is the source of CP violation in the weak interaction. Through calculations of Feynman diagrams that are CP violating (i.e. the phase δ does not cancel) for a neutron coupling to an external photon, physicists obtain SM estimates for the neutron EDM: $d_n \sim 10^{-32} e\cdot\text{cm}$ [1]; 6 orders of magnitude smaller than the current experimental upper limit. The small magnitude of the estimate can be attributed to the impossibility of neutron EDM contribution from a diagram with less than 2 loops and the coincidental cancellation at the 2-loop level, leaving 3-loop diagrams for leading order neutron EDM contributions [25].

In the strong sector, CP violation has not been observed. However, it remains a theoretical possibility through the so-called θ term in the strong interaction:

$$\mathcal{L}_{\bar{\theta}} = -\frac{\alpha_s}{16\pi^2} \bar{\theta} \text{Tr} \left(G^{\mu\nu} \tilde{G}_{\mu\nu} \right) \quad (1.9)$$

where α_s is the strong coupling constant, $G_{\mu\nu}$ is the gluon field and $\tilde{G}_{\mu\nu} = \epsilon_{\mu\nu\alpha\beta} G^{\alpha\beta} / 2$ is its dual. $\bar{\theta}$ can be written as:

$$\bar{\theta} = \theta + \arg \det [\mathbf{G}^{(U)} \mathbf{G}^{(D)}]$$

where θ is an arbitrary coefficient of the CP violating term in the strong interaction and $\mathbf{G}^{(U,D)}$ correspond to complex flavor matrices. Since CP violation exists in the weak interaction, these \mathbf{G} matrices will have a non-zero contribution to $\bar{\theta}$ when they are rotated to give real masses [12].

$\bar{\theta}$ will contribute to the the neutron EDM with the relation $d_n^{\bar{\theta}} \approx 1 \times 10^{-16} \bar{\theta} e\cdot\text{cm}$ [26]. The current neutron EDM upper limit at $|d_n| < 1.8 \times 10^{-26} e\cdot\text{cm}$ implies $|\bar{\theta}| \lesssim 10^{-10}$. The small value for $\bar{\theta}$, instead of the expected order of unity, requires

a fine tuning of the pure QCD angle θ and the phases of the quark mass matrices, posing the “strong CP problem” [27]. This remains an outstanding problem in physics with many proposed solutions, the most well-known being the Peccei-Quinn theory involving the introduction of a scalar particle called an axion [28].

Theoretical estimates of the BAU can be derived from the known CP violation in the SM. The magnitude of the asymmetry is often defined by an asymmetry parameter η :

$$\eta = \frac{n_B - n_{\bar{B}}}{n_\gamma}$$

where $n_B(n_{\bar{B}})$ is the number density of baryons (antibaryons) and n_γ is the number density of photons. The standard model fails to predict the measured asymmetry value, $\eta \approx 6 \times 10^{-10}$, obtained through measurements of the cosmic microwave background [29]. The combination of observed light element abundances and primordial abundances predicted from the standard model of Big-Bang nucleosynthesis can also be used to extract η . These predictions agree with the value from the CMB measurements within a factor of ~ 2 —the D/H estimate is the most precise and provides an asymmetry value $\eta = (6.143 \pm 0.19) \times 10^{-10}$ [30]. The inability for known CP violation to accommodate the relatively large BAU magnitude motivates physicists to search for other mechanisms of CP violation, including the proposal of models which extend the SM to provide solutions for its known shortcomings (e.g. the minimal supersymmetric model).

The neutron EDM offers a promising avenue of research as a potential source of CP violation which could help explain the development of the BAU. A neutron EDM measurement above the SM prediction from the weak interaction would be a certain discovery of new CP violation, either from currently unknown SM sources (i.e. the θ -term in the strong sector) or possibly from a beyond SM mechanism. Although the nearly seven decades of neutron EDM searches have not yielded a non-zero result, given the six orders of magnitude which separate the SM prediction and the best experimental upper-limit, there is still a large parameter space in which a significant result could be discovered. This statement is not meant to imply that the neutron EDM measurements to date lack significance—on the contrary, these measurements provide constraints on beyond SM theory parameters, which provide the CP violation to solve the baryon asymmetry problem. A neutron EDM estimate can be extracted from these parameters; thus the experimental constraints on the neutron EDM magnitude restricts the parameter space available, effectively eliminating theories which require abundant fine-tuning from consideration. Figure 1.1 shows the experimental sensitivity of neutron EDM experiments over time compared to predictions of neutron EDM magnitude from several popular beyond SM theories.

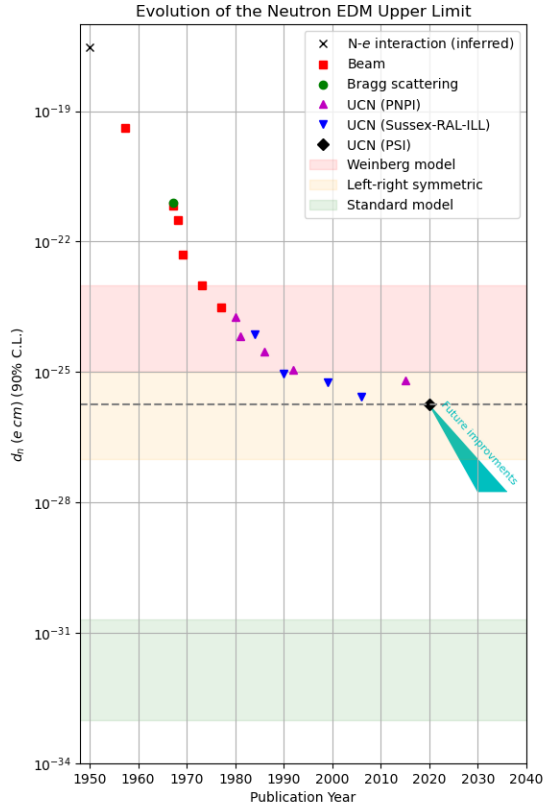


Figure 1.1: The upper limits of the neutron EDM for various experiments. This plot is adapted from T. Ito (personal communication). Also shown are theoretical predictions of the neutron EDM magnitude from the Standard model and two BSM theories [31].

Chapter 2 The LANL-nEDM Experiment

The first neutron EDM experiments were performed using a magnetic resonance technique on a neutron beam. Using this method, the neutron EDM upper limit was pushed down to $|d_n| < 3 \times 10^{-24} e \cdot \text{cm}$ by 1977 [32]. The ever-increasing demand for improved sensitivity, combined with the large systematic effects associated with the neutron beam method, compelled the development of new experimental designs. The latest neutron EDM experiment, completed at the Paul Scherrer Institute (PSI), used Ramsey’s method of separated oscillatory fields applied to ultracold neutrons (UCN) to obtain the current upper limit of $|d_n| < 1.8 \times 10^{-26} e \cdot \text{cm}$, which is largely dominated by the statistical error bar. A ^{199}Hg co-magnetometer and an array of external magnetometers were used to control systematic effects. Building on the success of the experiment conducted at PSI, the LANL-nEDM experiment will implement these methods with a higher-yield UCN source, providing the statistical reach and systematic control to attain the goal sensitivity of $\sim 3 \times 10^{-27} e \cdot \text{cm}$.

2.1 Measuring the Neutron Electric Dipole Moment

In the presence of electric and magnetic fields, the interaction terms of the neutron coupling with the fields are contained in the Hamiltonian below (Eq. 2.1). The energy of a neutron under the application of these fields depends on the alignment of the EDM and magnetic moment with the electric and magnetic fields, respectively, visually represented in Figure 2.1.

$$H = -\vec{\mu}_n \cdot \vec{B} - \vec{d}_n \cdot \vec{E} \quad (2.1)$$

The magnetic moment of the neutron is essential for the application of Ramsey’s Method of separated oscillatory fields. Since the neutron has a nonzero magnetic

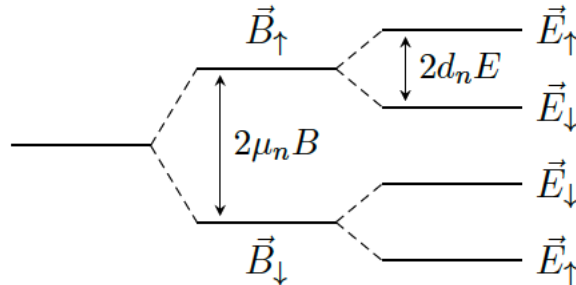


Figure 2.1: Visualization of the energy splitting due to the neutron magnetic moment and EDM coupling to parallel (\uparrow) and anti-parallel (\downarrow) magnetic and electric fields. [33]

moment, the spin of a neutron will precess about an external magnetic field—a phenomenon known as Larmor precession—with a frequency

$$\omega_L = \gamma B$$

where γ is the gyromagnetic ratio and B is the magnitude of the magnetic field. The gyromagnetic ratio is the ratio of the magnetic moment to the spin angular momentum, $\gamma = \mu/S$. For a neutron,

$$S = \hbar/2 \longrightarrow \omega_L = \frac{2\mu_n B}{\hbar} \quad (2.2)$$

Note that the energy $\hbar\omega_L$ associated with this precession corresponds to the energy splitting shown in Fig. 2.1. The magnetic moment of the neutron is [34],[35]:

$$\mu_n = -9.662 \times 10^{-27} \text{ J T}^{-1}$$

The negative sign refers to the direction of the observed precession. In a 1 μT magnetic field, which is the nominal magnetic field magnitude for the LANL-nEDM experiment, a neutron will precess at:

$$\omega_L = 183.25 \text{ rad s}^{-1}$$

An EDM would couple to an electric field in the same manner. In this case, the precession frequency ω_E would depend on the magnitude of the electric field E and EDM d_n , as shown below.

$$\omega_E = \frac{2d_n E}{\hbar}$$

Following the parallel with the magnetic moment, the EDM magnitude can be extracted by measuring the precession frequency of the neutron spin in a known electric field. Given the expected electric field magnitude for the experiment $E \approx 10 \text{ kV cm}^{-1}$ and the statistical reach of $d_n \sim 3 \times 10^{-27} e\cdot\text{cm}$, the resulting precession frequency about the electric field is:

$$\omega_E \approx 9.1 \times 10^{-8} \frac{\text{rad}}{\text{s}}$$

At this rate, it would take over two years to observe one full rotation—a precession frequency equivalent to Larmor precession about a $\sim 10^{-16} \text{ T}$ magnetic field. The neutron spin is also unlikely to remain in the precession plane due to the weak energy coupling with the electric field compared to other interactions. The level of precision and environmental control needed to measure the EDM using only an electric field is not feasible.

Thus, the measurement is conducted via application of magnetic and electric fields simultaneously. Assuming the fields are parallel ($\uparrow\uparrow$), the total neutron spin precession frequency resulting from the torques exerted is:

$$\omega_{\uparrow\uparrow} = \frac{2}{\hbar} (\mu_n B + d_n E) \quad (2.3)$$

The same formulation can be written with anti-parallel ($\uparrow\downarrow$) fields:

$$\omega_{\uparrow\downarrow} = \frac{2}{\hbar} (\mu_n B - d_n E) \quad (2.4)$$

Then it is straight forward to extract the neutron EDM, d_n , by taking the difference of the precession frequencies in the parallel and anti-parallel cases.

$$d_n = \frac{\hbar \Delta\omega}{4 E} \quad (2.5)$$

where $\Delta\omega = \omega_{\uparrow\uparrow} - \omega_{\uparrow\downarrow}$. Using Eq. 2.3 and Eq. 2.4, one can determine that $\Delta\omega$ is proportional to ω_E . Then it is reasonable to ask: “What have we gained by adding the magnetic field?” The answer to this question is two-fold: First, the magnetic field provides control over the direction of the neutron spin, making it possible to maintain spin alignment in a population of neutrons throughout a measurement cycle. Second, magnetic resonance techniques can be used in order to amplify the neutron EDM signal, as described in the following subsection.

Consider the circumstance described by Eq. 2.3 where the applied magnetic and electric fields are parallel. The total precession frequency is almost entirely a result of the magnetic field term, with the electric field term representing a small shift away from the Larmor frequency. It is not obvious how to extract this small frequency shift. The technique used most commonly in current neutron EDM experiments is the application of an oscillating magnetic field transverse to the initial neutron polarization in a two-pulse sequence, known as the Ramsey’s method of separated oscillatory fields. In this method, the probability of transitioning from $|\downarrow\rangle$ to $|\uparrow\rangle$ depends on the frequency of the applied oscillating magnetic field as well as the time separation of the magnetic field pulses. Therefore, the frequency shift due to the electric field can be extracted from a ratio of the two neutron spin states—aligned or anti-aligned with the static magnetic field.

Rabi Resonance Method

Before moving into the details of Ramsey’s method, it is important to understand the Rabi resonance method, from which Ramsey derived his technique. The method will be described in the context of neutron EDM experiments. Consider a neutron in a constant magnetic field \vec{B}_0 along \hat{z} . The energy difference between the spin anti-aligned state $|\downarrow\rangle$ and the spin aligned state $|\uparrow\rangle$ is $\hbar\omega_0$ where $\omega_0 = \gamma_n B_0$. The application of a magnetic field \vec{B}_1 which is perpendicular to the quantization direction \hat{z} and rotating at an angular frequency ω will cause Rabi oscillations between the spin aligned and spin anti-aligned states. The frequency of these Rabi oscillations is derived below, following an excellent derivation in Ryan Dadisman’s dissertation [36].

Recall the Hamiltonian for a neutron in an external magnetic field from 2.1:

$$H = -\vec{\mu}_n \cdot \vec{B} \quad (2.6)$$

where $\vec{\mu}_n = \hbar\gamma_n\vec{S}$ and $|\vec{S}| = \frac{1}{2}$ for the neutron. As described above, the magnetic field in this case is

$$\begin{aligned}\vec{B} &= \vec{B}_0 + \vec{B}_1 \\ &= B_0\hat{z} + B_1(\cos(\omega t)\hat{x} + \sin(\omega t)\hat{y})\end{aligned}\quad (2.7)$$

The time dependence in the neutron state can be separated into the contribution from the B_0 field and the B_1 field, considering the B_1 field as a time-dependent perturbation. Thus, the Hamiltonian can be written as:

$$H = H_0 + H_1 \quad (2.8)$$

$$H_0 = -\frac{\hbar\gamma_n B_0}{2}\sigma_z; \quad H_1 = -\frac{\hbar\gamma_n B_1}{2}(\cos(\omega t)\sigma_x + \sin(\omega t)\sigma_y) \quad (2.9)$$

$$\begin{aligned}H &= -\frac{\hbar\gamma_n}{2}\begin{pmatrix} B_0 & B_1\cos(\omega t) - i\sin(\omega t) \\ B_1\cos(\omega t) + i\sin(\omega t) & -B_0 \end{pmatrix} \\ &= -\frac{\hbar\gamma_n}{2}\begin{pmatrix} B_0 & B_1e^{-i\omega t} \\ B_1e^{i\omega t} & -B_0 \end{pmatrix}\end{aligned}\quad (2.10)$$

The time evolution of a general state $|\Psi\rangle$ in the S_z basis using the Schrödinger equation:

$$i\hbar\frac{\partial}{\partial t}|\Psi\rangle = H|\Psi\rangle = -\frac{\hbar\gamma_n}{2}\begin{pmatrix} B_0 & B_1e^{-i\omega t} \\ B_1e^{i\omega t} & -B_0 \end{pmatrix}|\Psi\rangle \quad (2.11)$$

where

$$|\Psi\rangle = \begin{pmatrix} \psi_+(t) \\ \psi_-(t) \end{pmatrix}$$

Here, $|\psi_+\rangle$ and $|\psi_-\rangle$ represent the spin-up and spin-down states, respectively.

$$|\psi_+\rangle = \begin{pmatrix} 1 \\ 0 \end{pmatrix} \quad \text{and} \quad |\psi_-\rangle = \begin{pmatrix} 0 \\ 1 \end{pmatrix}$$

The energies associated with H_0 , the time independent part of the interaction, are:

$$E_{\pm} = \mp\frac{\hbar\gamma_n}{2}B_0 \quad (2.12)$$

Using these energies, the time dependence of the general state can be written as

$$\Psi(t) = u(t)e^{-iE_+t/\hbar}\psi_+ + d(t)e^{-iE_-t/\hbar}\psi_- \quad (2.13)$$

Plugging $\Psi(t)$ into Eq. 2.11, the following coupled differential equations are found:

$$\dot{u} = \frac{i\gamma_n B_1}{2}e^{i(\omega-\omega_0)t}d \quad (2.14)$$

$$\dot{d} = \frac{i\gamma_n B_1}{2}e^{-i(\omega-\omega_0)t}u \quad (2.15)$$

$$\implies \ddot{u} - i(\omega - \omega_0)\dot{u} + \frac{\gamma_n^2 B_1^2}{4}u = 0 \quad (2.16)$$

The general solution for this second-order homogeneous differential equation is:

$$u(t) = e^{i(\omega - \omega_0)t/2} (C_1 e^{i\Omega t} + C_2 e^{-i\Omega t}) \quad (2.17)$$

where

$$\Omega = \frac{\sqrt{(\omega - \omega_0)^2 + \gamma_n^2 B_1^2}}{2}$$

The coefficients C_1 and C_2 can be solved using the initial conditions of the system. At time $t = 0$, the neutron is assumed to be in the spin anti-aligned state—spin-down in this case since the field is in the \hat{z} direction and $\gamma_n < 0$. Therefore, $u(t = 0) = 0$ and $d(t = 0) = 1$.

$$u(0) = 0 \implies C_1 = -C_2$$

$$u(t) = 2C_1 e^{i(\omega - \omega_0)t/2} \sin(\Omega t) \quad (2.18)$$

Using Eq. 2.14, $d(t)$ can be expressed as:

$$d(t) = \frac{4C_1}{i\gamma_n B_1} e^{-i(\omega - \omega_0)t/2} \left[i \frac{\omega - \omega_0}{2} \sin(\Omega t) - \Omega \cos(\Omega t) \right] \quad (2.19)$$

$$d(0) = 1 \implies C_1 = \frac{i\gamma_n B_1}{4\Omega}$$

The probability of measuring the neutron in the spin aligned state—i.e. spin-up—at any given time t is the probability of transitioning from the ground state to the excited state:

$$P_{-\rightarrow+} = |\langle \psi_- | \Psi \rangle|^2 = |u(t)|^2 \quad (2.20)$$

$$\begin{aligned} |u(t)|^2 &= 4|C_1|^2 \sin^2(\Omega t) \\ &= \frac{\gamma_n^2 B_1^2}{(\omega - \omega_0)^2 + \gamma_n^2 B_1^2} \sin^2 \left(\frac{\sqrt{(\omega - \omega_0)^2 + \gamma_n^2 B_1^2}}{2} t \right) \end{aligned} \quad (2.21)$$

Now, the frequency of transitions between the spin aligned and anti-aligned states can be easily read from Eq. 2.21, $\Omega = \sqrt{(\omega - \omega_0)^2 + \gamma_n^2 B_1^2}/2$. Note that the amplitude of the probability has a dependence on ω , the frequency at which the \vec{B}_1 field is oscillating. The maximum of this amplitude occurs at the resonant frequency $\omega = \omega_0$. Additionally, the probability can be maximized if the interaction time, during which the B_1 field is applied, is $t_{int} = \frac{\pi}{2\Omega}$. At resonance, this value simplifies to $t_{int} = \frac{\pi}{\gamma_n B_1}$. The application of the B_1 field for this period of time is known as a “ π pulse” because, in the classical picture, the neutron spin vector has been rotated by 180 degrees.

How can this be used to measure the neutron EDM? Consider a population of neutrons in the spin anti-aligned state from the derivation above. After the application of the π pulse, the ratio of neutrons in the spin anti-aligned state to the neutrons

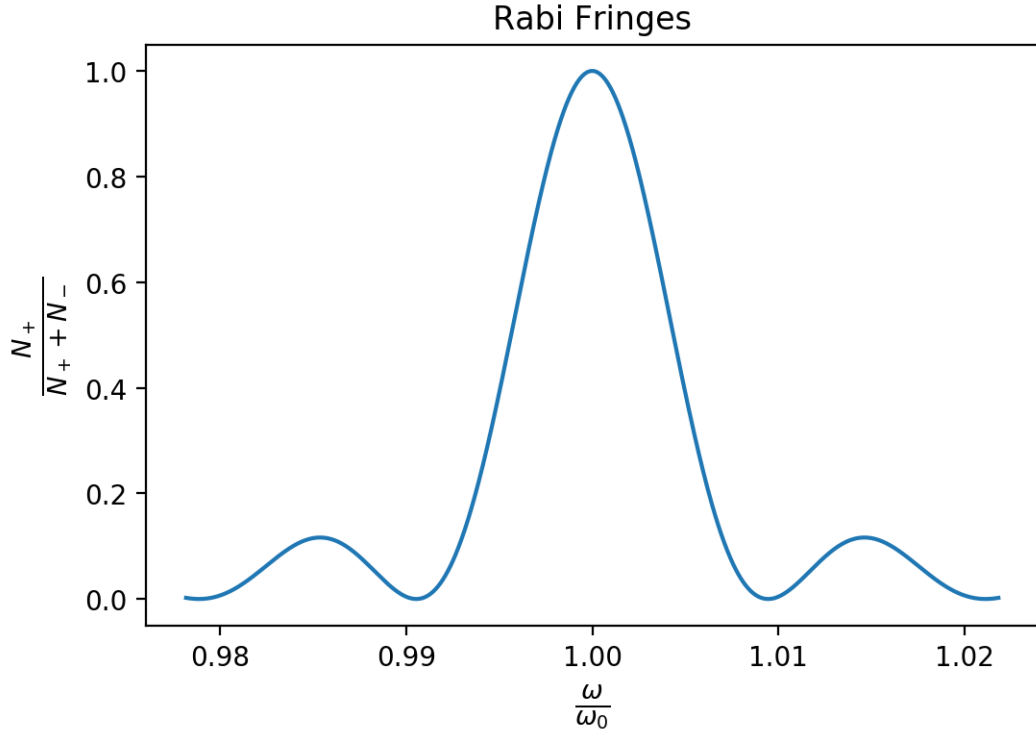


Figure 2.2: An example Rabi fringe pattern for the case where $\gamma_n B_1 = 1 \text{ s}^{-1}$ (see Eq. 2.21). The x-axis shows the frequency of the oscillating \vec{B}_1 field normalized to the Larmor frequency associated with the \vec{B}_0 excitation field, $\omega_0 = \gamma_n B_0$. The y-axis represents the number of neutrons in the spin-up state N_+ compared to the total number of neutrons $N = N_+ + N_-$ after the application of a π pulse. A resonance is observed at $\omega = \omega_0$.

in the spin aligned state will follow the probability given in Eq. 2.21. However, if the neutron EDM is non-zero, the resonant frequency will shift by ω_E . Fig. 2.2 shows an example Rabi fringe pattern for a range of frequencies normalized to the resonant frequency ω_0 . In this case, if an electric field is applied such that $\omega_E/\omega_0 \approx .004$, the experimenters would measure about 56% of the neutrons in the spin aligned state, as opposed to 100% without any EDM effect, and recognize that the resonant frequency is shifted from the expected value. As discussed earlier, ω_E represents a much smaller shift given the parameters of the LANL-nEDM experiment; $\omega_E/\omega_0 \approx 2 \times 10^{-10}$ at the expected sensitivity. Referring again to Fig. 2.2, a shift this small would result in negligible change in the number of neutrons measured in the spin aligned state. Thus, the Rabi method on its own is insensitive to the neutron EDM.

Ramsey's Method of Separated Oscillatory Fields

Ramsey was able to increase the precision of transition energy measurements, or equivalently resonant frequencies, by applying the Rabi spin-flip pulse as two $\pi/2$

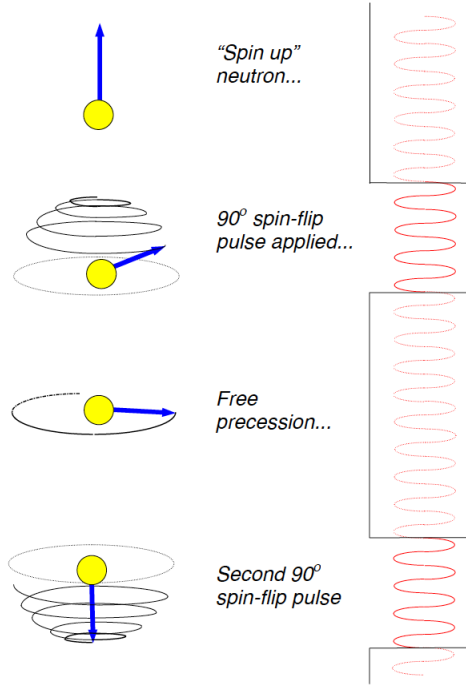


Figure 2.3: Diagram of Ramsey’s method of separated oscillatory fields. A static field B_0 is applied in the vertical direction, but is not shown in the image. The sinusoidal wave shown on the right represents a reference clock, which is used to apply an oscillating voltage to the coil producing the B_1 field during the two spin-flip pulses. Note that the clock is continuous and coherent throughout the sequence which allows a phase difference between the clock and neutron spin to accumulate during the free precession time. [37]

pulses separated by a free precession time rather than one continuous π pulse. The sequence is represented in the classical picture in Fig. 2.3. Initially, all of the neutron spins are anti-aligned with the static \vec{B}_0 field. The B_1 field is applied in the transverse plane at frequency ω for a time τ , which corresponds to a 90 degree rotation of the spin alignment into the transverse plane. The \vec{B}_1 field is then turned off, and the neutrons continue freely precess about the \vec{B}_0 field for a time T . If the applied frequency ω does not match the resonant frequency of the neutron precession ω_0 , a phase will accumulate between the neutron spin and the B_1 pulse. After the free precession period, a pulse of the \vec{B}_1 field is applied for a time τ representing the second $\pi/2$ pulse in the sequence. It is key for the first and second $\pi/2$ pulse to have the same phase so that the phase shift of the neutron spins relative to the second pulse can be attributed to the free precession period.

Similarly to the Rabi derivation above, one can derive the probability of measuring a neutron in the excited state after the application of Ramsey’s method of separated oscillatory fields. Assuming a neutron initially in the ground state, the probability of

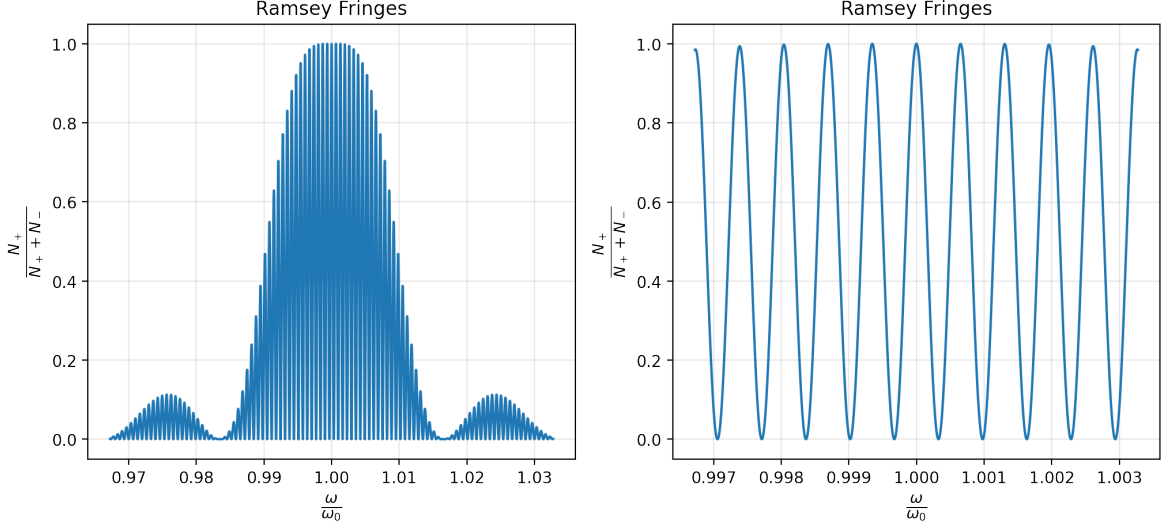


Figure 2.4: Plots showing the probability of a neutron transitioning the excited state after the application of Ramsey’s method of separated oscillatory fields. The following assumptions are used: the neutron is initially in the ground state, 50 second free precession period, $|\vec{B}_1|$ is chosen for 2 second $\pi/2$ pulse duration, and $|\vec{B}_0| = 1 \mu\text{T}$. The left plot contains Ramsey fringes over a wide range of normalized frequencies. The right plot show the fringes over a much smaller range so that the structure of the fringes near $\omega = \omega_0$ can be seen clearly.

measuring the neutron in the excited state is [36]:

$$P = 4 \left(\frac{\gamma_n B_1}{2\Omega} \right)^2 \sin^2(\Omega\tau) \left[\cos(\Omega\tau) \cos\left(\frac{\omega_0 - \omega}{2}T\right) - \frac{\omega_0 - \omega}{2\Omega} \sin(\Omega\tau) \sin\left(\frac{\omega_0 - \omega}{2}T\right) \right]^2 \quad (2.22)$$

Using a plot of this probability as a reference (see Fig. 2.4), some physical intuition can be gained from Eq. 2.22 as it relates to the neutron EDM measurement. Many fine fringes exist within a larger envelope, contained in the first term of Eq. 2.22:

$$P_{envelope} = 4 \left(\frac{\gamma_n B_1}{2\Omega} \right)^2 \sin^2(\Omega\tau)$$

Note that this term has the same form as Eq. 2.21, revealing information about the source of this outer envelope—namely, Rabi fringes. Even though the $\pi/2$ pulses are separated in time, they will not be very effective at flipping spins if the applied frequency is far from resonance, resulting in fewer neutrons in the excited state.

The fine fringes within the Rabi envelope come from the bracketed term in Eq. 2.22. The source of these fringes is the phase shift between the neutron spins and B_1 voltage clock during the free precession period. The classical picture can be

used here, visualizing the neutron spin as a vector, to gain intuition for this effect. After the first $\pi/2$ pulse, assuming we are near resonance, the B_1 voltage clock and neutron spin precession are approximately coherent. If $\omega = \omega_0$, then the two systems will remain in phase, and the second spin flip will result in maximal probability of exciting the neutron as if no free precession period occurred. However, if $\omega \neq \omega_0$, the free precession time will generate a phase difference ϕ between the two systems:

$$\phi = (\omega - \omega_0) T_{FP} \quad (2.23)$$

Now two scenarios can be evaluated: ϕ is an even multiple of π and ϕ is an odd multiple of π . For the case where ϕ is an even multiple of π , the angle between B_1 and neutron spin is identical at the end of the first $\pi/2$ pulse and the beginning of the second $\pi/2$ pulse. Therefore, the torque applied on the spin by the second pulse is the same as if there were no free precession period separating the two pulses, resulting in a Rabi fringe pattern. Plugging in the numbers used for the example fringes in Fig 2.4 and calculating ϕ from Eq. 2.23, one can see that the peaks of the fine fringes occur at these even multiples of π .

On the other hand, if ϕ is an odd multiple of π , the torque applied by the B_1 field will be in the opposite direction for the second pulse compared to the first. Effectively, \vec{B}_1 has been replaced by $-\vec{B}_1$, causing the rotation of the spin during the first pulse to be completely undone by the second pulse. In Fig 2.4, this can be seen at the troughs of the fine fringes where all neutrons are measured in the initial state which was assumed to be the ground state.

The width of the central fringe in the Ramsey fringe pattern is the distance between the first two troughs at frequencies corresponding to $\phi = \pm\pi$. Using Eq. 2.23, this distance is found to be proportional to the free precession period T_{FP} . Therefore, to measure a small frequency shift, T_{FP} should be maximized and ω should be chosen slightly off resonance ($\phi \approx \pi/2$) near the steepest region of the fringes such that small changes in frequency result in the largest possible changes of excited state neutron count.

2.2 LANL-nEDM Apparatus and Experimental Cycle

The apparatus for the LANL-nEDM experiment is designed to optimize the implementation of Ramsey’s method within the current technological landscape to extract the neutron EDM value. The important factors for accomplishing the goal sensitivity include a high density of neutrons within the storage volume, a long free precession period, polarization of the neutron population throughout the experimental cycle, and fine control and precise knowledge of magnetic and electric fields. The various techniques used to address these challenges are introduced in this section.

Ultracold Neutrons

The experimental cycle begins with the generation of neutrons via a pulsed proton beam from an 800 MeV linear accelerator impinging on a tungsten spallation target. The average energy of these spallation neutrons is 2 MeV. In order to reduce the

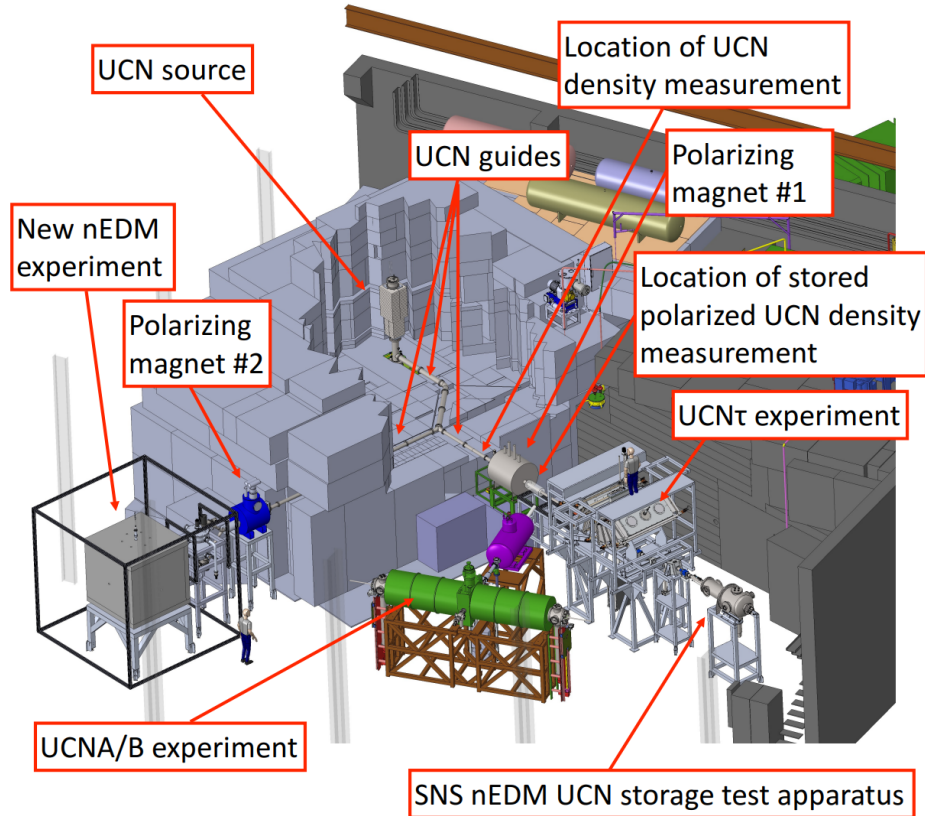


Figure 2.5: CAD model of the UCN experimental hall at LANL from [38]. The LANL-nEDM experimental setup is shown on the left side of the image. The neighboring experiments measure the free neutron lifetime ($UCN\tau$) and the neutron β -decay parameter A_0 (UCNA) [39],[40].

energy, the neutrons are moderated by beryllium and graphite, resulting in thermal neutrons. The neutrons are further moderated by cold polyethylene beads, taking the neutron energies down to the cold regime. The last step of energy reduction within the neutron source involves a solid deuterium (SD_2) volume where the neutron energy is reduced to < 300 neV by exciting phonons in the SD_2 crystal structure [41]. Neutrons at this extremely low energy are referred to as Ultracold neutrons (UCNs). See Table 2.1 for a summary of UCN properties.

UCNs hold a key property for the success of modern neutron EDM searches—they can be stored in material bottles, allowing for long free precession periods in the Ramsey cycle. As a UCN approaches a surface, the long wavelength causes it to interact with many nuclei simultaneously. For some materials, the effective optical potential produced by these nuclei can reflect the neutron for all angles of incidence. This effective potential V_F is called the Fermi Potential, named after Enrico Fermi who originally formulated the interaction. The surfaces that the neutrons will encounter throughout the experimental cycle must be coated with a material

Table 2.1: A summary of energetic properties of UCNs relevant to the LANL-nEDM experiment.

Parameter	Value
Kinetic Energy	$< 300 \text{ neV}$
Temperature	$< 4 \text{ mK}$
Wavelength	$> 500 \text{ \AA}$
Velocity	$< 8 \text{ m/s}$
Gravitational Potential Energy	100 neV/m
Magnetic Potential Energy	60 neV/T

obtaining a high Fermi potential to minimize neutron losses and, thus, maximize statistical sensitivity. The chosen material coatings to achieve this goal are deuterated polystyrene ($V_F = 160 \text{ neV}$) on the storage cells’ walls and NiP ($V_F = 213 \text{ neV}$) on the neutron guides, which serve to transport neutrons between the source and the storage cells. It is important to note that the selection of these materials is not just contingent on high Fermi potentials. The coatings must also be nonmagnetic, have low depolarization rate, and, in the case of the storage cell coating, be electrically insulating. The importance of these additional requirements will be made clear in the remaining subsections.

Each UCN from the source has random spin orientation resulting in an unpolarized population of neutrons. In order to implement Ramsey’s method of separated oscillatory fields, as discussed in the previous section, the neutrons must initially be polarized in the direction of the \vec{B}_0 magnetic field, nominally the z direction for the LANL-nEDM experiment. Polarization in the z direction is obtained in two steps: 1) Polarize the neutron population using a strong magnetic field; 2) Rotate the polarization to the z direction. The neutrons are nearly all spin-aligned along x immediately after passing through the polarizing magnetic field, which described in the next subsection, resulting in a polarization of > 0.99 .

Polarizing Magnet

Polarization of the neutron population is accomplished via the application of a 5 T magnetic field within the neutron guide provided by the aptly named “polarizing magnet” shown in Fig 2.6.

The UCNs, propagating from the source through the neutron guide system, couple to the magnetic field due to the magnetic moment ($-\vec{\mu} \cdot \vec{B}$) giving a potential energy of $\pm 300 \text{ neV}$, corresponding to the spin aligned state or anti-aligned state, respectively. Note that the spin vector and magnetic moment vector are anti-parallel, so the magnetic field is aligned with the field when the neutron spin is anti-aligned. A thin aluminum foil is placed in the high field region of the polarizing magnet to supply a repulsive optical potential for the UCN. For standard neutron energy ranges, a 300 neV coupling would likely be negligible, but, given the UCN kinetic energy is $< 300 \text{ neV}$, the UCN that experience a high magnetic potential—i.e. the state with



Figure 2.6: Picture of the 5 T superconducting solenoidal polarizing magnet to be used in the LANL-nEDM experiment. [41]

spin aligned along the magnetic field direction since the neutron magnetic moment is negative—will experience a potential barrier greater than or equal to kinetic energy in the high field region. Combining the magnetic and optical potentials from the polarizing field and thin foil, UCN in the spin-aligned state have a near zero probability of passing through the potential barrier. Meanwhile, the UCN with spin anti-aligned to the field direction will experience a potential well at the high field region, effectively accelerating the neutrons through the optical potential of the thin foil to the other side of the magnet. The resulting UCN flux exiting the polarizing magnet will be $> 99\%$ polarized.

UCN Transport

The experiment relies on a low magnetic field environment at the storage cell volume, so the polarizing magnet is positioned far from the storage cells—approximately 4 m. The polarizing magnetic field points along the neutron guide axis, and the z direction is transverse to the guide axis. As a result, the polarization must be maintained as the neutrons traverse the ~ 4 m guide system between the polarizing magnet and storage volume, and the neutrons must undergo a 90° spin rotation. A holding field $\sim 30 \mu\text{T}$ is supplied by square Helmholtz pairs along the length of the guide up to the magnetically shielded room (MSR) to prevent depolarization of the neutrons. At that point, the field magnitude must ramp down to the nominal $1 \mu\text{T}$ B_0 field as the

neutrons pass through penetrations in the MSR. A set of spin-transport coils have been designed to generate an optimal ramp for polarization maintenance. Additionally, as the neutrons enter the spin-transport, the combination of fringing magnetic fields from the holding field coils and spin-transport coils rotate the UCN spins to be aligned along \hat{z} . Once inside the MSR, the highly uniform B_0 field dominates and the polarized neutrons propagate into the storage cells. See Chapter 4 for a detailed discussion of the spin-transport coils.

Applied Electromagnetic Fields

The UCN propagate through the guide system on the upstream side of the polarizing magnet for a “fill” time of 50 seconds, after which the storage cells are closed and the Ramsey technique is initiated. The two applied magnetic fields necessary to perform Ramsey’s method of separated oscillatory fields are a static B_0 field and an oscillating “RF” field. The B_0 field is a uniform, 1 μT field aligned along the z direction. It is generated by the B_0 coil, a multiple split coil solenoid with an octagonal cross section. The B_0 field and coil design are a main focus in this dissertation, and the details are covered extensively in Chapter 3. The “RF” field B_1 is a linearly polarized field oscillating at ~ 30 Hz, corresponding to the precession frequency of the neutron spin about the B_0 field. This field is pulsed for approximately 2 seconds before and after a 180 seconds free precession period, representing the “ $\pi/2$ ” pulses.

Along with the magnetic fields, a ~ 12 kV/cm electric field is generated in each cell volume via the application of high voltage to an electrode that forms the bottom and top of the upper and lower storage volumes, respectively. The opposite side of the cylindrical storage cells are ground electrodes, which pair with the high voltage electrode as parallel plates. The resulting E field, assuming a positive voltage on the central electrode, will be in the z direction for the upper storage cell, and the $-z$ direction for the lower. Recalling that B_0 is in the z direction, this two-cell configuration allows for the magnetic and electric field aligned and anti-aligned measurements to occur simultaneously, relaxing the constraint on, for example, field stability corresponding to systematic uncertainty. Each cylindrical storage cell has a height of 10 cm and a diameter of 50 cm. Since the electric field is produced along the axis of the storage cells, the total voltage needed on the high voltage electrode to produce the desired electric field magnitude is 120 kV. The entire double storage cell apparatus is held in a large vacuum chamber to prevent electrical breakdown from the high electric field magnitude.

Magnetically Shielded Room

In order to produce the low magnetic field environment necessary to carry out this neutron EDM measurement, the UCN experimental hall’s background field magnitude, nominally ~ 20 μT , and gradients must be mitigated. A five-layer magnetically shielded room (MSR) has been constructed to provide a one cubic meter central volume with low remnant magnetic field gradient (< 1 nT/m). The room consists of four mumetal layers, providing the low frequency magnetic shielding, and one cop-

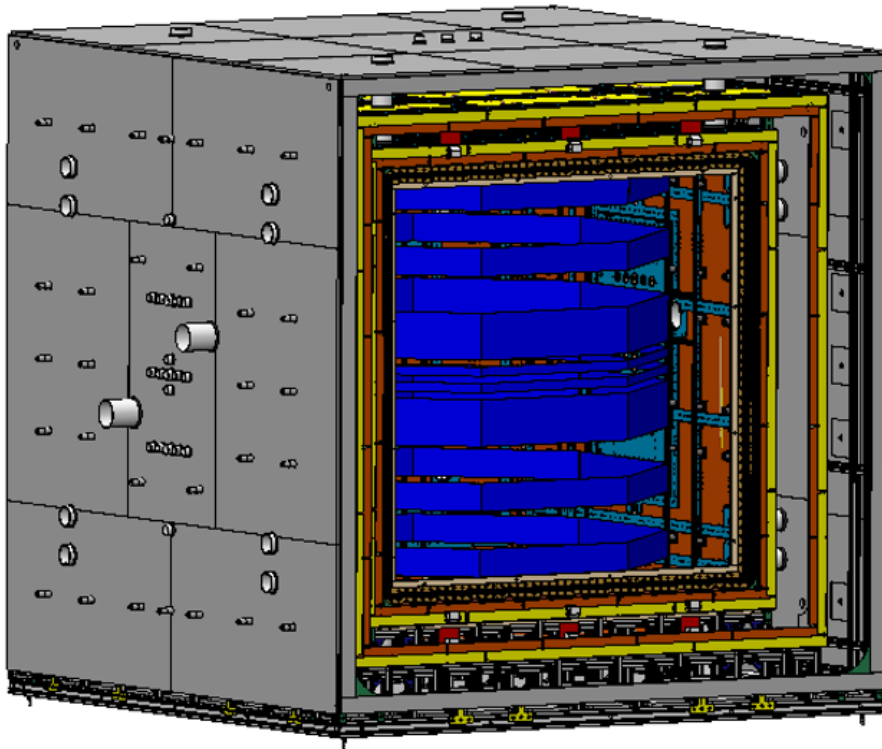


Figure 2.7: CAD model of the LANL-nEDM magnetically shielded room (MSR). The rendering shows the MSR in the “open” orientation, i.e. the door is removed. The B_0 coil is positioned inside of the MSR, shown with blue-colored panels.

per layer, shielding higher frequency magnetic field perturbations. Penetrations exist through the five MSR layers to provide access to the interior of the apparatus for various subsystems, e.g. the neutron guides, vacuum pump, high voltage cable, optical paths for magnetometry, etc.

The mumetal layers can hold remnant magnetization from hysteresis so a degaussing procedure has been developed to optimize the shielding factor of the room. The magnetic environment inside the MSR can also be improved by reducing the magnetic flux incident on each external face. A large array of square, Helmholtz coils, called the “field cage” coils, have been implemented to accomplish coarse external magnetic field control, aiming to minimize the ambient field experienced by the MSR. Internal sources of magnetic field create potentially large field perturbations that are not mitigated by the shielding and are often difficult to quantify. Thus, it is necessary to examine all components which will be located on the interior of the MSR during experimental operation for magnetism, including magnetic impurities within a nominally non-magnetic material.

Simultaneous Spin Analyzers

After the completion of the second RF pulse in the Ramsey cycle, the UCN are allowed to propagate to the one of the two simultaneous spin analyzers, each one corresponding to either the upper or lower storage cell. The simultaneous spin analyzers contain two “arms” with a spin analyzer and a neutron detector. The spin analyzer is a magnetized Fe foil which preferentially allows one spin state to be transmitted while the other spin state is reflected. The neutron detector is a combination of a ^{10}B coated ZnS scintillating screen, which converts the UCN signal into a pulse of photons, and a silicon photomultiplier, which detects the generated photon pulse. On one arm, the simultaneous spin analyzer will include a spin-flipping coil such that the foil on this arm transmits the opposite spin state as the foil in the other arm. In this way, the count of both UCN spin states can be measured simultaneously. The ratio of spin-up to spin-down UCN measured is used to extract the neutron EDM value via deviation from expected ratio derived from the Ramsey method with $d_n = 0$.

Magnetometry

Magnetometry provides access to magnetic field measurements during experimental operation. Two types of magnetometry will be employed in the LANL-nEDM experiment: comagnetometry and external magnetometry. The comagnetometer is a companion species introduced into the same volume as the neutrons to allow a simultaneous EDM measurement. In the case where the EDM of the companion species is known to be much smaller than the neutron EDM, the effect of the electric field on the companion species can be neglected. The spin precession of the companion species would then depend only on the magnetic field, ultimately serving to suppress magnetic field effects such as time varying magnetic field magnitude and fields from HV leakage current. The LANL-nEDM experiment will use ^{199}Hg as the magnetometer because it has an EDM $|d_{\text{Hg}}| < 7.4 \times 10^{-30} e \cdot \text{cm}$ (90% CL) [42], which is nearly 3 orders of magnitude below the goal measurement sensitivity, and the spin precession can be probed using optical techniques. The systematic effects associated with a ^{199}Hg magnetometer for neutron EDM searches using UCNs is well understood [43][44][45]. A polarized UV laser will be used to optically pump and probe the mercury vapor. When the optical paths for the laser light pass through the each UCN storage volume, the spin-dependent interaction between the light and the mercury vapor modulates the transmission amplitude of the light. The Larmor precession frequency of the ^{199}Hg , and therefore the magnetic field magnitude, can be extracted from this signal.

The external magnetometry, meaning external to the UCN storage volumes, makes use of ^{199}Hg in a similar fashion. The mercury vapor is contained within a glass cylinder. The size of the glass cylinder determines the resolution of the magnetic field measurement since the enclosed vapor will sample the entire interior volume. A special coating is applied to the glass surface to minimize spin-relaxation, which improves the precision of the measurements [46]. Many individual magnetometer cells form an array of locations at which the magnetic field magnitude can be probed via

Table 2.2: Expected statistical sensitivity of the LANL-nEDM experiment [41]. T_{cycle} takes into account the time for loading, unloading, free precession period, and dead time associated with a single measurement. It should be noted that the times for achieving the sensitivities are live days/years. Given the operational schedule of the linear accelerator and other considerations, one live year of data taking will take approximately 5 calendar years.

Parameters	Values
E (kV / cm)	12
N (per cell)	39,000
T_{FP} (sec)	180
T_{cycle} (sec)	300
AP_{det}	0.8
σ /day ($10^{-26}e\cdot\text{cm}$)	4
σ /year ($10^{-27}e\cdot\text{cm}$)	2.1
90% C.L./year ($10^{-27}e\cdot\text{cm}$)	3.4

polarized UV laser. Using Maxwell’s equations, well placed magnetometers external to the storage volumes provide information about the magnetic field present within the UCN storage volumes.

2.3 Statistical Uncertainty and Sytematic Effects

The overall sensitivity of the experiment can be broken down into statistical uncertainty and systematic effects. The statistical uncertainty is

$$\sigma_{d_n} \sim \frac{1}{EAP_{det}T_{FP}\sqrt{M}\sqrt{N}} \quad (2.24)$$

where E is the electric field magnitude, A is the simultaneous spin analyzer efficiency, P_{det} is the polarization of the neutron population at the detector location, T_{FP} is the free precession period in the Ramsey cycle, M is the number of experimental cycles, and N is the average number of neutrons detected in one experimental cycle. Table 2.2 shows the expected values of these listed parameters, allowing the experiment to achieve the goal sensitivity of $3 \times 10^{-27}e\cdot\text{cm}$.

Due to the fact that data taking has not commenced, the systematic effects for the LANL-nEDM experiment can only be assumed based on previous neutron EDM searches implementing similar methodology. Based on the systematic effects seen in the latest Sussex-ILL experiment and the sources of those effects [2], one can extract the necessary control measures which must be implemented to meet the goal sensitivity. Table 2.3 shows the reported systematic errors in the 2020 updated analysis of the ILL neutron EDM experiment. Many of these systematic effects will be removed from the LANL-nEDM experiment by design. For example, the magnetometry will be probed using laser light which greatly reduces the ν_{Hg} light shift effect, and the dipole field effect is nearly eliminated by a strict materials scanning routine. Other

Table 2.3: Systematic errors reported in the 2020 updated analysis of the ILL neutron EDM experiment [2]. The units of the effects are $10^{-28} e\cdot\text{cm}$.

Effect	Shift	σ
Error on $\langle z \rangle$	-	7
Higher order gradients \hat{G}	69	10
Transverse field correction $\langle B_T^2 \rangle$	0	5
Hg EDM [42]	-0.1	0.1
Local dipole fields	-	4
$\vec{v} \times \vec{E}$ UCN net motion	-	2
Quadratic $\vec{v} \times \vec{E}$	-	0.1
Uncompensated G drift	-	7.5
Hg light shift	-	0.4
Inc. scattering ^{199}Hg	-	7

systematic effects depend on the experimental control and knowledge, e.g. employing magnetometry to closely monitor magnetic field drifts.

This section will focus on key uncertainties and systematic effects within the scope of this thesis work, i.e. related to the B_0 and spin-transport magnetic field gradients.

Geometric Phase Effect

It is most crucial to control for systematic effects that scale linearly with the E field because such an effect would be interpreted as an EDM. This is precisely the case for the so-called “geometric phase” effect—a well known phenomenon in permanent EDM measurements using trapped particles, atoms, and molecules [47]. The geometric phase results from the combination of B_0 magnetic field gradients and the motion of the UCN during the storage time. To understand the source of this effect and why it is inherent to the experimental method employed, a derivation is outlined below (following from [47], [48]).

Suppose a neutron stored within a cylindrical container with a uniform $\vec{B}_0 = B_0 \hat{z}$ applied magnetic field. The spin will undergo Larmor precession at angular frequency $\omega_0 = \gamma_n B_0$. In a reference frame rotating at an angular velocity $\vec{\omega}_r$, with $\vec{\omega}_r$ parallel to $\vec{\omega}_0$, the precession frequency will be shifted. The precession frequency in the rotating frame $\Delta\omega = \omega_0 - \omega_r$ can be understood as Larmor precession about an effective magnetic field

$$\vec{B}_{eff} = -\frac{\Delta\omega}{\gamma_n} = \left(\vec{B}_0 - \frac{\vec{\omega}_r}{\gamma_n} \right)$$

A second magnetic field \vec{B}_{xy} perpendicular to \vec{B}_0 is introduced such that the total magnetic field in the lab frame and rotating frame are:

$$\begin{aligned} \vec{B}_{lab} &= \vec{B}_{xy} + \vec{B}_0 = B_{xy} (\cos(\omega_r t) \hat{x} + \sin(\omega_r t) \hat{y}) + B_0 \hat{z} \\ \vec{B}_{rot} &= B_{xy} \hat{x} + B_{eff} \hat{z} \end{aligned} \tag{2.25}$$

Using B_{rot} , the neutron spin precession frequency in the rotating frame can be written as:

$$\omega_{n-rot} = \gamma_n B_{rot} = \gamma_n \left[B_{xy}^2 + \left(B_0 - \frac{\omega_r}{\gamma_n} \right)^2 \right]^{\frac{1}{2}} \quad (2.26)$$

Now, an angular frequency shift away from the Larmor frequency due to this rotating B_{xy} magnetic field can be determined:

$$\begin{aligned} \omega_{shift} &= \omega_{n-rot} - \omega_0 \\ &= (\omega_0 - \omega_r) \left[1 + \frac{\omega_{xy}^2}{(\omega_0 - \omega_r)^2} \right]^{\frac{1}{2}} + (\omega_r - \omega_0) \end{aligned} \quad (2.27)$$

where $\omega_{xy} = \gamma_n B_{xy}$. In the limit $B_{xy} \ll \left(B_0 - \frac{\omega_r}{\gamma_n} \right)$:

$$\omega_{shift} \approx \frac{\gamma_n^2 B_{xy}^2}{2(\omega_0 - \omega_r)} \quad (2.28)$$

The frequency shift in Eq. 2.28 is a well known phenomenon called the Bloch-Siegert shift. In order for such a shift to occur, there must exist some source of oscillating magnetic field transverse to the B_0 magnetic field. Given only static fields are applied to the neutron, one might suspect that the frequency shift would vanish, assuming there would not exist a candidate oscillating B_{xy} . However, time varying magnetic fields in the neutron reference frame will be present, even in a static field, if non-zero spatial field gradients are combined with motion through the field [49]. An example pertaining to the LANL-nEDM experiment is presented below.

A physically realized B_0 magnetic field will contain a non-zero gradient along the nominal field direction, namely $\partial B_{0z}/\partial z$. Under the assumption that the region of interest is free from magnetic field sources, Maxwell's equations require a corresponding radial field in the $z = 0$ plane:

$$\vec{B}_{0r} = -\frac{r}{2} \frac{\partial B_{0z}}{\partial z} \hat{r}$$

Cylindrical coordinates are chosen to match the geometry of the storage cells for the LANL-nEDM experiment with the axis of the cylindrical cells aligned along z . As discussed in 2.1, the neutron EDM measurement method employed requires the application of an electric field \vec{E} across the storage cell volume. The UCN within the cell will experience a motional magnetic field dictated by special relativity:

$$\vec{B}_{mot} = \frac{\vec{E} \times \vec{v}}{c^2} \quad (2.29)$$

where \vec{v} is the velocity of the neutron. In the reference frame of the neutron, the effective magnetic field is

$$\begin{aligned} \vec{B}_{eff} &= \vec{B}_{0r} + \vec{B}_{mot} \\ &= -\frac{r}{2} \frac{\partial B_{0z}}{\partial z} \hat{r} + \frac{\vec{E} \times \vec{v}}{c^2} \end{aligned} \quad (2.30)$$

Table 2.4: The expected experimental parameters for the LANL-nEDM experiment [41]. These values are estimated from previous experimental work in the field [2] [42] as well as research and development conducted at LANL. Note: $\omega_r \equiv \frac{v_\phi}{\rho}$.

Parameter	Value
ρ	0.5 m
v_ϕ	5 m/s
E	12 kV/cm
ω_r	10 s ⁻¹
ω_0	183.2 rad/s

Assuming the neutrons undergo specular reflection when interacting with the cell walls, the neutron velocity will precess around the z axis. Thus, \vec{B}_{eff} will oscillate in the xy plane similar to \vec{B}_{xy} from the Bloch-Siegert shift derivation. The induced frequency shift can be found by plugging in \vec{B}_{eff} to Eq. 2.28:

$$\begin{aligned} \omega_{shift} &= \frac{\gamma_n^2 B_{eff}^2}{2(\omega_0 - \omega_r)} \\ &= \frac{\gamma_n^2 \left(-\frac{r}{2} \frac{\partial B_{0z}}{\partial z} \hat{r} + \frac{\vec{E} \times \vec{v}}{c^2} \right)^2}{2(\omega_0 - \omega_r)} \end{aligned} \quad (2.31)$$

where ω_r is the angular frequency of the neutron's velocity.

Expanding the numerator, one will find that the cross term in linear in \vec{E} which will not average to zero when considering a population of neutrons with equal probability of net rotational motion in the clockwise and counter-clockwise directions. The LANL-nEDM experiment extracts the neutron EDM via a phase difference between the neutron populations in two cells—one with the E field aligned along B_0 and one with the E field anti-aligned with B_0 . The phase difference resulting from the shift in Eq. 2.31 is:

$$\Delta\omega_{\uparrow\uparrow} - \Delta\omega_{\uparrow\downarrow} = -\frac{\gamma_n^2 \rho v_\phi E}{c^2} \frac{\partial B_{0z}}{\partial z} \frac{|\omega_r|}{(\omega_0^2 - \omega_r^2)} \quad (2.32)$$

where ρ is the radius of the cylindrical UCN storage cells.

The upper limit on the gradient can be calculated from this formula using the goal sensitivity and expected parameters. The LANL-nEDM goal sensitivity is 3×10^{-27} e·cm, corresponding to a frequency shift of 1.09×10^{-7} rad/s in each cell. Plugging the experimental parameters (see Table 2.4) into Eq. 2.32 and solving for the gradient, the upper limit on $\partial B_{0z}/\partial z$ is found to be:

$$\frac{\partial B_{0z}}{\partial z} \leq 0.3 \text{ nT/m} \quad (2.33)$$

Polarization Product

The polarizing magnet provides a UCN population with $> 99\%$ polarization. After passing through the polarizing magnetic field, the neutrons propagate throughout

the guides and storage cells for ~ 250 seconds—the sum of the fill, storage, and dump times—before reaching the detector. The UCN population is likely to have a decreased polarization from interactions with magnetic field gradients during this approximately four minute period, leading to decreased Ramsey fringe contrast and decreased statistical reach of the experiment. Two concerning sources of depolarization are spin relaxation during free-precession and non-adiabatic transport through the MSR mumetal layers.

Ramsey’s method of separated oscillatory fields as described in Section 2.1 assumes a uniform B_0 magnetic field. Under this assumption, each neutron in the storage cell are precessing at the same rate, $\omega_0 = \gamma_n B_0$, regardless of position. Thus, the initial polarization P_0 of the neutron population is conserved. The transverse phase of each neutron will depend on the average magnetic field experienced. If the magnetic field contains spatial gradients, which must be true for any physical magnetic field produced, neutrons that sample the storage cell volume differently could experience different average magnetic field magnitudes. For example, a neutron n_1 with kinetic energy KE_1 will generally have an average z position that is lower than a neutron n_2 with kinetic energy $KE_2 > KE_1$ due to the gravitational potential energy associated with z . In combination with a linear gradient $\partial B_z / \partial z > 0$, the neutron with a larger average z will also see a larger average magnetic field, resulting in a larger accumulated phase.

The dephasing that occurs during the free-precession period is called transverse spin relaxation. The characteristic time scale T_2 of the dephasing for a cylindrical geometry is given by [50]:

$$T_2 = \left[\frac{1}{2T_1} + \frac{\gamma_n^2 h^4}{120D} \left(\frac{\partial B_z}{\partial z} \right)^2 + \frac{2\gamma_n^2 R^4}{96D} \left(\frac{\partial B_z}{\partial \rho} \right)^2 \right]^{-1}$$

$$D \approx |v| \frac{hR}{2(h+R)}$$

where T_1 is the longitudinal spin relaxation time, h is the height of the storage cell, R is the radius of the storage cell, and v is the neutron velocity. The LANL-nEDM values for these variables along with the gradient specification from the geometric phase can be used to estimate $T_2 \sim 10^5$ s, which leads to a decrease in polarization of $\approx 1 - \exp(180/10^5) \approx 0.002$, which is negligible depolarization. Therefore, the constraint on the magnetic field gradient from the geometric phase is stringent enough for the spin relaxation as well.

External to the MSR, the ambient magnetic field magnitude is $\sim 20 \mu\text{T}$. Given the B_0 field magnitude within the MSR is $1 \mu\text{T}$, the neutrons must experience a substantial magnetic field gradient as they pass through the layers of magnetic shielding. The rate at which the field changes needs to meet the adiabatic condition $\kappa \gg 1$ (as described in Section 4.1) in order to maintain the neutron polarization in this transition region, κ being the adiabaticity parameter [51]:

$$\kappa = \frac{\omega_L}{\omega_{grad}} \tag{2.34}$$

where $\omega_L = \gamma_n |\vec{B}|$ is the Larmor precession angular frequency about a magnetic field \vec{B} and ω_{grad} is the angular frequency of the magnetic field seen by the UCN.

$\kappa \gg 1$ implies that the speed at which the neutron spin precesses about the magnetic field is much larger than the fractional rate of change of the magnetic field in the rest frame of the neutron. A system of spin-transport coils have been designed to provide an optimal magnetic field taper in the region within the MSR penetrations. An in-depth discussion of adiabaticity, the field taper design method, and particle tracking simulation results are contained in Chapter 4.

Chapter 3 Highly Uniform B_0 Coil

The B_0 coil provides the static, highly-uniform magnetic field for the LANL-nEDM experiment. As described in Section 2.3, the field gradients present in the UCN storage cells are associated with systematic effects crucial to the experiment’s measurement sensitivity. Thus, the primary consideration in the B_0 coil design is optimizing the field uniformity in the fiducial volume. The engineering constraints related to part fabrication and operation of the experiment are also important factors in designing the B_0 coil geometry. Since many features of the B_0 coil are driven by these physical constraints, this chapter begins by introducing the coil design and highlighting features meant to accommodate the LANL-nEDM apparatus.

3.1 B_0 Coil Design

The B_0 coil is a multiple split solenoid with an octagonal cross section. In total, there are eight coil sections separated by seven gaps. The four sections nearest to the center of the B_0 coil are the “inner” sections, which are connected in series and excited with current $I_{in} \approx 3.5$ mA. Similarly, the remaining four “outer” sections are connected in series and excited with current $I_{out} \approx 1.82I_{in}$, where I_{out}/I_{in} is chosen to minimize gradients in the UCN storage volume (see Section 3.2). The exact current values will vary depending on the operating conditions present in the LANL experimental hall. For example, ambient temperature changes can alter the magnetic response of the MuMetal layers, and thermal expansion/contraction from ambient temperature shifts can affect the interaction between adjacent sheets of MuMetal. The height and width of the B_0 coil are 2.243 m and 2.131 m, respectively. Refer to Section 3.2 for a detailed breakdown of the various coil section and gap dimensions. Take note of the labels for the gaps and coil sections in Fig 3.1 as these will be referenced throughout the chapter. In addition, the cardinal directions will be used to specify particular coil faces (e.g. the Northwest face). The apparatus is oriented such that the neutrons enter the MSR through the South face, and the MSR door is located on the West side. The split solenoid design provides a high degree of flexibility in the size and position of the gaps, allowing access planes to the interior of the B_0 coil for various subsystems detailed below.

Magnetometry

The magnetometry for the LANL-nEDM experiment must be pumped and probed using linearly polarized UV laser. Thus, there must exist an optical path through the B_0 coil volume corresponding to the position of each magnetometer that will be monitored. The comagnetometry, a ^{199}Hg vapor that co-inhabits the UCN storage volume, will be probed at the center of each storage cell. An array of five external magnetometers will also be implemented on the plane centered between the storage cells. The optical paths necessary to probe these magnetometers are accommodated

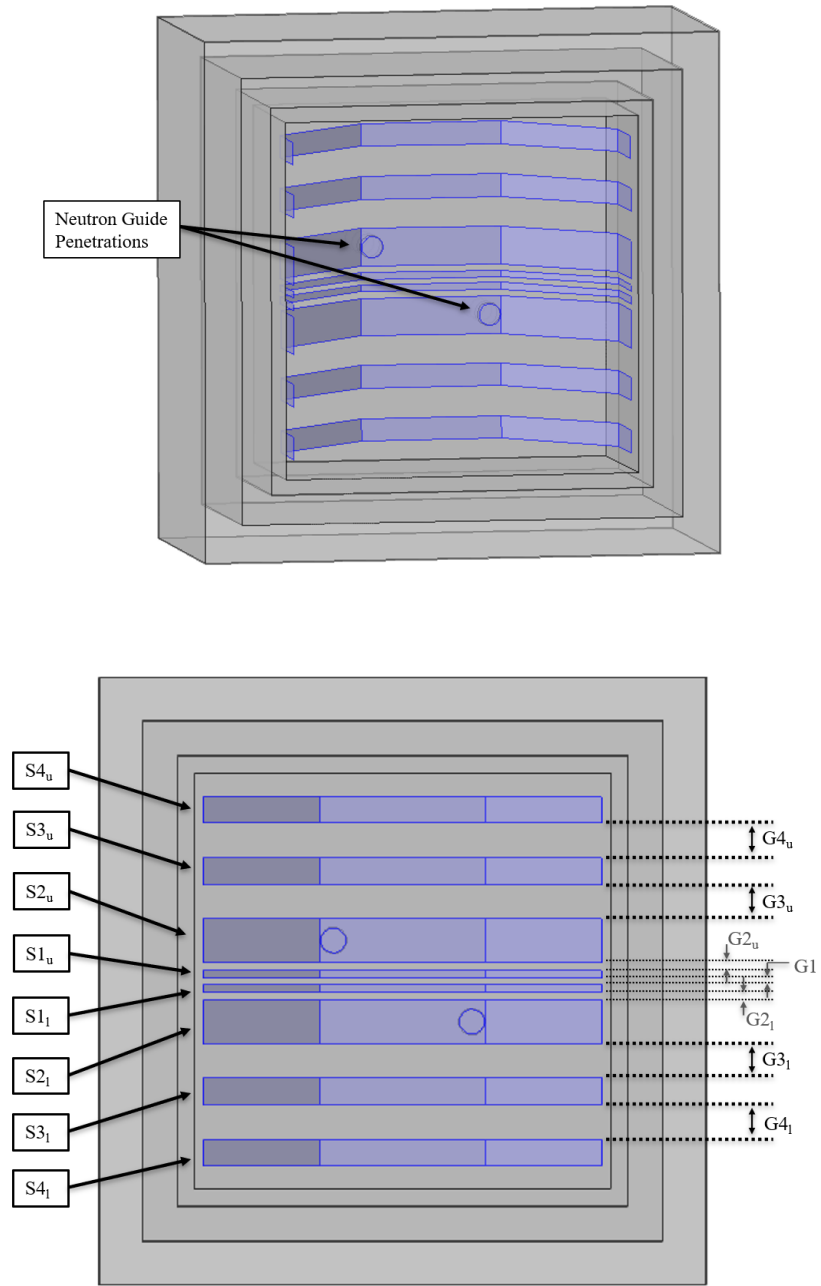


Figure 3.1: CAD renderings showing the B_0 coil in a 3D view to give perspective of the octagonal shape (TOP) and a 2D view with the labels for gaps and coil sections (BOTTOM).

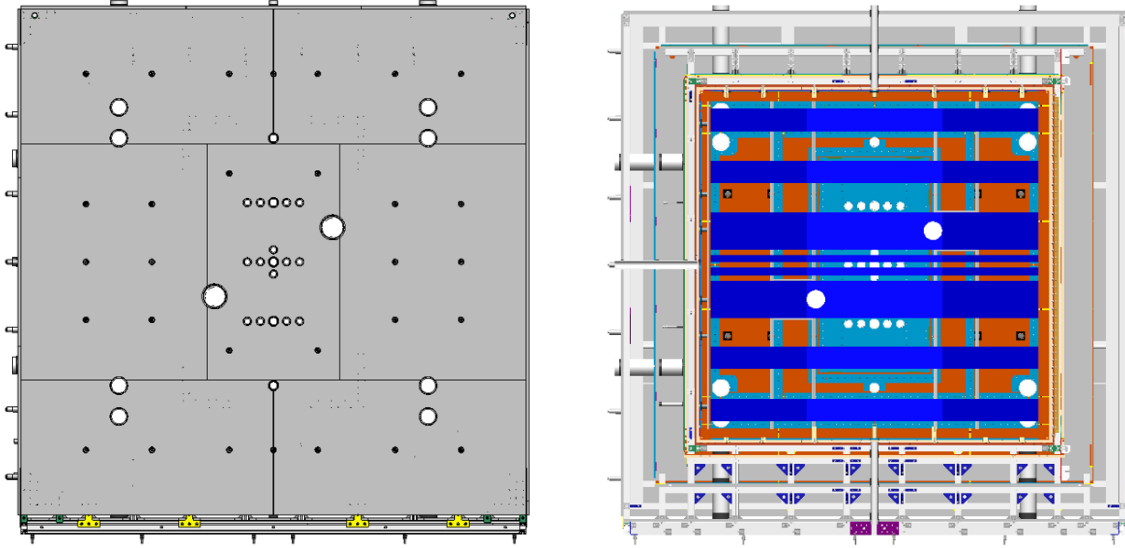


Figure 3.2: CAD models of the LANL MSR and the B_0 coil. The LEFT image shows the North side of the MSR, which includes the penetrations corresponding to the neutron guide locations, magnetometry, etc. The RIGHT image shows the interior of the MSR with the B_0 coil in place. In this view, one can see how the placement and dimension of each coil section accommodates the various penetrations.

by the three gaps nearest to the center of B_0 coil: gaps G1, G2_u, and G2_l (see Fig. 3.2). Gap G1 is able to accommodate all five external magnetometers since they are in the same z plane. Gaps G2_u and G2_l align with the center of the UCN storage cells, which is also the height at which the ^{199}Hg comagnetometer will be probed. The mercury vapor will be pumped via a longitudinally polarized pulsed laser with optical paths through gaps G3_u and G3_l.

Since each coil gap provides access in an entire z plane, the coil design provides the opportunity to relocate, or even expand, the external magnetometer array to any position where a gap exists without coil design alteration. Such an action would require a modification of penetrations in the MSR, which has small penetrations for each optical path anticipated for the experiment. In consideration for future upgrades or expansion to magnetometry, the MSR optical path penetrations exist on a removable MuMetal panel which can be redesigned as the experiment evolves.

Neutron Guides and High Voltage Cable

Within the coil gaps, the magnetic field gradients are large enough to cause depolarization of the UCN population. Therefore, the neutron guides should not enter the interior of the B_0 coil via one of the gaps. Instead, the guides are passed through penetrations in sections S2_u and S2_l. The current incident with the penetration boundary is rerouted around the penetration perimeter. At these penetration locations, the B_0 coil interfaces with the spin-transport coils to mitigate field perturbations resulting from the rerouted current distribution. The neutron guides only pass through the

south side of the coil so the guide penetrations could be removed from the north coil faces. It was decided that the penetrations should be on both the north and south faces to mitigate magnetic field asymmetry in the UCN storage volume. Without neutron guides on the north side, these penetrations can be used for other subsystems to access the interior volume of the B_0 coil, such as the high voltage (HV) system. The HV is applied to the center electrode via a high voltage cable. The correspondingly large bend radius limits the displacement between the HV vacuum feed-through and the location at which the cable enters the interior volume. Using the B_0 penetrations to route this cable prevents the need to provide a large gap near the mid-plane of the coil, which would reduce magnetic field uniformity.

Magnetic Field Mapping

Knowledge of the magnetic field is key to the success of the LANL-nEDM experiment. A deep understanding of the magnetic field gradients in the fiducial volume allows for optimization of the control measures available, e.g. environmental controls, degaussing, tuning the B_0 current ratio, adjusting the external field cage, and calibrating shim coils. The B_0 coil geometry is amenable to many different field measurement strategies. Measuring the field during experimental operation is accomplished via the magnetometry discussed above. When the apparatus is not assembled inside the MSR, other methods of field measurement are preferred. An array of optically probed magnetometers could be implemented at $\sim 50 \mu\text{T}$ —the magnitude of the geomagnetic field—taking into consideration complications from, for example, the nonlinear Zeeman effect [52]. To measure the magnetic field at multiple locations, one can build a stationary array where the number of probes is equivalent to the number of locations, or a small number of probes—typically one—can be moved to many different locations measurement points. An array of magnetic field probes is easily accommodated by the B_0 coil as the associated electronics can be routed through the numerous gaps available. A system which translates probes through the interior volume provides more stringent geometric constraints.

The B_0 coil is designed for an H-frame mapping system similar to a gantry. Two large I-beams form the main structure of the mapper, and these must be supported externally from the MSR to prevent excess load and vibrations experienced by the MSR. Aluminum is the candidate material for the rails due to its favorable, i.e. nonmagnetic, properties. Given the strength of aluminum, the projected weight of the mapping system, and the length of the rails, which must be greater than 3.5 m to span the MSR outer dimension, the I-beam profile must be made large to rigidly support the mapping apparatus. Gap G3_u and corresponding penetrations through the MSR layers provide a path for I-beam rails with flanges and web up to 7 inches. See Section 3.4 for more details of the H-frame magnetic field mapping system.

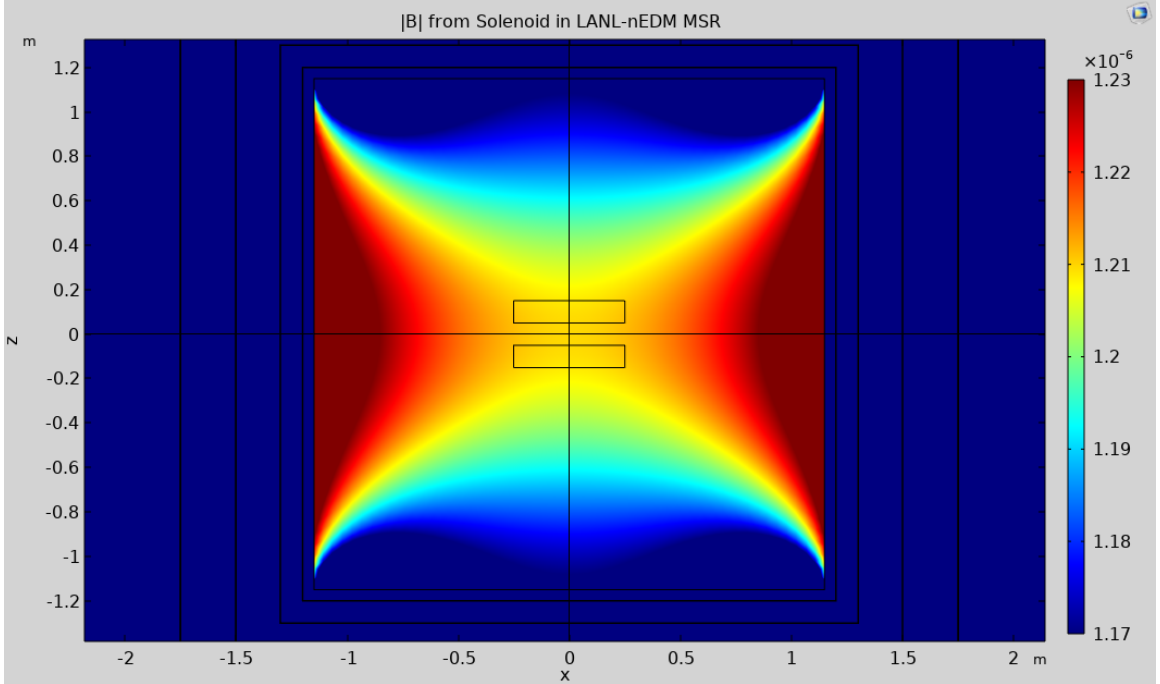


Figure 3.3: Color map of $|\vec{B}|$ of a large solenoid housed inside the LANL-nEDM MSR. The 2D cross section shown is the $y = 0$ plane. The coil height and diameter are 2.3 m. The volume averaged magnitude of the vertical gradient of the B_z component in the UCN storage volume is $1 \mu\text{T}$ is $\langle |\partial B_z / \partial z| \rangle = 8.39 \text{ nT/m}$. Note: The gradient calculation is normalized to a central field magnitude $|B_0| = 1 \mu\text{T}$.

3.2 Magnetic Field Optimization

Gapped Solenoids

Nearly all physics students will be familiar with the popular example of a uniform magnetic field generated by an infinitely long solenoid [53],[54]. An approximately infinite length solenoid—meaning much longer than the length of the UCN storage volume—would provide a magnetic field which meets the uniformity specification for the LANL-nEDM experiment. This of course ignores many of the experiment’s physical considerations such as the implementation of magnetic shielding surrounding the apparatus to control the ambient magnetic field magnitude and gradients. Since the B_0 coil is located within the MSR, the inner dimensions of the MSR are the practical limitation on the maximum coil size, allowing a maximum length and diameter less than 2.4 m. The magnetic shielding boundary conditions can be viewed as image currents, effectively increasing the length—equivalently the magnetic field uniformity—of the enclosed solenoid. Using finite element analysis, the average magnetic field gradient $\langle |\partial B_z / \partial z| \rangle$ for a maximally large solenoid inside the MSR can be calculated to be 8.39 nT/m (see Fig. 3.3). For comparison, the specified magnetic field gradient for the LANL-nEDM experiment is $\langle |\partial B_z / \partial z| \rangle \leq 0.3 \text{ nT/m}$, a factor of 28 lower gradient than the field provided by the solenoid.

The magnetic field uniformity in the central field volume of a finite length solenoid can be improved by the inclusion of a gap at the center of the solenoid [55]. Assuming a solenoid in free space has a current distribution that is well represented by a current sheet, the optimal gap length can be calculated analytically [56]. Near the center of a gapped solenoid, the magnetic flux density will increase as $|z|$ increases. The opposite behavior occurs for the central region of a finite solenoid where the magnetic flux is decreasing for larger $|z|$ positions. As shown in Fig. 3.4, the combination of these fields results can result in higher field uniformity in the central volume. The resulting current distribution from the combined solenoid and gapped solenoid is a double-gapped solenoid. An interesting feature of this current distribution is the ability to tune the ratio of the outer current (the gapped solenoid current) to the inner current (the central solenoid current) as a means of minimizing gradients [57],[36].

B_0 Optimization

The optimized B_0 coil geometry must simultaneously satisfy the physics constraints (i.e. the magnetic field gradient specification) and the engineering constraints (discussed in section 3.1). Both sets of constraints are equally important to the success of the experiment, and they have some interplay. The magnetic field provided by the B_0 coil is fully determined by the current distribution and the magnetic boundary conditions present. The engineering constraints determine the nature of the boundary conditions and place limits on the available volume for currents. A convenient feature of the multi-split solenoid design is the ability to accommodate many geometric constraints, allowing for flexibility in the engineering constraints without the risk of drastic coil redesign. Given the general nature of the coil geometry and boundary conditions, the tool chosen to complete the B_0 coil geometry optimization was finite element analysis (FEA) software, namely COMSOL Multiphysics.

The B_0 COMSOL model used for parameter optimization contains uniform 2D current sheets inside a multi-layer MuMetal enclosure (see Figure 3.5). The current sheet approximates multiple parallel current-carrying traces which greatly reduces the time and computational resources required for each FEA simulation. The model used for parameter optimization does not include the neutron guide penetrations through sections $S2_u$ and $S2_l$ since the effect of the associated rerouted current is mitigated by the spin-transport coils—Chapter 4 contains a detailed discussion of the spin-transport coil contribution to the B_0 field. The penetrations in the MSR are also ignored for this initial optimization.

The optimal B_0 coil parameters will minimize the magnetic field gradients within the UCN storage cells, most importantly $\langle |\partial B_z / \partial z| \rangle$. A search of the parameter space was conducted in COMSOL via parametric sweeps. The following parameters were included in the optimization: total number of sections, section widths, section positions, and section currents. The number of free parameters is reduced greatly if mirror symmetry across the xy plane is prescribed to prevent production of odd magnetic field gradients. There are also physical considerations, e.g. the inner dimension of the MSR physically bounds the total B_0 coil height and width.

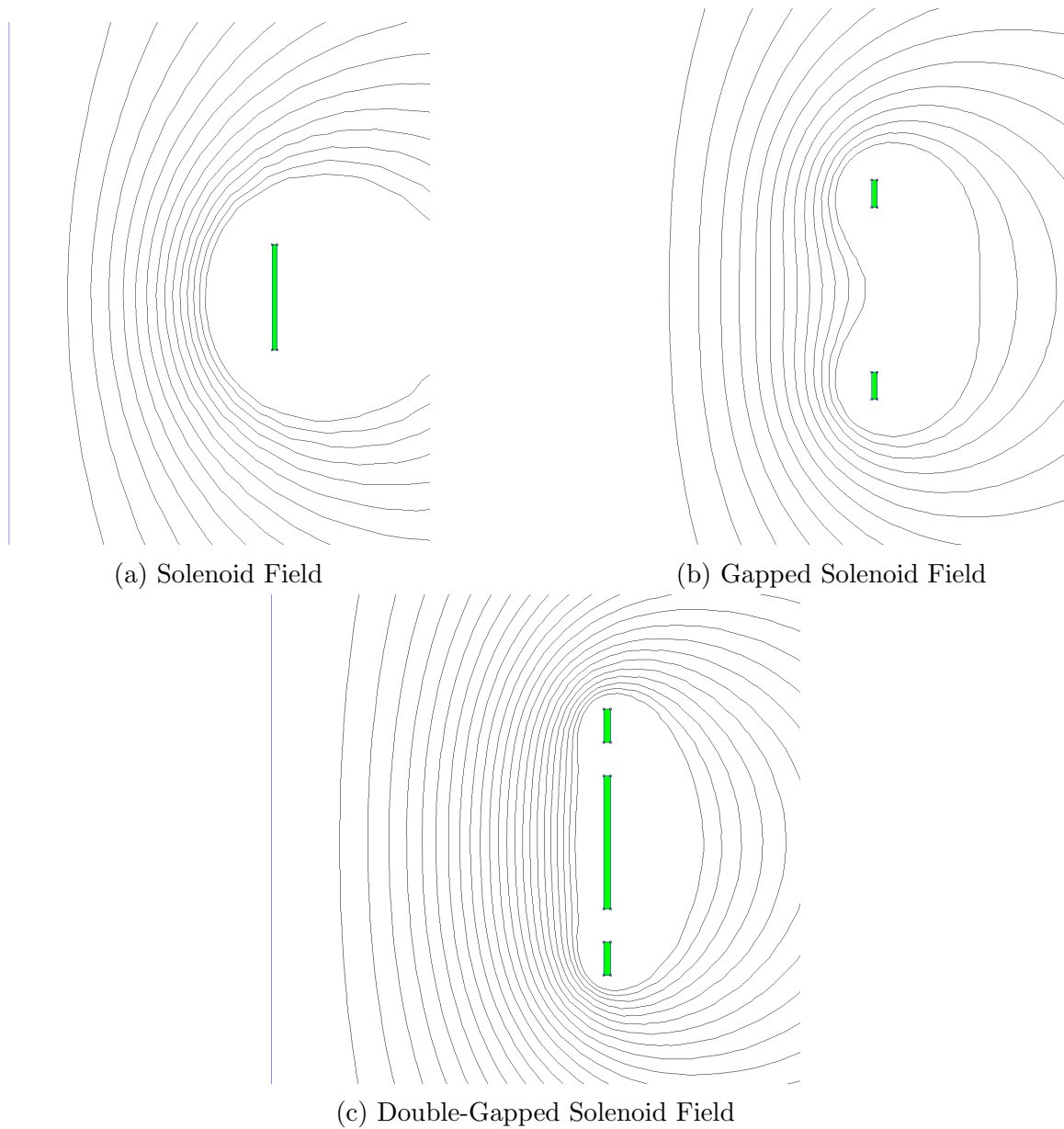


Figure 3.4: This set of images shows magnetic flux lines from a solenoid (a), gapped solenoid (b), and double-gapped solenoid (c) calculated using a 2D axis-symmetric finite element simulation—the left side of each image being the axis of symmetry. The green in each image represents the current density oriented into the page. Note that the solenoid field diverges as distance from the center increases. On the other hand, the gapped solenoid field lines converge, up to some point, moving away from the center of the system. Thus, the linear combination of these two fields, given that their magnitudes are approximately equal, will produce straighter flux lines near the center of the system. This effect is represented in (c), where the field is produced by the combination of the solenoid and gapped solenoid coils.

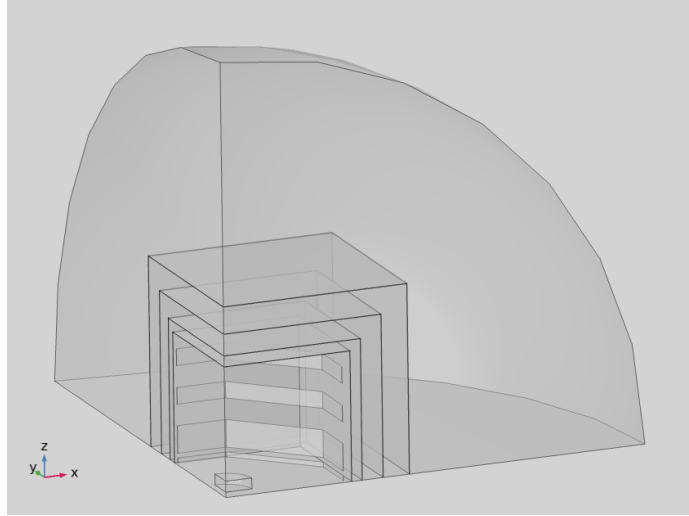


Figure 3.5: Simplified COMSOL model of B_0 and the LANL-nEDM MSR used for optimization of the B_0 coil parameters. This simplified geometry does not include penetrations in the B_0 coil faces or the MSR walls. Without these penetrations, the system has a $\pi/4$ rotational symmetry about the z axis and a mirror symmetry about the $z = 0$ plane. In this case the system can be simulated in just one octant with the application of proper boundary conditions.

As discussed in Section 3.1, there are various subsystems which need unobstructed access to the interior of the B_0 coil. Generally, these access locations are provided in the form of gaps in the B_0 coil surface. The span of z corresponding to each access location is defined as a “keepout” zone in the optimization routine, meaning that the coil current sheets must not intersect those regions. A notable exception is the neutron guide access, which is provided by a penetration in sections $S2_u$ and $S2_l$ of the B_0 coil. The motivation for bringing the neutron guides through the coil faces comes from spin-transport optimization, discussed in Chapter 4.

The optimal design with the simplified geometry approximation is used as the starting point for a parameter sweep with a higher fidelity model. Here, the symmetry planes are removed, permitting the inclusion of asymmetric features such as the MSR penetrations. Modeling the full system also presents the opportunity to investigate the effect of expected tolerances, discussed in Section 3.3. In the physical implementation, the B_0 coil faces are PCB panels with horizontal traces to carry the current. The trace widths were chosen to be 2.5 mm with 3 mm spacing center to center for manufacturing considerations. Thus the optimized coil parameters had to be adjusted such that the current sheet widths were integer multiples of 3 mm. The optimal current ratio shifts from 1.75 to 1.82 when the PCB widths are included in the model. These adjusted widths are reported as the final design values shown in Table 3.1.

The table shown in Figure 3.7 lists the various gradients extracted from the optimized B_0 COMSOL model. The exact values are listed here for completeness, although it is not expected that the physical magnetic field can achieve this level of

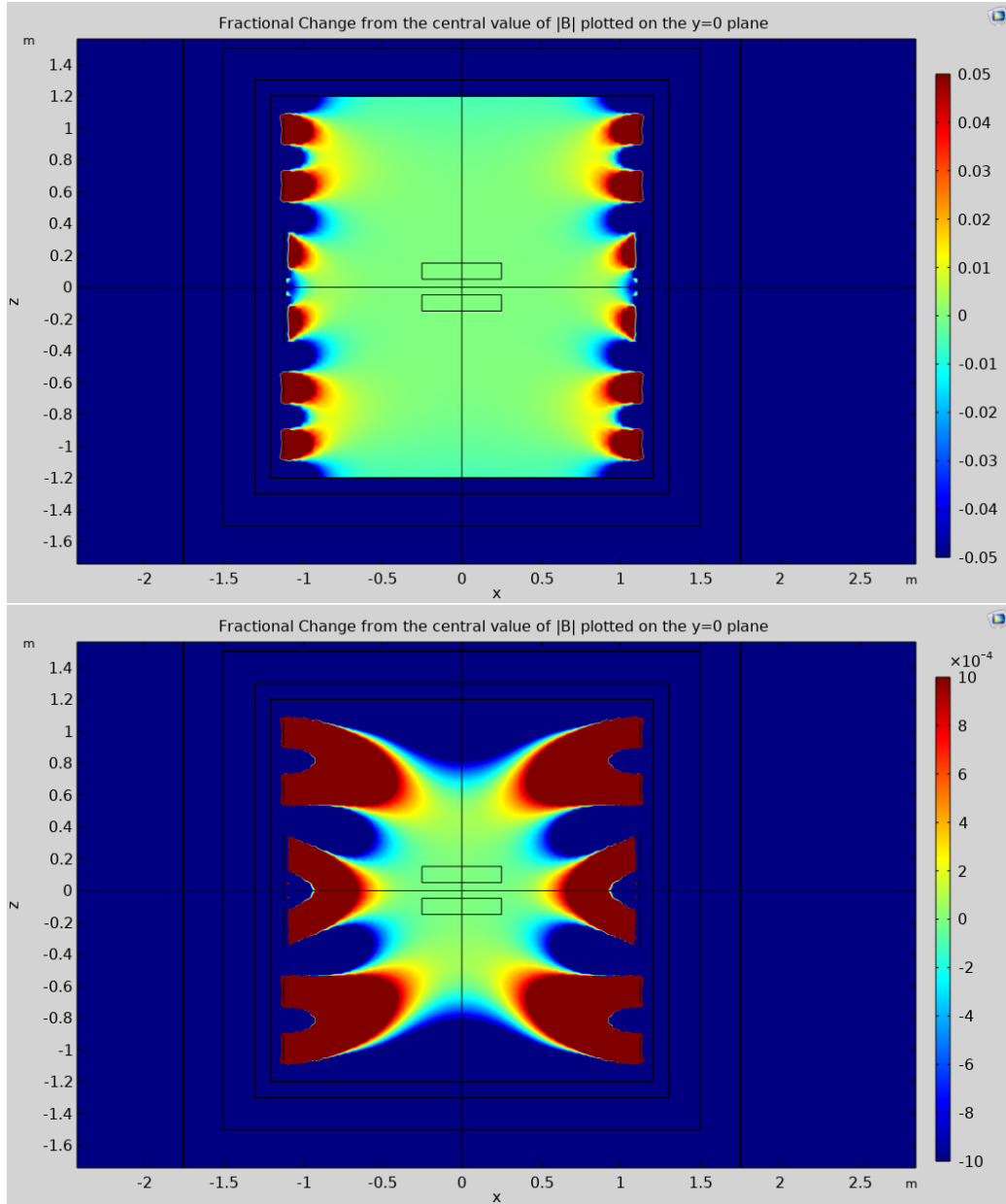


Figure 3.6: Color maps of fractional change in $|\vec{B}|$ from the central value $|B_0| = 1 \mu\text{T}$ produced by the optimized B_0 coil within the LANL-nEDM MSR. The top image shows a plot of the field profile with a scale of $\pm 5\%$. The bottom image shows a plot of the same values with a smaller scale: $\pm 0.1\%$.

Table 3.1: List of the optimized coil parameters for the B_0 coil. These values were established using parameter sweeps in COMSOL to minimize the volume averaged gradient magnitude $\langle |\partial B_z / \partial z| \rangle$ in the UCN storage cells. The listed coil section positions correspond to the minimum z position of the section. Only the sections located on the upper half of the coil are shown; the lower section parameters can be derived using mirror symmetry across the $z = 0$ plane.

B_0 Coil Parameter	Value
Total width	2.243 m
Total height	2.131 m
Current Ratio (I_{out}/I_{in})	1.820
S1 _u z position	15.8 mm
S1 _u height	51 mm
S2 _u z position	107.9 mm
S2 _u height	252 mm
S3 _u z position	560.0 mm
S3 _u height	150 mm
S4 _u z position	915.6 mm
S4 _u height	150 mm

Component	Partial Derivative	Gradient Value (nT/m)
B_x	$\partial/\partial x$	0.048
	$\partial/\partial y$	0.040
	$\partial/\partial z$	0.072
B_y	$\partial/\partial x$	0.041
	$\partial/\partial y$	0.061
	$\partial/\partial z$	0.041
B_z	$\partial/\partial x$	0.078
	$\partial/\partial y$	0.042
	$\partial/\partial z$	0.070

Figure 3.7: Table of gradients extracted from the optimized B_0 COMSOL model.

uniformity. The shielding performance of the MSR combined with the non-zero tolerances of the physical B_0 coil will likely result in gradients larger than the modeled gradients. In the remainder of the chapter, gradients less than 0.1 nT in magnitude will be specified as “< 0.1 nT/m”.

3.3 Tolerances

It has been shown above that the B_0 coil design theoretically provides a magnetic field consistent with the gradient specification $\langle |\partial B_z / \partial z| \rangle < 0.3$ nT/m. The physical coil and surrounding magnetic materials will contain imperfections and inaccuracies which result in field gradients with larger magnitude than the modeled field. The examples of possible discrepancies between the modeled coil and the physical coil discussed in this subsection are: the ratio between the two applied currents, the positioning of the coil sections relative to the MSR, and the magnetic properties of the MuMetal shielding layers. A successful coil design will meet the specified gradient requirement despite expected imperfections in the range of the estimated tolerances. In other words, the optimized coil design should be located in a sufficiently flat region of the parameter space such that altering any coil parameters by the corresponding achievable tolerances will not increase the magnetic field gradients above the gradient specification.

Applied Current Ratio

The optimal current ratio in the modeled B_0 system is $I_{out}/I_{in} = 1.820$ (see Table 3.1). Note that only 4 significant figures are included. The motivation for this is two-fold: 1) Any changes in the magnetic material surrounding the coil will cause the optimal current ratio to shift. Since the modeling of the MSR surrounding the coil is imperfect, the optimal current ratio for the physical apparatus will be determined in situ via a feedback from magnetic field measurements. More details on the expected range of such a shift in current ratio will be discussed later in this section. 2) The power supplies employed to supply the currents will have a noise profile and non-zero current magnitude drift over time. If the B_0 field is more sensitive to these perturbations in current values, the optimal current ratio would need to be precise to many significant digits, making the supplies more difficult and/or more expensive to fabricate or acquire.

To address these concerns, the optimal coil parameters should be chosen such that the gradient specification is satisfied for a range of current ratios. Using the COMSOL model, the current ratio can be swept, holding all other parameters constant, to investigate the effect of perturbing the current ratio on the storage cell gradients. The results of the sweep are summarized by the plot in Fig 3.8. The B_0 field profile in the upper UCN storage cell corresponding to various current ratios is shown in Fig 3.9. Given the relatively large range over which the gradient specification is still satisfied, the power supply requirements will not be constrained by gradient concerns, i.e. relative drifts of the currents provided by each supply. A more stringent requirement

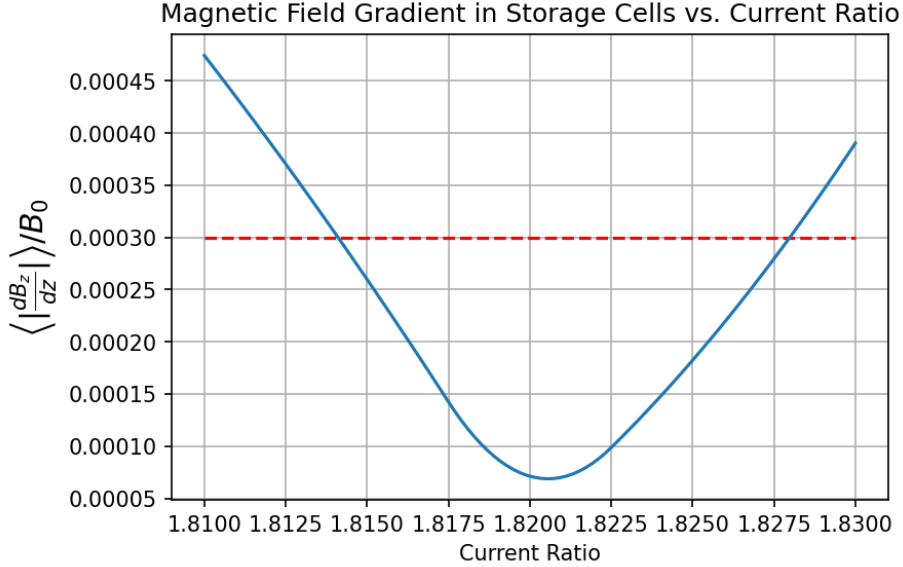


Figure 3.8: Plot of $\langle |\partial B_z / \partial z| \rangle$ normalized to the central value of \vec{B}_0 for different current ratios. The dashed red line represents the upper limit of the gradient specification $\langle |\partial B_z / \partial z| \rangle < 0.3$ nT/m. The gradient produced by the modeled B_0 coil design satisfies the gradient specification for the range of current ratios $1.814 \leq I_{out}/I_{in} \leq 1.828$

of the power supply current will come from the temporal stability required for the neutron EDM measurement.

The B_0 coil could be driven with up to 4 independent currents, assuming that the coil is still made to be symmetric about the xy -plane. The B_0 design presented here also has the following constraints on current:

$$\begin{aligned} I_{S1} &= I_{S2} \\ I_{S3} &= I_{S4} \end{aligned} \tag{3.1}$$

This reduces the number of independent currents to two. The magnetic field uniformity in the fiducial volume can be increased if the constraints in Eq. 3.1 are not applied. However, if $I_{S1} \neq I_{S2} \neq I_{S3} \neq I_{S4}$, four current supplies are required to generate the B_0 field. Having four independent current supplies introduces complexity in the magnetic field control and data analysis because the supplies will all drift relative to one another. There is also effort and cost associated with implementing and monitoring two additional power supplies. Given that the MSR performance specification is based on the UCN storage cell gradient specification, improving the B_0 field uniformity past 0.1 nT/m is unlikely to be realized in the physical apparatus. Since the B_0 model indicates that the gradient specification can be achieved using two current supplies without sacrificing the magnetic field uniformity in the fiducial volume, the two-current design is preferable compared to a design with four currents.

In the modeling, the optimized values were not currents—they were current densities. The terms current and current density have been used interchangeably in this chapter under the assumption that the current paths in the inner and outer coil sec-

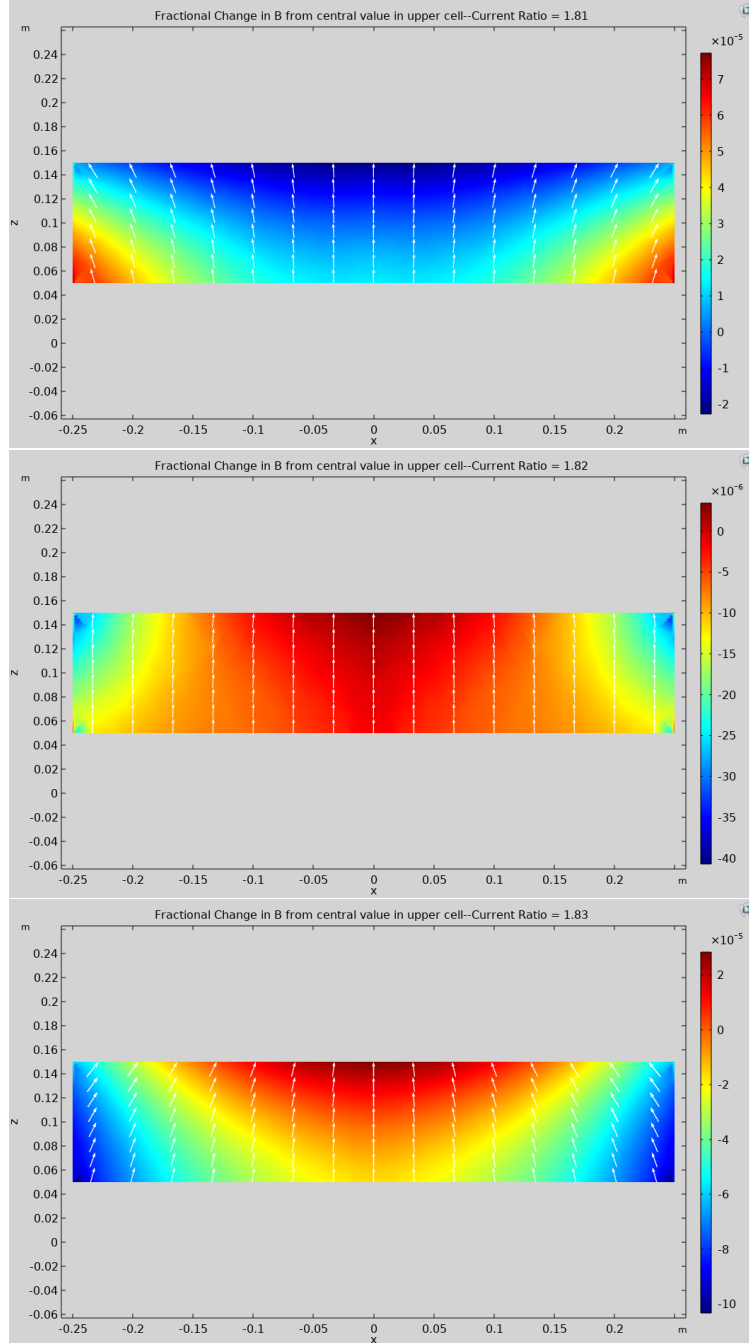


Figure 3.9: Plots showing the \vec{B} field profile in a $y = 0$ cross section of the upper UCN storage cells for current ratios 1.81, 1.82, and 1.83 (from TOP to BOTTOM). Since the model is symmetric across $z = 0$, one can infer the field behavior in the lower cell. The color map shows fractional change from the central $|\vec{B}|$ value. The vector plots show \vec{B} projected onto the $y = 0$ plane. The z component of the vectors has been scaled by 10^{-4} to visualize the divergence/convergence of the fields. The optimal current ratio 1.82 is tuned such that there is very little deviation in the B_x component of the vector plot.

tions have equivalent, constant cross section. This was implemented in the B_0 final coil design presented here by setting all PCB trace widths to 3 mm and using 2 oz copper thickness. It is interesting to consider altering trace density, as opposed to current value, to produce different current densities. For example, the optimal B_0 coil design presented in this chapter could have used the same 3 mm trace pitch on the inner coil PCB panels and a 1.65 mm trace pitch on the outer coil PCB panels. Then exciting the inner and outer coils with the same current would produce the desired current ratio of 1.82 from Table 3.1. This allows B_0 coil sections to be connected in series and operated with a single current supply. Assuming that the behavior of the MSR is linear with respect to the B_0 current—a valid assumption if the MuMetal is far from magnetic saturation—drifts in the single current supply would only alter the magnetic field magnitude, and the fractional gradient would remain constant. The sacrifice associated with the single supply design is that the current ratio cannot be tuned in situ. Since the modeling may not precisely capture the magnetic properties of the MSR, which are not necessarily constant over time, it was decided that the flexibility in the two-current design outweighed the advantages of the single-current option. The magnetic properties of the MSR related to the B_0 coil tolerances are discussed in detail later in this section.

Physical Offsets

When the B_0 coil is assembled, the positions of each coil section will have some error. The magnitude of this error depends on the method used to measure the various positions. Using FEA modeling, the precision required for positioning the coil sections can be estimated. The estimates inform the process and mechanisms used in the coil assembly process. Using the method of images as in [58], the system of the B_0 coil and MSR can be visualized as the B_0 coil superimposed with two reflected coils—one from the top face of the MSR and one from the bottom face. The position of the reflected coils depend on the distance r from the MuMetal surfaces. In this picture, if the B_0 coil is displaced by D in the positive z direction, the reflected coil from the top MuMetal surface will be displaced by $-D$, and the reflected coil from the bottom MuMetal surface will also be displaced by $-D$. Relative to the fiducial volume, the distance to the upper reflected coil has decreased while the distance to the lower reflected coil has increased, creating an asymmetry in the effective current distribution. The worst-case scenario is a vertical offset of the entire B_0 structure, i.e. offsetting the z positions of each coil section in the same direction, because this type of offset maximizes the asymmetry of the effective current distribution. Figures 3.10 and 3.11 show the effect of a vertical offset on the magnetic field gradient. An offset > 0.24 mm will result in a magnetic field gradient larger than the specified $\langle |\partial B_z / \partial z| \rangle < 0.3$ nT/m. Considering the scale of the coil is ~ 2 m, sub mm precision is difficult to achieve. To accomplish such precise positioning, a point cloud will be generated from the initial coil assembly using a laser measurement system. The point cloud can be used to prescribe displacements of the corner connectors that determine the coil section positions, and the adjustments can be applied precisely using the z position adjustment mechanism described in section 3.4. Since the B_0 field is very

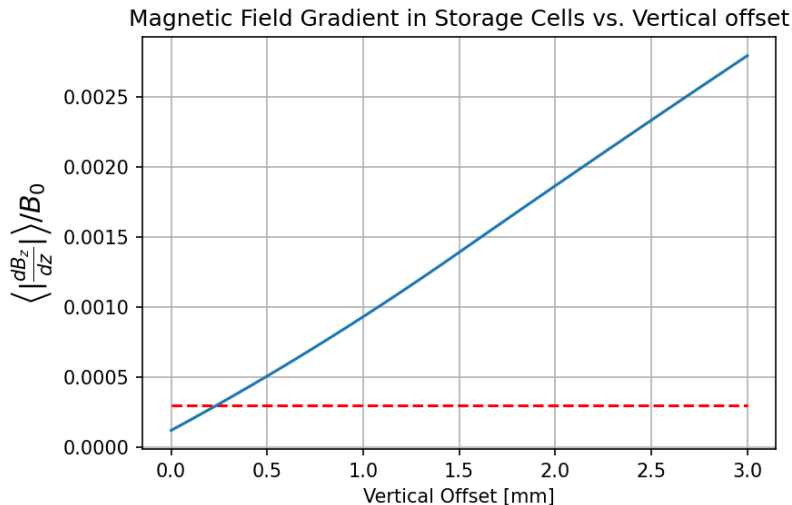


Figure 3.10: Plot of volume averaged magnitude of fractional B_z vertical gradient versus vertical offset of the B_0 coil. Note that the vertical offset on the x -axis is applied to all the B_0 coil sections. The dashed red line represents the upper limit of the gradient specification. The gradient specification is satisfied for offsets up to 0.25 mm.

sensitive to a globally applied vertical offset, it is important that the technique chosen to do the initial coil assembly is not subject to a systematic effect that produces such an offset.

Suppose the positioning constraint is relaxed to allow for up to 1 mm vertical offsets where the offset of each coil section is randomly distributed between -1 mm and 1 mm. This level of precision is achievable even without implementing the laser measurement system. Three example assortments of offsets are shown in Table 3.2 alongside the corresponding value of $\langle |\partial B_z / \partial z| \rangle$. The effect of these offsets is much smaller than even a 0.5 mm offset as observed in Figure 3.10. For some arrangements of offsets, the gradients may be larger than the specified value and would require correction, i.e. physical adjustment of coil position, field tuning by altering the current ratio, or the application of fields from shim coils. Table 3.2 supports the decision to relax the physical offset precision to < 1 mm offset, as long as any correlated systematic shifts are mitigated. Physical offsets in the x and y directions were modeled as well. These horizontal offsets have negligible effect on the gradients in the UCN storage cell volumes. Returning to the method of images, the reflected coils from the side walls of the MSR will be seen as adjacent solenoids. The field outside of the radius of the solenoid and close to its mid-plane will be much smaller than the field at its center [59]. Therefore, the contribution of each of these reflected solenoids from the side walls is expected to be negligible.

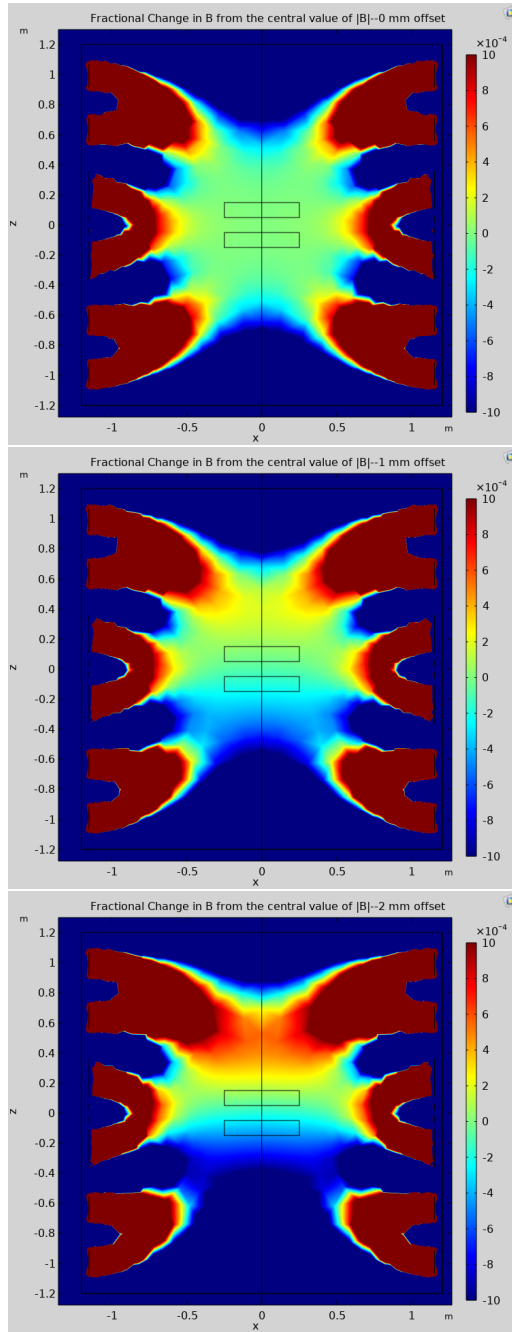


Figure 3.11: Color maps showing effect of vertical offsets on the B_0 field profile. The offset listed in each plot title is applied to the z position of the B_0 coil sections. Note that larger offsets result in larger field variation across the cell volumes, represented by the small rectangles at the center of each plot.

Table 3.2: Table of offsets for each B_0 coil section in mm and the modeled gradient from a design with those offsets applied in nT/m. The nominal design case does not have any position offsets. The offsets are selected at random from a uniform distribution $[-1, 1]$ mm and rounded to the nearest 0.1 mm. Note that Ex. 1 does not meet the gradient specification $\langle |\partial B_z / \partial z| \rangle < 0.3$ nT/m.

Coil Section	Nominal design	Ex. 1	Ex. 2	Ex. 3
S4 _l	0	0.5	0.4	0.2
S3 _l	0	0.0	0.3	0.3
S2 _l	0	0.9	0.0	0.0
S1 _l	0	-0.3	0.2	0.8
S1 _u	0	-0.9	-0.2	-0.5
S2 _u	0	1.0	0.3	-0.3
S3 _u	0	-0.4	1.0	0.3
S4 _u	0	0.6	-0.8	-0.3
$\langle \partial B_z / \partial z \rangle$	< 0.1	0.56	0.20	< 0.1

Mumetal Magnetic Properties

Mumetal is well-known for having inconsistent magnetic properties, specifically the magnetic permeability. Two samples from the same batch may not show similar permeability depending on the annealing and handling of the material, as was seen in [60]. By the same token, a sample of MuMetal may have its magnetic properties change over time if it is, for example, under mechanical stress. During transportation and assembly of the MSR, the constituent MuMetal sheets were subjected to some amount of stress. Re-annealing the material would return it to a high permeability state [61], but it is not feasible to re-anneal the sheets in situ. Even if one could complete such a measurement, the sheets may be subjected to additional stress from the MSR settling or thermal expansion/contraction, altering the magnetic properties over a long time scale. So, the magnetic properties of the MSR material is not known to high precision. The primary purpose of the MSR is to shield the ambient magnetic field, for which the performance can be evaluated without knowing the permeability of the material. However, the permeability is important to consider for calculating the field provided by the coil and MSR magnetic system.

The optimized model uses a nominal relative permeability $\mu_r = 3 \times 10^4$ to represent the MuMetal shielding. If the physical MuMetal sheets have a different permeability, the coupling between the coil and MSR will not be modeled accurately, and the optimal location in the coil parameter space will shift from the modeled optimum. It is not feasible to design a coil for a particular magnetic environment because, as discussed above, the magnetic properties of the MSR can evolve over time. Instead, the coil design should meet the gradient specification for the full range of possible permeability. For a single coil design, the geometric parameters are fixed with the exception of gap sizes, which may not be fully constrained but are difficult to manipulate. On the other hand, the current ratio can be freely varied to maximize

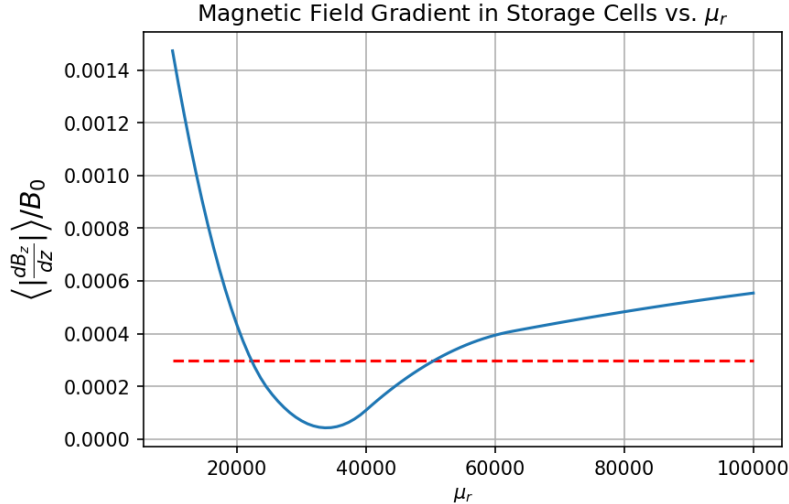


Figure 3.12: Plot of volume averaged magnitude of fractional B_z vertical gradient versus relative permeability μ_r of the MSR layers. The gradient specification $\langle |\partial B_z / \partial z| \rangle < 0.3$ nT/m—the upper limit of which is shown by the dashed red line—is satisfied for the range of permeability $21800 < \mu_r < 50900$. This analysis was performed without adjustment of current ratio from the nominal value $I_{out}/I_{in} = 1.82$.

field uniformity for the present magnetic system. It is important to validate that the optimal B_0 coil design can meet the gradient specification for the range of expected permeability, and, if the gradient becomes too large using the nominal current ratio for any permeability in this range, the required uniformity can be recovered by adjusting the current ratio to a new optimal value.

The effect of μ_r on the magnetic field gradient produced by the optimized B_0 design is shown in Figure 3.12. The range of permeability across which the gradient specification is satisfied is $21800 < \mu_r < 50900$. The permeability of the physical MuMetal sheets may fall outside of this range; however the current ratio that yields the highest field uniformity with $\mu_r = 30000$ will not necessarily yield the highest uniformity for a model with $\mu_r \neq 30000$. If the current ratio is allowed to shift for different values of μ_r , the gradient specification criterion can be recovered. As an example, one can evaluate the case where $\mu_r = 75000$. The gradient produced using the nominal current ratio $I_{out}/I_{in} = 1.82$ is $\langle |\partial B_z / \partial z| \rangle = 0.46$ nT/m. Adjusting the current ratio to $I_{out}/I_{in} = 1.81$ reduces the gradient magnitude to $\langle |\partial B_z / \partial z| \rangle < 0.1$ nT/m, successfully recovering the gradient specification of $\langle |\partial B_z / \partial z| \rangle < 0.3$ nT/m. Thus, the design is able to meet the experiment’s magnetic field specifications for a range of MSR magnetic properties, providing the flexibility needed to maintain the required uniformity throughout the operation of the experiment.

Although the B_0 coil modeling provides confidence that the applied magnetic field will contain gradients within the experimental specification, the possibility of large gradients present in the storage volume cannot be ruled out. The source of field gradients could be ambient magnetic field that is not adequately shielded, remnant magnetization in the MSR MuMetal, or the B_0 field itself. Anticipating the

possibility—even likelihood—of magnetic field gradients above the specified magnitude, a system of shim coils is being developed to generate general higher order field gradients. The design of the shim coil system is based on the projection of field expansion terms onto a cubic surface within the MSR interior. The basis functions in rectangular coordinates are calculated in [62].

3.4 Novel Features and Prototyping

The materials and design for the B_0 coil components were chosen to meet material property specification, provide the necessary positioning precision, and mitigate challenges associated with the operation of the experiment. The requirement on material properties is that the materials must be nonmagnetic, determined by the magnetic contamination scanning procedure described in Section 2.2. The precision to which each coil section must be positioned is < 1 mm which comes from the analysis of FEA modeling in the previous section. The experimental challenges addressed by the coil design will be introduced during the detailed discussion of the corresponding coil component in this section.

The B_0 coil sections each contain eight PCB panels—the PCB panels representing the flat coil faces. The panels contain multiple parallel traces which provide the desired current path across the long axis of the coil face. Corner connectors are used to physically support the PCBs and create electrical continuity across the 45° angle at each “vertex” of the octagonal shape. The corner connectors consist of a rubber-backed flexible PCB within a machined aluminum housing. The flexible PCBs each have parallel traces matching the pattern of the two PCB panels with which they are connecting. The PCB panels and flexible PCBs have copper pads at both ends of each trace. When the exposed copper of the PCB panel contacts the exposed copper of the flexible PCB, electrical continuity across the corner is achieved. The connection between the flexible PCB and PCB panels is achieved via a compression supplied by an aluminum sheet. The rubber backing is important for equalizing the compression force across the panel width, maximizing the opportunity for reliable electrical continuity. The coil sections are attached to the B_0 frame at the corner connector locations. Each corner mount has a built-in adjustment mechanism that allows for fine adjustments of the z position of the corner connector. The frame is attached directly to exposed MSR support locations.

The assembly process of the coil begins with the frame. The B_0 frame, shown in Figure 3.13 is a series of extruded, T-slotted aluminum connected to the MSR. Since the B_0 coil is magnetically coupled to the MSR, it makes sense to physically couple the two. Low-profile extrusion was chosen to maximize the volume available for the coil and other elements of the LANL-nEDM apparatus. Breaks in the frame verticals accommodate the neutron guide entry into the coil interior. The frame cannot be mounted on the door of the MSR, which is the west wall, because the system must be assembled when the MSR is open, i.e. when the west wall is not in place. Thus, the west side of the frame is connected to the MSR via mount points on the ceiling.

After the frame is in place, the corner connector housings are mounted. The corner connector mounts are 3D-printed parts that fully constrain the corner con-

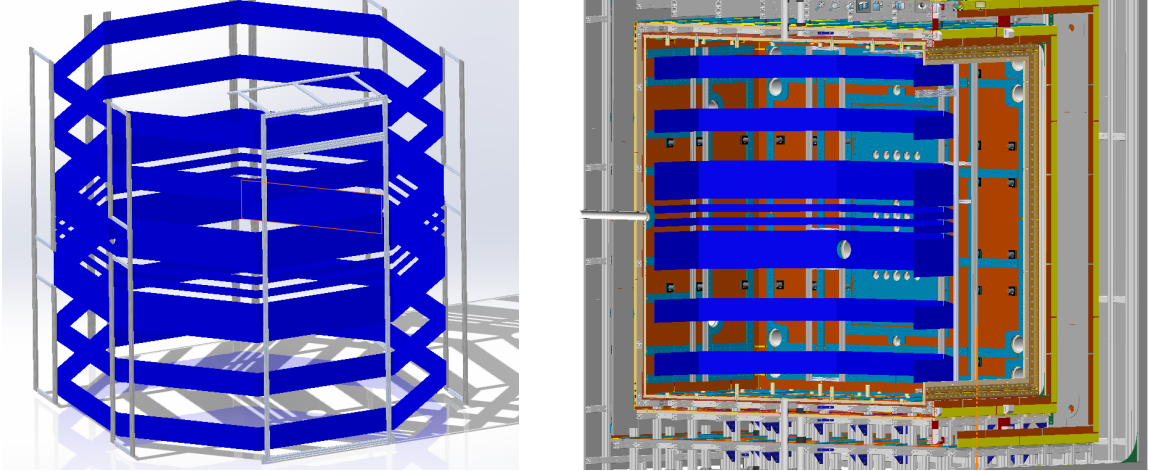


Figure 3.13: CAD renderings of the B_0 coil frame and coil. The system is shown standalone (LEFT) and in the MSR (RIGHT).

nector position. Gauge blocks are used to position the mounts precisely in reference to the MSR ceiling mount points. The corner connector housings are then secured in the mounts. Since the ceiling mount points may not be coplanar with the top MuMetal face, the positioning achieved by the gauge blocks may not be accurate to the < 1 mm requirement found in tolerance modeling. To account for this possibility, the mounts include a fine adjustment mechanism in the form of a trapped nut and bolt. The weight of the upper part of the mount is supported by this bolt, meaning that the z position of the corner connector is fully determined by the position of the bolt. Since the trapped nut cannot move, rotating the bolt will displace the bolt, and consequently the corner connector, in the z direction. For a standard $1/4'' - 20$ bolt, assuming the resolution of manual adjustment is limited to one quarter turn, position adjustments of ~ 0.3 mm can be achieved, which should be adequate to meet the gradient specification based on Fig. 3.10 and Table 3.2. Finer adjustment is possible with the choice of a nut and bolt that have smaller pitch.

Finally, the PCB panels can be attached to the mounted housings. Note that the choice of PCB panels and the design of the corner connectors allow for the coil to be modular. The PCB panels exist independent from one another—aside from the consideration that a closed loop should be formed to produce electrical continuity. An example of why this should be considered advantageous is in the case of damage to the trace causing electrical discontinuity. This may result in the replacement of a single PCB panel. This simple solution is juxtaposed to damaging a cylindrical coil wound with magnet wire where damage to the wire could lead to replacement of the entire coil section.

Another advantage of the modular B_0 design is that it allows quick access to the interior of the coil for personnel. There are times during the operation of the experiment when work, often maintenance, needs to be completed on the apparatus within the B_0 coil. A portion of this experimental “down time” is spent disassembling and reassembling the coil. In the case of a wire-wound coil, the coil sections will likely need



Figure 3.14: Picture of the full-scale B_0 coil assembled in the MSR at LANL.

to be displaced or removed entirely, only to be repositioned when work is completed. For the modular design, access to the interior of the coil is achieved by removing the number of PCB panels corresponding to the space needed for the ongoing work, which may be as little as six. In the end, the PCB panels can be reattached to the corner connectors, which remain in their precise positions throughout the process. The reduction in time spent with the experiment down due to the modular design has a direct impact on the final statistical sensitivity attained.

The full-scale B_0 coil has been successfully fabricated and assembled in the LANL-nEDM apparatus (see Fig. 3.14).



Figure 3.15: Picture of the half-scale prototype B_0 coil.

Half-scale Prototype

A half-scale prototype B_0 coil was designed and fabricated to validate the full-scale design concept. The main goal of the half-scale coil was to test the corner connector housing, the corner mounting mechanism, and the electrical continuity provided by the compression at the corner connectors. In addition to testing these features, the half-scale prototype was placed into a small MSR at LANL to measure the magnetic field generated.

A standalone frame was designed to support the prototype B_0 coil. Extruded T-slotted aluminum and aluminum hardware were used to fabricate the frame—choosing nonmagnetic material allows for unperturbed measurement of magnetic field uniformity. The corner connectors and corner mounts were 3D printed using polylactic acid (PLA) filament. It was found that the mounts were difficult to position to the sub 1 mm precision required which motivated the development of the fine position adjustment mechanism described in the previous subsection. Additionally, the 3D printed corner connectors deformed when applying the compression force to the PCB panels, resulting in intermittent and/or unreliable connections between adjacent PCB panels. To solve this problem in the half-scale B_0 coil, aluminum sheets were added to each side of the corner connectors as rigid support pieces. It was determined that the full-scale B_0 corner connectors should be machined from aluminum to provide the rigidity needed for consistent electrical connection. The implementation of aluminum corner connectors and a precision mount alignment mechanism was proven successful in the full-scale B_0 coil.

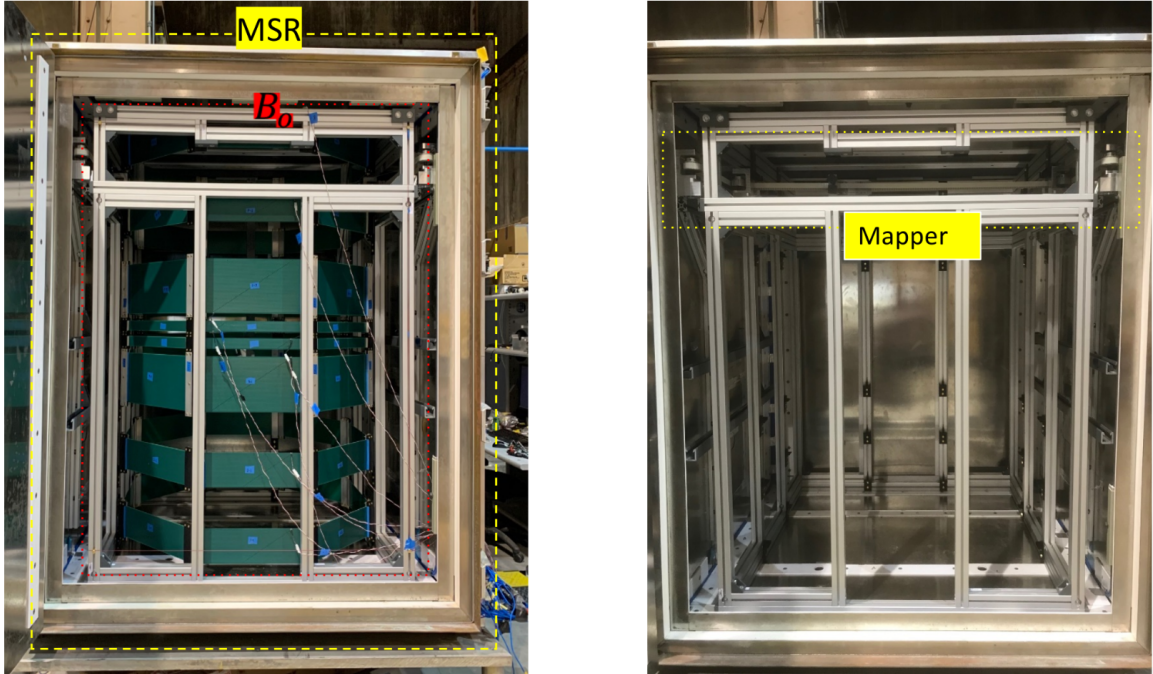


Figure 3.16: Pictures of the half-scale prototype coil in the small MSR at LANL [63].

The half-scale B_0 coil was designed to fit into a small MSR at LANL where the field uniformity would be measured. The MSR provides a low field environment to measure small gradients as well as the coupling between the B_0 prototype and magnetic shielding which is required to produce high uniformity. The half-scale coil and framed were designed to accommodate the H-frame mapper that exists in the small MSR at LANL. The H-frame mapper requires an unobstructed plane in which the mapper can be translated. This plane is located between the top two sections of the prototype coil. The field produced by the half-scale prototype inside the MSR was measured along the axis of the coil. An anti-Helmholtz shim coil was added to cancel the linear gradient along the axis of the coil. Given the mirror symmetry of the coil about the mid-plane, the coil should not produce a linear gradient along its axis. Some possible sources of a linear gradient along the coil axis are: remnant magnetization of the MSR after a degaussing procedure, a vertical position offset of the coil frame relative to the MSR, and positional offsets of individual coil sections. The existence of the strong gradients confirms the importance of precisely controlling all such sources of magnetic field gradient, especially linear gradients along the axis of the B_0 coil, in the full-scale implementation of the B_0 coil.

The magnetic field measured in the half-scale coil demonstrates the expected behavior of the B_0 design. A single fluxgate magnetometer was translated along the axis of the coil in order to generate the various sets of magnetic field measurements. Adjusting the current ratio between the inner and outer coil sections provides the ability to minimize the even order gradients (see the left plot in Fig. 3.18). At the optimal current ratio of 1.71, the shim current was increased to minimize the linear gradient (see the right plot in Fig. 3.18). Given the optimal current ratio of 1.71 with

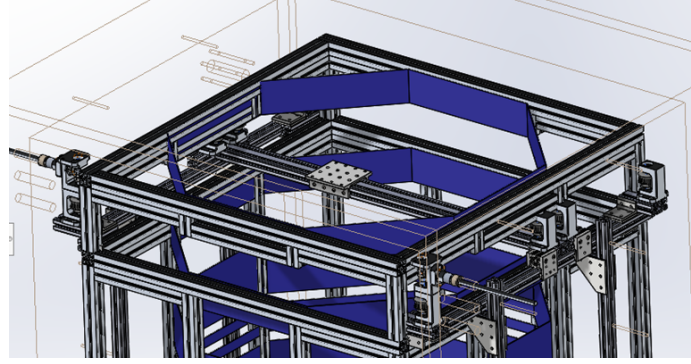


Figure 3.17: CAD rendering of the H-frame mapper and the half-scale B_0 . The mapper allows motion of the carriage (shown at the center of the image) along the rail spanning the coil width. This rail is translated perpendicular to its length via synchronous actuation of stepper motors and a timing belt-pulley system (not pictured).

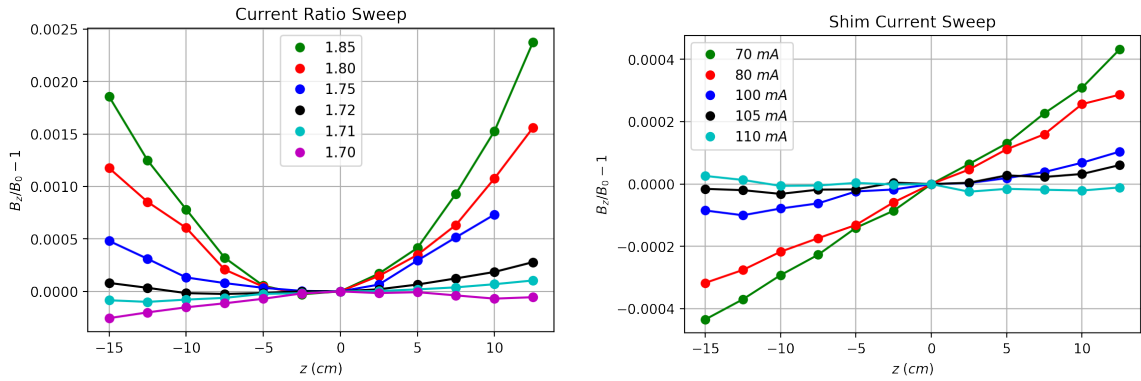


Figure 3.18: Plots of B_z from the half-scale B_0 prototype field along the axis of the coil. The magnitude of the magnetic field produced by the prototype coil is $|B_0| \approx 2.9 \mu\text{T}$. LEFT: Holding the shim current constant (100 mA), the B_0 outer to inner current ratio is swept to find the minimum second order gradient. RIGHT: At the optimal current ratio of 1.71, the shim current is swept to produce the highest uniformity—i.e. the smallest gradient. The optimal shim current is between 105 mA and 110 mA.

the nearly optimal shim coil current of 110 mA, the magnetic field gradient along the axis was:

$$\frac{1}{B_0} \frac{\partial B_z}{\partial z} < 1 \times 10^{-4} \text{ m}^{-1}$$

Chapter 4 Spin-Transport Coils

4.1 Spin-Transport Magnetic Field

The magnetic fields realized in the LANL-nEDM experiment will, of course, contain non-zero gradients. The systematic effect of non-zero gradients present in the UCN storage volume is discussed in the previous chapters. This chapter discusses the impact of magnetic field gradients, which must be considered in all regions accessible to neutrons, on the achievable statistical uncertainty. The UCNs propagate through the neutron guides between the polarizing magnet and storage cells, during the fill time period, and between the storage cells and detector location, during the dump period. In order to maximize the polarization product AP_{det} , thus maximizing the experiment's statistical reach (Eq. 2.24), the polarization should be preserved while the neutrons travel through the guide system. The adiabatic parameter κ relates the neutron polarization to the magnetic field gradients [51]:

$$\kappa = \frac{\omega_L}{\omega_{grad}} \quad (4.1)$$

where $\omega_L = \gamma_n |\vec{B}|$ is the Larmor precession angular frequency about a magnetic field \vec{B} and ω_{grad} is the angular frequency of the magnetic field due to the gradients seen by the UCN. If $\kappa \gg 1$, the field is said to meet the adiabatic condition, meaning the change in polarization due to the field gradients can be considered negligible. The physical interpretation is that the neutron spin will follow the magnetic field direction if it is rotating about the field much faster than the field is changing direction. Note that a static magnetic field with a spatial gradient will produce a non-zero ω_{grad} if the UCN is moving through the field, as shown in Eq. 4.2:

$$\begin{aligned} \omega_{grad} &= \frac{1}{|\vec{B}|} \frac{d\vec{B}}{dt} \\ &= \frac{1}{|\vec{B}|} \frac{d\vec{B}}{d\vec{r}} \frac{d\vec{r}}{dt} \\ &= \frac{\vec{v}_n}{|\vec{B}|} \frac{d\vec{B}_\perp}{d\vec{r}} \end{aligned} \quad (4.2)$$

where \vec{r} is the position of the neutron and $\vec{v}_n = d\vec{r}/dt$ is therefore the neutron velocity. Plugging this result into Eq. 4.1, we find:

$$\kappa = \frac{\gamma_n |\vec{B}|^2}{v_n \frac{d\vec{B}}{d\vec{r}}} \quad (4.3)$$

The velocity of the neutrons will be, at most, 5 m/s (see Section 4.3). The adiabatic condition $\kappa \gg 1$ is considered true when $\kappa \geq 100$ for this maximum magnitude neutron velocity, where 100 is arbitrarily chosen as a large number.

The LANL-nEDM experiment relies on the MSR to supply a low magnetic field environment in which the $1 \mu\text{T}$ B_0 field is the dominant magnetic field. Using this field magnitude in Eq. 4.3, the field will meet the adiabatic condition if the following is true:

$$\left| \frac{\partial \vec{B}}{\partial \vec{r}} \right| \leq 0.366 \mu\text{T/m}$$

Considering the stringent requirement for uniformity of the B_0 field, represented by the $\langle |\partial B_z / \partial z| \rangle < 0.3 \text{ nT/m}$, is three orders of magnitude smaller than the allowable gradient using $\kappa = 100$ at $|\vec{B}| = 1 \mu\text{T}$, it can be assumed that the apparent rotation of the magnetic field in the neutron rest frame provides negligible depolarization.

For the ambient magnetic field magnitude $\sim 20 \mu\text{T}$, the adiabatic condition is met with a gradient:

$$\left| \frac{\partial \vec{B}}{\partial \vec{r}} \right| \leq 146 \mu\text{T/m}$$

Given that the field magnitude is $20 \mu\text{T}$, the source of such a large gradient would necessarily be located in close proximity to the volume containing neutrons, i.e. magnetic contamination in or around the neutron guide. Since the materials of the system are well controlled for magnetism, it is expected that the neutron polarization will not decrease when the neutrons are in the $20 \mu\text{T}$ field.

The region of space between the ambient field and the B_0 field must have a transition from $20 \mu\text{T}$ to $1 \mu\text{T}$. The distance from the B_0 surface to the exterior of the MSR is 0.6 m , but the field taper occurs over a length of 0.75 m . The additional 15 cm external to the magnetic shielding assumes that the combination of the field cage and MSR will reduce the field magnitude near the exterior of the MSR such that the applied spin-transport field will dominate, effectively providing extra length to ramp the field magnitude. If the field taper were linear, the gradient across this region would be $25.3 \mu\text{T/m}$. The neutron spin-transport in the high field portion of the field taper would be adiabatic, but the region with $|\vec{B}| \approx 1 \mu\text{T}$ would introduce significant depolarization with $\kappa \approx 10^{-6}$. To prevent depolarization, the profile of the magnetic field in the transition region should be designed to optimize for adiabatic transport.

A discrete solution to Eq. 4.3 can be calculated numerically for any value of κ using the following recursive relation:

$$B(x_k) = \begin{cases} 1.1 \times 10^{-6} & \text{if } k = 0 \\ B(x_{k-1}) + (\delta h) \gamma_n |B(x_{k-1})|^2 (\kappa v_n)^{-1} & \text{if } k > 0 \end{cases} \quad (4.4)$$

where δh is the step size between points at which the recursive equation is evaluated, $x_k = k(\delta h)$, and $B(x_k)$ is the magnetic field magnitude at x_k . As $\delta h \rightarrow 0$ the discrete solution converges to the continuous solution. From the convergence plot shown in Fig. 4.1, a step size of $1 \mu\text{m}$ is sufficiently small to provide a precise solution. The field taper is designed starting at the low field end where it interfaces with the B_0 surface. The magnetic field magnitude near the B_0 coil surface is $1.1 \mu\text{T}$, which sets

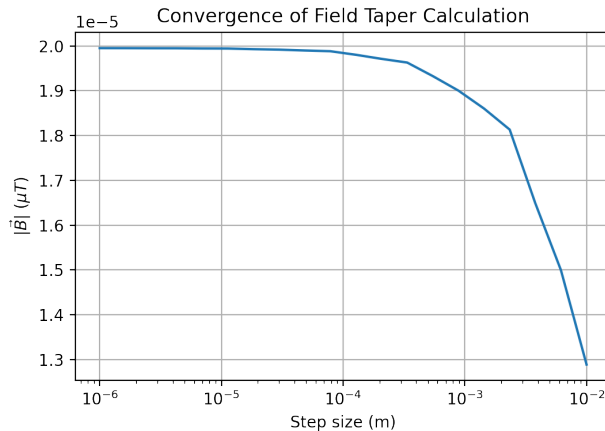


Figure 4.1: Plot of the maximum value of $|\vec{B}|$ in the field taper versus step size in the numerical integration. $|\vec{B}|$ is given by numerical integration of Eq. 4.3 for $\kappa = 32$.

the initial field magnitude at the end of the field taper. Since the value of κ controls the gradient magnitude and the starting magnitude is fixed, choosing a value for κ is equivalent to choosing the magnitude of the magnetic field at the other end of the field taper. Higher values of κ imply smaller gradients and therefore lower spin-transport field magnitude at the exterior of the MSR. For example, selecting $\kappa = 100$ results in a field taper from a $1.1 \mu\text{T}$ initial value to a final value of $1.58 \mu\text{T}$ —not sufficiently high field magnitude considering the ambient field magnitude is an order of magnitude larger.

To generate a field taper that achieves a final field magnitude of $\sim 20 \mu\text{T}$ in the allotted 0.75 m , the adiabatic condition $\kappa = 100$ cannot be maintained. The value of κ selected for the field taper design is $\kappa = 32$. This is the largest value of κ that provides the desired $\sim 20 \mu\text{T}$ field magnitude at the large field end of the spin-transport coils, giving a field ramp from $1.1 \mu\text{T}$ to $19.995 \mu\text{T}$. The magnitude of depolarization from the lack of adiabatic spin-transport is determined via spin-tracking simulations. Fig. 4.2 shows a plot of the field taper along the neutron guide. A NumPy least squares fitting routine is used to convert the discrete field taper data set into a 10^{th} degree polynomial function (see Table 4.1). The polynomial degree was determined based on the error, characterized by the residuals in Fig. 4.2, with the goal of achieving $\sim 1\%$ error to avoid local regions, especially in the low-field portion of the coil, with $\kappa < 32$. The coefficients of the polynomial terms are convenient for reproducing the field taper in COMSOL to produce the winding pattern, as discussed in the next section.

4.2 Spin-Transport Coil Design

After choosing the ideal field profile, one must determine the current distribution that will generate the desired magnetic field. This can be accomplished using the magnetic scalar potential [64]. In a region of space with no currents, such as the

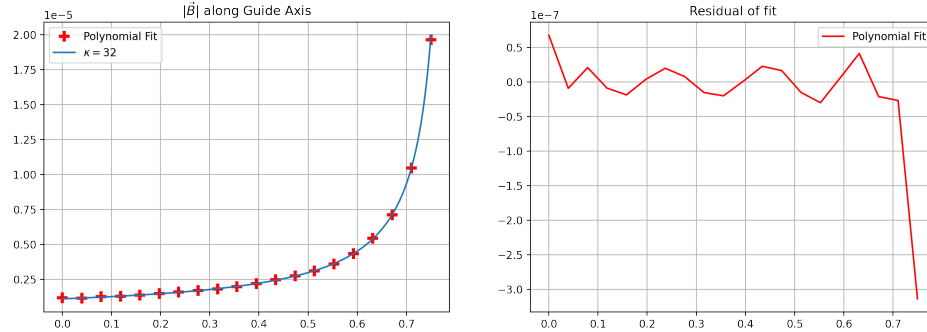


Figure 4.2: LEFT: Plot of the magnetic field magnitude given by the field taper between the ambient magnetic field and the B_0 magnetic field. The field taper gradient corresponds to an adiabatic parameter value $\kappa = 32$. A polynomial fit was performed to provide a functional form for the field taper. The value of the fit at discrete locations is plotted on top of the field taper. RIGHT: Plot of the residuals from the aforementioned polynomial fit.

Table 4.1: Coefficients of the polynomial fit for the field taper. The degree 10 polynomial provided residual on the order of 1% (see Fig. 4.2). Important to note that the range of this fit is $x = [-0.75, 0]$ where the $1.1 \mu\text{T}$ field magnitude occurs at $x = 0.75$ m.

Term	Coefficient
1	1.963671×10^{-5}
x	3.799942×10^{-4}
x^2	5.213411×10^{-3}
x^3	4.648211×10^{-2}
x^4	0.267355
x^5	1.004638
x^6	2.482305
x^7	3.989987
x^8	4.010262
x^9	2.286749
x^{10}	0.564321

neutron guide volume, Maxwell's equations require that:

$$\vec{\nabla} \times \vec{H} = 0 \quad (4.5)$$

$$\vec{\nabla} \cdot \vec{B} = 0 \quad (4.6)$$

where the fields \vec{B} and \vec{H} have a constitutive relationship assumed to be linear:

$$\vec{B} = \mu \vec{H}$$

Eq. 4.5 implies

$$\vec{H}(\vec{r}) = -\vec{\nabla} \Phi_m(\vec{r}) \quad (4.7)$$

where Φ_m is the magnetic scalar potential. Note that Φ_m must be a solution to the Laplace equation:

$$\begin{aligned} \vec{\nabla} \cdot \vec{B} &= \vec{\nabla} \cdot (\mu \vec{H}) \\ &= \vec{\nabla} \cdot (-\mu \vec{\nabla} \Phi_m) \\ &= -\nabla^2 \Phi_m \\ \vec{\nabla} \cdot \vec{B} &= -\nabla^2 \Phi_m = 0 \end{aligned} \quad (4.8)$$

The magnetic scalar potential Φ_m on the coil surface represents the current paths that produce the desired magnetic field $\vec{H} = -\vec{\nabla} \Phi_m$ within the enclosed region. Wires are used in the physical coils as current paths which means the continuous potential must be discretized to a finite number of contours. The current applied to each contour is given by the potential width of the continuous band that the contour represents. Typically, isocontours are chosen when discretizing the potential since each isocontour is equally spaced. The potential width of every band represented by an isocontour band is the same, given by the difference between the potential of two adjacent isocontours, meaning every isocontour requires the same current [65]. Since all of the wires should be carrying the same current, the wires can be connected in series, and the coil can be powered by a single current supply.

Coil Geometry

The coil geometry must be chosen to apply the magnetic scalar potential design technique. The spin-transport coils are a system of four coaxial cylindrical shells. The design is a modified double $\cos \theta$ coil. The coils are designed to be self-shielding, hence the need for two winding layers as opposed to a traditional cylindrical coil form. The modification from the traditional $\cos \theta$ design is the variable field magnitude along the axis of the coil. The coils have matching radii and various lengths shown in Table 4.2 and Fig. 4.3. Four sets of spin-transport coils will be implemented in the experiment—one set for each of the penetrations corresponding to the neutron guide position. The four sets will be referred to using the labels Set 1, 2, 3, and 4. In each set, the 4 individual coils will be termed Coils A, B, C, and D, where A is the innermost coil that interfaces with the B_0 coil, and D is the outermost coil.

Table 4.2: Dimensions of the four spin transport coils. All four coils have the same inner and outer radii: $R_{inner} = 0.0533$ m and $R_{outer} = 0.0661$ m. See Fig. 4.3 for a visualization of the coil geometry. The relative current values are normalized to the current in coil D. The absolute current values will be tuned to give optimal polarization transport using measurements of polarized UCN on the LANL UCN beamline.

Coil	Length (m)	Number of Wires	Relative Current
A	0.10	202	0.1196
B	0.15	182	0.1474
C	0.25	144	0.2572
D	0.25	166	1.0

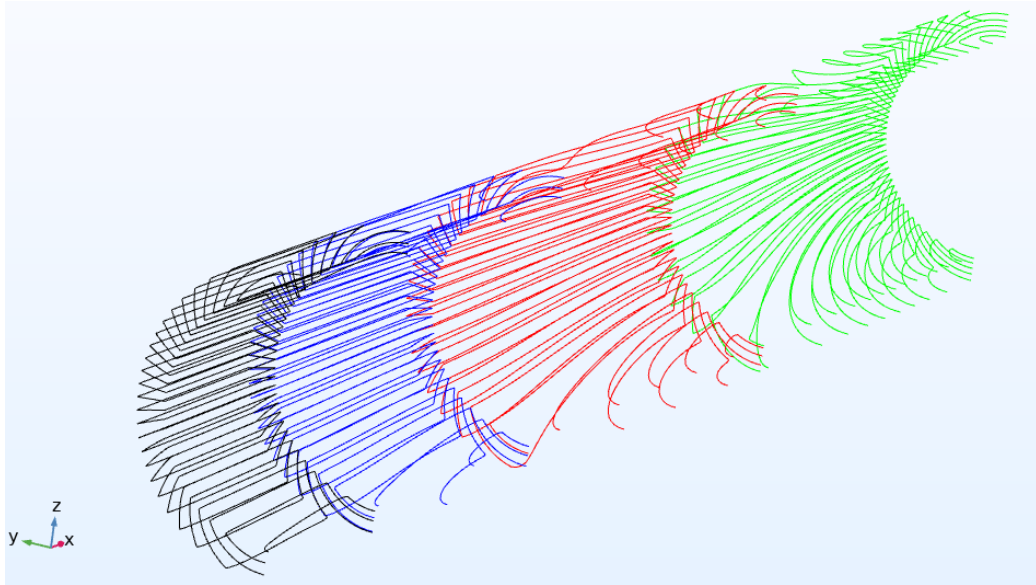


Figure 4.3: Image of spin-transport coil winding pattern. The coils are as follows: A (black), B(blue), C (red), D (green). The winding pattern is symmetric across the symmetry plane used to divide the cylindrical shell in half. The number of wires shown for each coil is a subset of the total number of wires used since the wire density becomes too high to distinguish detail.

The coil geometry is driven by the engineering constraints in the spin-transport region, consisting of the neutron guide with radius $R_{guide} = 1.5$ inches centered in the MSR copper branch tubes with radius $R_{tube} = 3$ inches passing through the MSR MuMetal penetrations. The design choice of cylindrical symmetry of the coil system is motivated by the cylindrical symmetry of the neutron guide and MSR penetrations. The copper branch tubes are constraining the outer radius of the coil geometry, so the outer radius of the coil system is $R_{outer} = 2.6$ inches, leaving space around the branch tube for centering relative to the guide and tolerance. The approximation that the discrete winding pattern represents the magnetic scalar potential isocontours breaks down at points where the distance to a wire is small relative to the spacing between wires. The perturbation from discrete wires falls off exponentially with length scale $D/(2\pi)$ as one moves away from the current carrying coil surface, where D is the distance between neighboring wires [64]. It should be noted that the wire density is not constant across the coil surface, and locations with lower wire density will reproduce the desired field profile less accurately [66]. To minimize this error, the wires should be positioned maximally far from the neutron guide, i.e. the inner radius should be made as large as possible. The current needed to generate the desired field depends on the thickness of the cylindrical shell, with thinner cylindrical shells requiring larger current excitation to produce the desired magnetic field magnitude in the neutron guide. The considerations related to higher current requirements are resistive losses in the wire and larger error from potential discretization and imperfect wire placement. The inner radius of the spin-transport coil system is chosen to be $R_{inner} = 2.1$ inches, resulting in a cylindrical shell thickness of 0.5 inches.

As stated above, the spin-transport coil system is comprised of four coils. In general, the use of multiple shorter coils in place of a single coil is not preferred. At the interface of each pair of the spin-transport coils, there will be finite space between the coil surfaces. The non-zero space between the coils will lead to field distortions compared to the target magnetic field profile. An example of this phenomenon is shown in Fig. 4.4. The single coil design does not introduce the interface related magnetic field distortions because the coil surface is continuous across the entire spin-transport system length. Consider the potential near the extreme ends of the single coil design. Near the B_0 interface, the field provided by the spin-transport coil is $\sim 1 \mu\text{T}$. At the opposite end of the coil, the field generated is on the order of $20 \mu\text{T}$. In order to produce a larger magnitude field, the magnetic scalar potential must have a larger magnitude gradient, which can be seen directly from $\vec{H} = -\vec{\nabla}\Phi_m$. As discussed above, the magnetic scalar potential coil design method requires that isocontours of the magnetic scalar potential be selected to represent the wire winding pattern with the current in each wire determined by the potential difference between isocontours. The density of isocontours at any point along the length of the single coil design is proportional to the field magnitude, regardless of the choice of isocontour potential width. Thus, the winding at the B_0 end of the coil will have wire spacing approximately ten times the wire spacing at the opposite end. Given the minimum distance between the wire surface and the neutron guide is 15.2 mm, the wire spacing in the $\sim 1 \mu\text{T}$ should be $D < 7.6$ mm for error on the order of $\exp(-4\pi) = 3 \times 10^{-6}$, resulting in at least ~ 45 wires. The wire density at the $\sim 20 \mu\text{T}$ region would then

Contours of $|B|$ (T) for a Cross Section of the Spin-Transport Coils

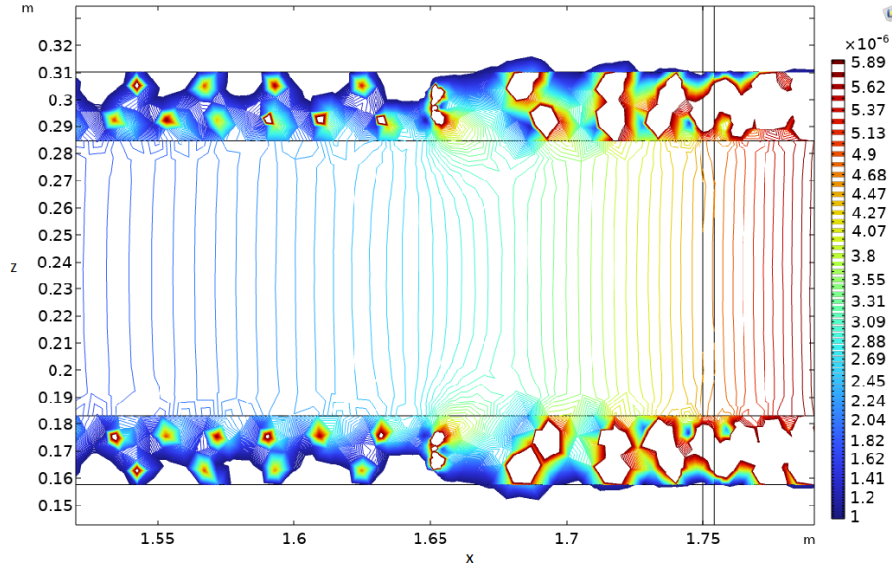


Figure 4.4: Contour plot of the magnetic field magnitude in the interior volume of two adjacent coils of the transport system, namely coil B and coil C. The color scale is logarithmic. The contours are nearly vertical, signifying that the magnitude of the field at a given x position is approximately constant, which is consistent with the design objective. The interface between coil B and coil C is located at $x = 1.65$ m. The contours in this region show more noticeable curvature due to the perturbation introduced by the interface.

be 20 times larger, requiring a minimum of 900 wires which gives an average wire spacing $D_{avg} = 0.37$ mm. The wire spacing is too small to provide the individual grooves necessary for precise positioning of the fabricated coil. Selecting a feasible wire density for the $\sim 20 \mu\text{T}$ coil region would lead to wire spacing much larger than the 7.2 mm spacing in the $\sim 1 \mu\text{T}$ region of the coil where gradients from local field distortions have a greater impact on adiabaticity.

Separating the spin-transport coil system into four individually powered coils allows for different isocontour potential differences on each of the coil surfaces. The selection of isocontour, or equivalently number of wires, can be tuned for each coil such that the wire spacing requirement is satisfied with a manageable number of wires on each coil (see Table 4.2 for number of wires on each coil). Coil A in each spin-transport set will be excited with the same current, and therefore coils 1A, 2A, 3A, and 4A will be connected in series. The same is true for coils B, C, and D. Four current supplies are required to power the four sets of spin-transport coils.

COMSOL Implementation

The magnetic scalar potential method was implemented in COMSOL to numerically solve for the winding pattern on the surface of the coil system geometry. The “Magnetic Fields, No Currents” package allows the user to define \vec{B} flux through the coil

surface and solves for the magnetic scalar potential that produces the assigned flux conditions. The spin-transport coil geometry is represented by four coaxial cylindrical shells with the dimensions prescribed in Table 4.2. The spacing between these coils is set to 0.25 mm so that the winding pattern on the annular end caps of each coil is calculated. The case where the coil spacing is zero would represent the single coil solution, which is not optimal for the reason described in the previous subsection. In the physical implementation, the coil spacing is limited by the diameter of the wire used to wind the coils—the fabricated spin-transport coils use 24 gauge magnet wire, resulting in ~ 0.5 mm of space between the coils. An additional double $\cos \theta$ coil is added at the “ B_0 end” of the spin-transport system with flux $B_z = 1 \mu\text{T}$ through the inner surface and zero flux through the outer surface. The magnetic field produced by the additional coil produces a magnetic field representative of B_0 coil near the spin-transport interface.

It is important to solve for the magnetic scalar potential in all domains separated by the coil surfaces. In the spin-transport model, the interior of each cylindrical shell is a domain in which the potential is solved. This gives us potential U_1 . Due to the open end caps, the remaining volume is a single domain in which the magnetic scalar potential can be calculated. The same flux conditions are applied to the coil surfaces, taking into account that the surface normal vectors have reversed sign for the new domain (normal vectors are defined as pointing into the volume being solved). The magnetic scalar potential in the exterior volume is defined as U_2 . Plotting the sum of these two vector potentials $U = U_1 \pm U_2$ on the coil surfaces gives the current path that produces the desired magnetic field.

Isocontours of the scalar potential U can be plotted on the surface of the spin-transport coil geometry using COMSOL (see Fig. 4.5). The plot of each coil is exported and sorted into individual wire files, which contain a list of (x, y, z) coordinates representing a three-dimensional polygon. These files are imported to the “Magnetic Fields” COMSOL module containing the B_0 coil and the MSR (see the top image in Fig. 4.6) to calculate the magnetic field generated by the full magnet system. Fig. 4.6 shows the cross section of the magnetic field in the xz plane. The modeled spin transport field can be compared to the target field profile, as shown in Fig. 4.7.

Self-Shielding Coil Motivation

The spin-transport coils are located within the penetrations in the MSR layers. The MuMetal material in close proximity to the coils presents two challenges: 1) the MuMetal magnetization can distort the magnetic field produced by the coils; 2) the magnetic field generated by the coil could affect the shielding performance by causing saturation near the MSR penetrations. The distortion of the magnetic field can be predicted given proper modeling of the MuMetal material properties. In fact, the MuMetal layers can be included in the FEA magnetic scalar potential model to generate a winding pattern which accounts for the effect of the MuMetal. An example wire winding pattern can be seen in Fig 4.8. Notice the kinks in the contours that occur at four locations along the axis of the cylinders, corresponding to the four

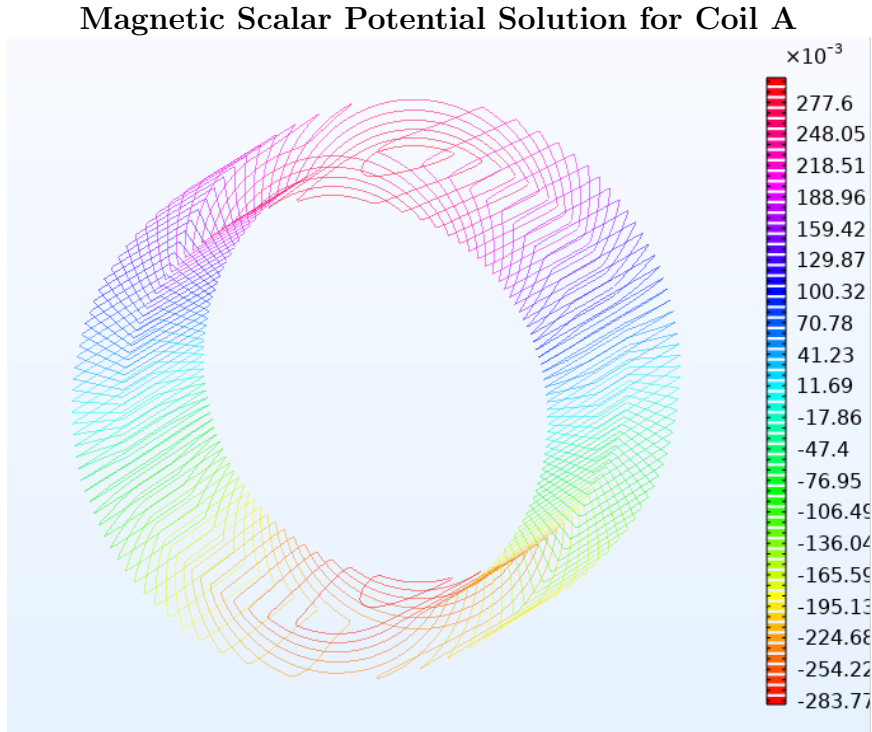
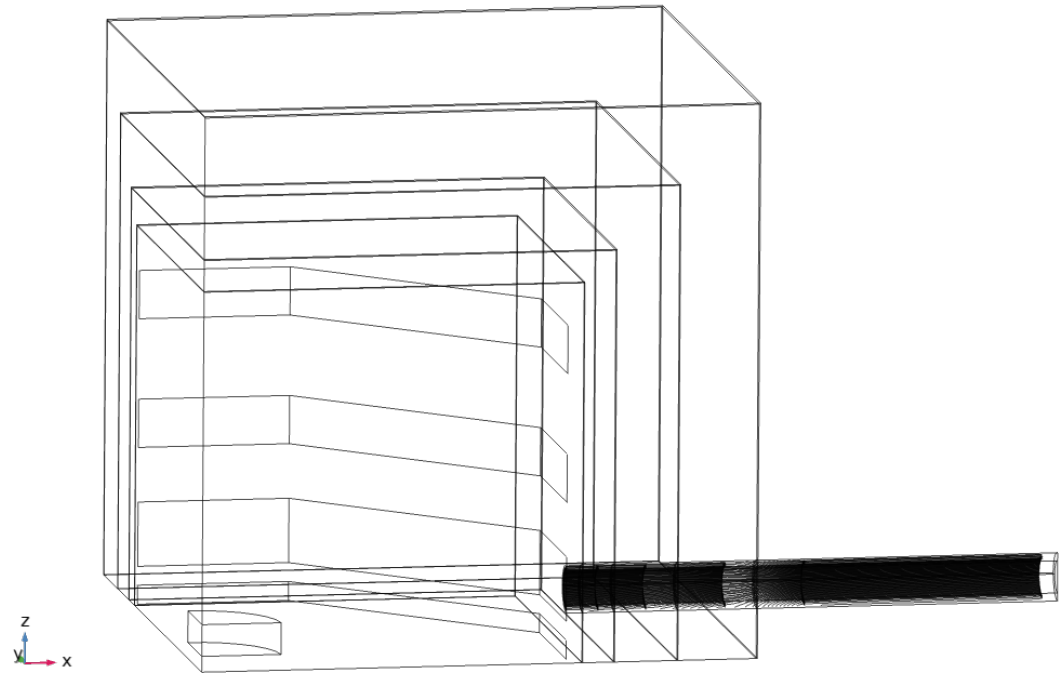


Figure 4.5: Winding pattern (isocontours) of Coil A in COMSOL. The color scale shows the value of the scalar potential.

MuMetal layers. While this is a valid solution to produce the desired field, it relies on accurate modeling of the MSR material properties which is not well-understood (see Ch. 3). Additionally, the resulting coil system is sensitive to changes in position relative to the shield layers which adds concern of position/fabrication tolerances and lack of flexibility to accommodate design changes. Accounting for the field distortion in the winding pattern will not address the possibility of the coil system reducing local shield performance (see Fig. 4.9).

Another solution for these potential concerns is to prevent the production of magnetic field at the location of the MuMetal layers. This can be accomplished using self-shielding coils, i.e. there is no magnetic flux through the outer surface of the coils. The magnetic field generated by a self-shielding coil will be determined by the current distribution and the material within the coil boundary, decoupling the coil from the external magnetic environment. The physical implementation of the coils will not be perfectly self-shielding, but the coil parameters (e.g. wire spacing and coil outer radius) can be chosen such that the field magnitude in the region with MuMetal material is negligible. The spin-transport coils are not strictly self-shielding coils since the coil end caps are not closed, creating leakage field. Where adjacent coils interface, the leakage field effect is mitigated (see Fig. 4.10). The interfaces of the four spin-transport coils are positioned at the midpoint between the various MSR layer locations to minimize the leakage field magnitude present at the MuMetal surfaces. The only open end cap without an interfacing coil is the outermost coil surface which is external to the MSR—the innermost coil interfaces with the B_0 coil



$|B|$ (T) generated by COMSOL

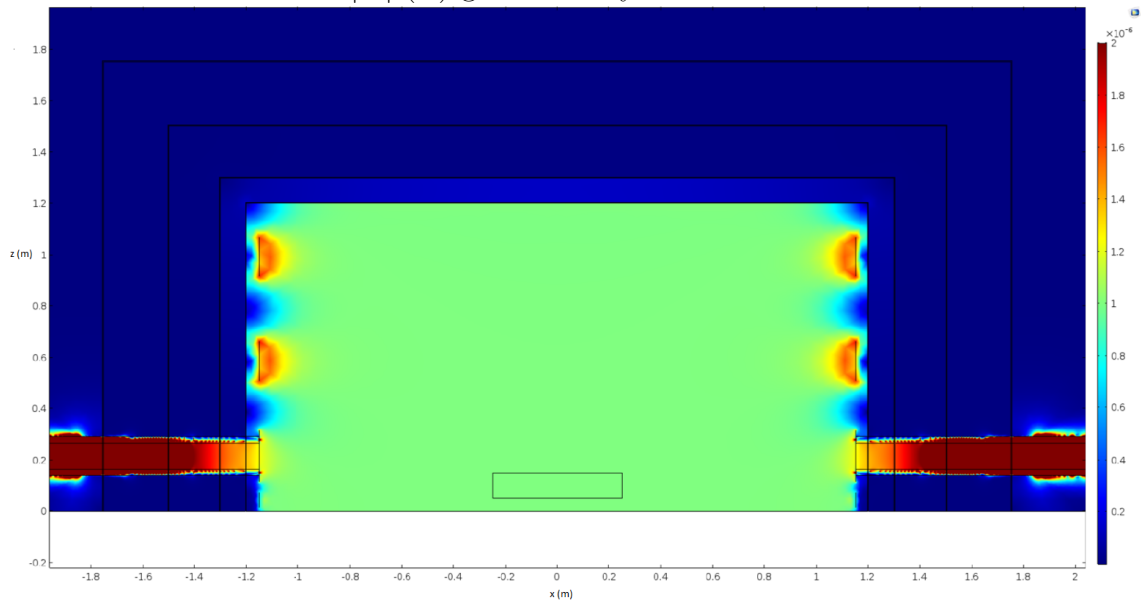


Figure 4.6: TOP: COMSOL combined B_0 and spin-transport coil geometry, rendered as a wire frame in one octant. The storage cell volume, B_0 surfaces, and the MSR layers are clearly visible. The high wire density in the spin-transport coils makes it difficult to distinguish winding pattern detail. BOTTOM: Magnetic field magnitude on the $y = 0$ plane generated using the COMSOL model shown above.

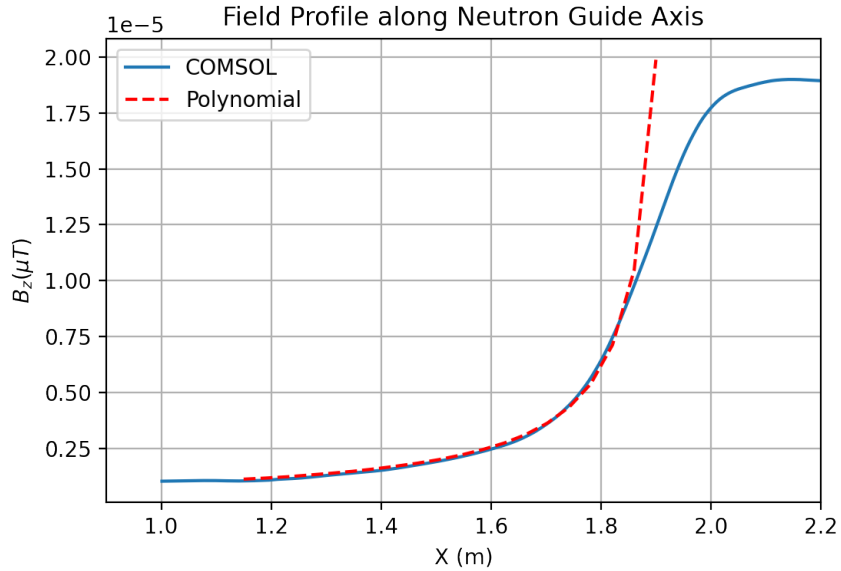


Figure 4.7: Plot comparing field profile generated by COMSOL versus the polynomial field taper. The spin transport coils are positioned between $x = 1.15$ m and $x = 1.90$ m. The designed field taper and COMSOL field are in good agreement up to $x = 1.85$ m. The spin-transport field profile deviates from the designed field taper due to the leakage field from the uncompensated, open end cap of coil D. Since the gradient of the modeled field is less than the polynomial gradient at this deviation, the value of the adiabatic parameter κ would be larger, but the length required to reach the ambient field magnitude is extended.

Figure 4.8: Show winding pattern of single layer spin-transport system where the effect of the MuMetal on the winding pattern can be seen.

to compensate for leakage field from the innermost surface of the spin-transport coil system.

4.3 Spin-Transport Efficiency Simulation

Simulation Setup

The spin-transport coil design is validated using PENTrack, a simulation tool for UCN interacting with geometries and electromagnetic fields [67]. Fusion 360 computer-aided-design (CAD) software was used to generate the neutron guide and storage cell mesh files imported by PENTrack. The neutron guide is a 3 inch inner diameter tube with a 90° bend connecting it to the top of the storage cell volume. The guide extends to $x = 4$ m, but it is capped with a guide stop at $x = 2.5$ m to prevent neutrons from escaping the enclosed volume, making the effective length of the neutron guide 2.5 m. The storage cell is a hollow cylinder with a height of 10 cm and a diameter of 50 cm.

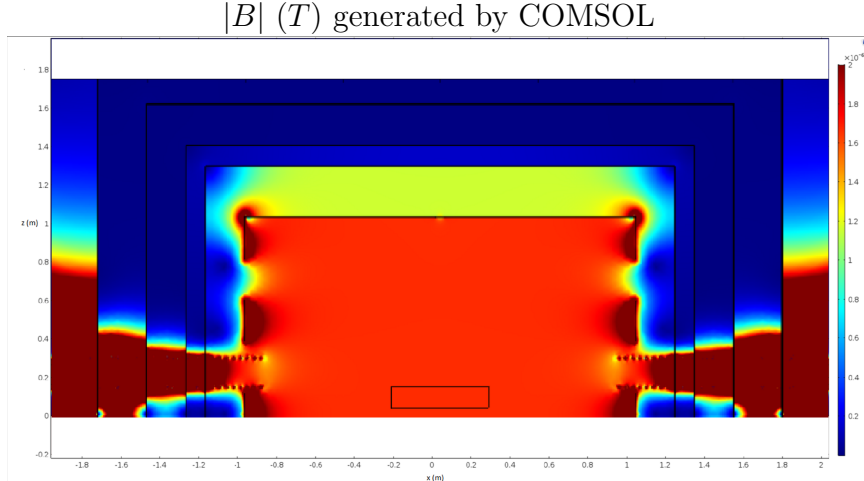


Figure 4.9: Plot of $|B|$ generated by COMSOL on the $y = 0$ plane. This COMSOL model contains a previous iteration of the B_0 and spin-transport coil designs. This plot illustrates the spin-transport field at the MuMetal surface due to the single layer (i.e. not self-shielding) spin-transport coil design. The leakage field around the spin-transport coils should be compared to Fig. 4.6, which plots the same cross section for the modified double $\cos \theta$ spin-transport design.

A small volume is added in the neutron guide near the guide stop to act as a neutron source or neutron “detector” depending on the simulation. Note that a single cell and neutron guide are used for the simulation geometry. Indeed, the simulation only considers the upper storage cell with the assumption that the transport efficiency will be equivalent for the UCN populations stored in each cell.

The various states of the apparatus (i.e. fill, store, and dump) are realized in the software by switching geometries to active or inactive (See Fig. 4.11). For example, the storage volume is set to a closed state by instantaneously replacing the joined guide and storage cell geometry with the storage cell geometry. In the physical apparatus, the storage cells are closed by translating a plug into the open surface through which the neutrons enter. This moving object can affect the UCN energy distribution by accelerating the neutrons that are reflected from its surface, as is seen during the trap door actuation in the UCN τ experiment [39]. The possible interaction between neutrons and moving surfaces is not captured in the simulation.

The material properties assigned to the geometry include the Fermi potential (both real and imaginary components), a diffuse reflection probability, and a spin-flip probability. For the neutron guide and storage cell, the Fermi potential used in the simulation is $V_{walls} = 1000 \text{ neV}$, which is chosen to be much larger than the UCN kinetic energy to prevent neutrons being transmitted through the material surface. The neutron guide and cell walls have a diffuse reflection probability of 0.05 based on diffuse reflection probabilities measured in similar guides for UCN transport [68, 69]. The detector volume is assigned a Fermi potential $V_{det} = i1000 \text{ neV}$ to ensure that all neutrons incident on the detector are absorbed. The spin-flip probability is set to zero for all materials such that the only source of UCN depolarization is

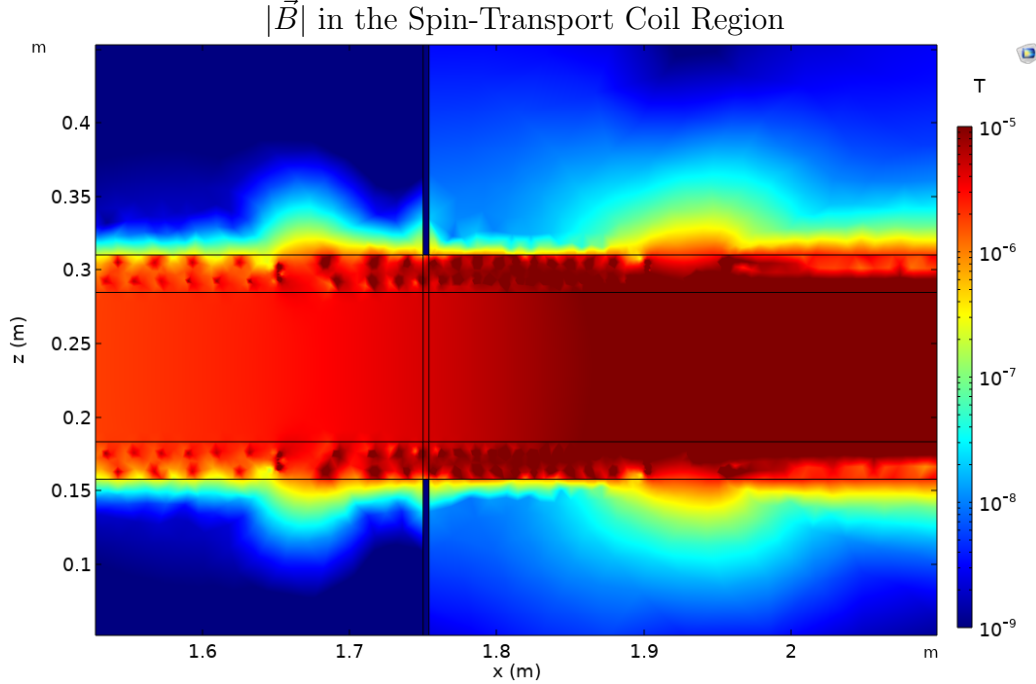


Figure 4.10: Plot of the magnetic field magnitude in the spin-transport coil region on the $y = 0$ plane. The color scale is logarithmic. The double $\cos \theta$ coil design is not perfectly self-shielding, as seen by the non-zero field outside of the surface, but, in general, the magnitude of the leakage field is order of magnitude smaller than the nominal applied field inside the coil volume. Local increases in leakage field exist at $x \approx 1.65$ m and $x \approx 1.9$ m. The source of the larger leakage field is the 0.5 mm gap between adjacent coils.

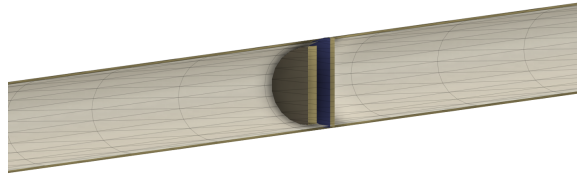
the interaction with the magnetic field. In addition to the materials assigned to the geometry derived from the STL files, a default material exists which is a sphere of vacuum. This sphere defines the world volume in which the simulation occurs, and neutrons that intersect the sphere boundary are absorbed.

The magnetic field for the spin-transport simulations are exported on a grid from a COMSOL model with the spin-transport coils, B_0 coil, and the MSR. The extent of the grid must exceed the volume accessible to the neutrons, which is the neutron guide and storage cell volume. PENTrack creates a continuous magnetic field via tricubic interpolation of each component in the loaded grid data [70]. The simulated neutron spins interact with the magnetic field via numerical integration of the well-known Bargmann-Michel-Telegdi (BMT) equation [71].

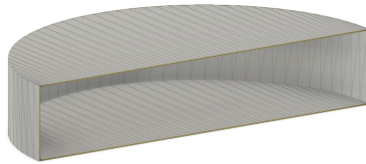
Simulation of the spin-transport efficiency occurs in two phases. The first phase is a simulation of the fill time. The neutrons are generated in the neutron guide source volume and propagate throughout the combined guide-cell volume for a time $T_{fill} = 25$ seconds. The initial velocity magnitude of each UCN is sampled from a v^2 distribution (see Fig. 4.12). Neutrons with kinetic energy $E > 160$ neV cannot be stored in the UCN cell volumes due to the deuterated polystyrene wall coating discussed in Section 2.2. Since all neutrons will be reflected by the simulated material,



(a) Guide-cell geometry with source volume and guide stop.



(b) Zoomed image showing the neutron source and guide stop.



(c) Closed cell geometry.

Figure 4.11: Geometry in PENTrack simulation.

the initial energy spectrum of the simulation should match the energy spectrum expected at the detector. Assuming the neutrons have equal potential energy at these two locations, the velocity distribution must then be equal. The velocity direction is sampled from a uniform spherical distribution. The neutron spins are represented with a normalized spin vector $|\vec{S}| = 1$, and the initial spin state is $S_z = 1$. At time $t = T_{fill}$, the cell-guide geometry is instantaneously replaced by the closed cell geometry. The neutrons that are not enclosed within the cell geometry will continue on a parabolic trajectory, under the influence of gravity, until they contact the outer surface of the world volume. These events will be labeled as “hit outer boundaries”. The neutrons contained by the cell geometry will continue to propagate in the closed cell. The simulation time continues for an additional 25 seconds to guarantee all non-stored neutrons contact the outer boundary. The simulation is completed at $t = 50$ seconds. All of the neutrons in the cell will be labeled “did not finish” due to the fact that the neutrons were simulated for the full 50 second simulation time.

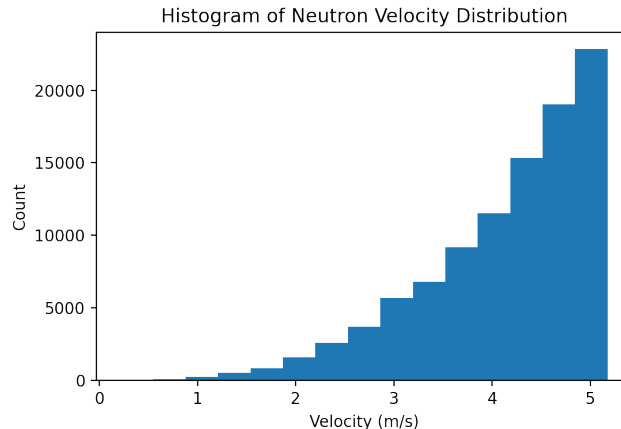


Figure 4.12: Histogram of initial neutron velocities from PENTrack.

The second phase of the transport efficiency simulation is the unload time. The neutrons begin in the cell volume and propagate to the detector at the end of the neutron guide. The detector in this simulation is the same geometry as the source from the first phase. The source volume in phase two is the interior of the storage cell volume, in which PENTrack will randomly assign the UCN initial positions. The initial velocities are chosen using the same method as phase one. The initial spin state of each neutron is also $S_z = 1$. In phase two, the guide-cell geometry and detector geometry are active for the full simulation length. Neutrons propagate throughout the guide-cell volume and, at any time, may come into contact with the detector surface. When this occurs, the neutron is absorbed by the detector and labeled “absorbed in bulk material”, and these neutrons will be considered detected. The unload simulation time is $T_{unload} = 25$ seconds. Neutrons which have not intersected the detector surface during the unload time, meaning they are still propagating throughout the guide-cell geometry, will be flagged as “did not finish”.

Results

The neutron population polarization P is defined as:

$$P = \frac{1}{N} \sum_{k=1}^N \frac{\vec{S}_k \cdot \vec{B}_k}{|\vec{B}_k|} \quad (4.9)$$

where N is the total number of neutrons, \vec{S}_k is the final state normalized spin vector of the k th neutron, and \vec{B}_k is the magnetic field at the final position of the k th neutron. At the final positions of the neutrons in each simulation, which is within the cell volume for Phase 1 and at the detector surface for Phase 2, the magnetic field is $\vec{B} \approx B_z \hat{z}$. Using this approximation in Eq.4.9, the polarization reduces to the average S_z of the neutron population:

$$P \approx \frac{1}{N} \sum_{k=1}^N S_{zk}$$

Since the initial polarization is defined to be $P_0 = 1$, the spin-transport efficiency of each phase is the final polarization of the neutron population, and the total spin-transport efficiency P_{trans} is the product of the efficiencies of each phase. Phase 1 and Phase 2 contain $N_0 = 10^5$ neutrons, but only those labeled as “did not finish” in Phase 1 and “absorbed in bulk material” in Phase 2 are considered in the respective polarization calculation.

Phase 1 completed with $N_1 = 6.5978 \times 10^4$ neutrons in the cell volume and a polarization $P_1 = 0.9184$ of the stored neutron population. In Phase 2, $N_2 = 5.8828 \times 10^4$ neutrons were “detected” with a polarization $P_2 = 0.9769$. Phase 2 has significantly less depolarization when compared with Phase 1. Under the assumption that most of the depolarization occurs in the spin-transport magnetic field, the dynamics of the neutrons during the two phases provides an explanation for the difference in final state polarization. Phase 1 provides 25 seconds of time for the neutrons to propagate in the guide-cell geometry. During this time, neutrons can make multiple passes through the spin-transport region, greatly increasing the interaction time with the spin-transport magnetic field. An example of this behavior is shown for an individual neutron in Fig. 4.14. Neutrons are far less likely to make multiple passes through the spin-transport magnetic field in Phase 2 because the detector absorbs neutrons at the end of the neutron guide, preventing reflection off of the guide stop toward the spin-transport region. Therefore, the interaction time of the neutrons with the spin-transport magnetic field in Phase 2 is small relative to Phase 1. The total spin-transport efficiency from these simulations is:

$$P_{trans} = P_1 P_2 = 0.89718$$

Recall the polarization product $\alpha = AP_{det}$ from Eq. 2.24 must satisfy $\alpha > 0.8$. Assuming the analyzing power of the detector is $A > 0.9$, the spin-transport magnetic field maintains the polarization necessary to achieve the specification.

Extensions of the Spin-Transport Simulation

The simulation work above served the purpose of validating the spin-transport coil system design. A number of assumptions and simplifications were made to simulate the system, which should be resolved using a higher fidelity simulation. This subsection discusses the assumptions in the completed simulation work and provides suggestions for exploration of associated effects, including extensions beyond spin-transport.

The neutron guide in the physical apparatus is approximately 4 m in length (measuring from the polarizing magnet to the center of the UCN storage cell), which is much longer than the guide implemented in the spin-transport simulation. The guide geometry imported into the simulation effectively has a length of 2.5 m determined by the position of the guide stop. The missing ~ 1.5 m portion of neutron guide is not considered in the simulation because the applied magnetic field in this region is large enough to provide adiabatic transport of the neutron spins with negligible depolarization. Simulating with a longer neutron guide, holding the simulation time constant, will result in improved spin-transport efficiency because the neutron interaction time with the field taper region will be smaller. Naturally, neutrons will have to travel a

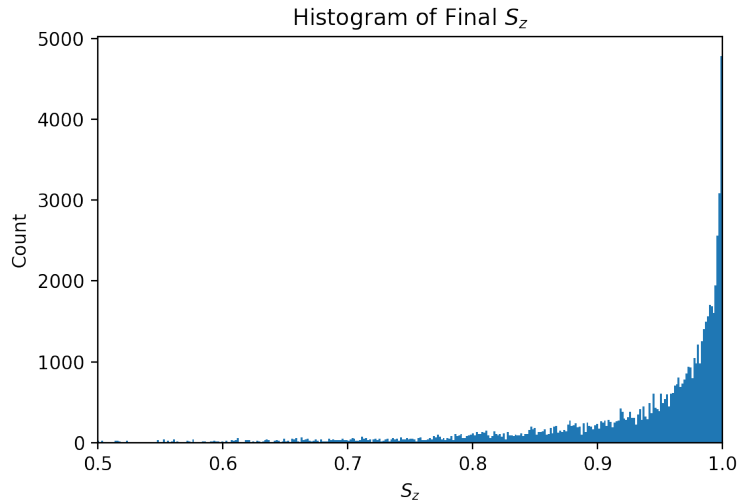


Figure 4.13: Histogram showing the z -component of the simulated neutron spin vector from Phase 2. Only the detected neutrons are shown in the histogram, and S_z is recorded when the neutrons contact the detector volume.

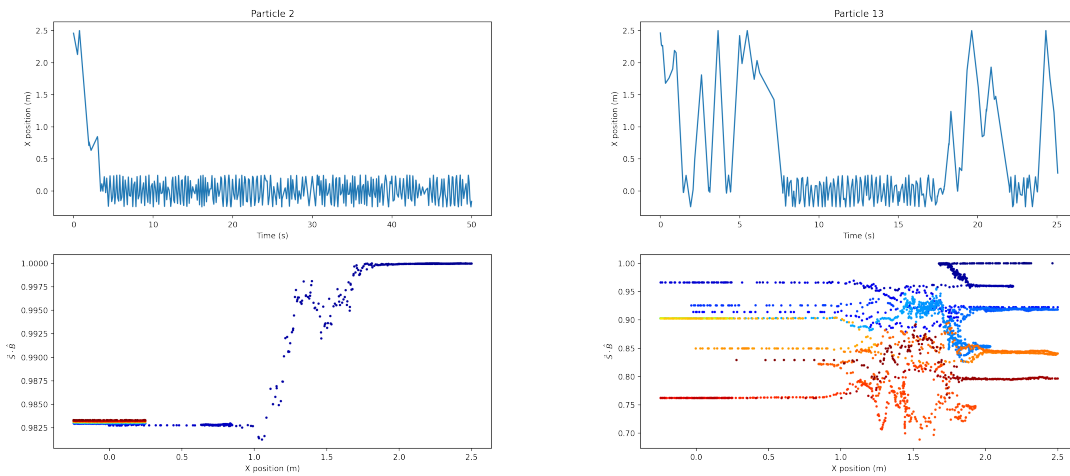


Figure 4.14: The plots represent two individual neutrons simulated during Phase 1: particle 2 (LEFT) and particle 13 (RIGHT). These two particles were chosen to show some representative behavior of the simulated neutrons. The top two plots show the x position of the simulated neutron during the full simulation time. The bottom two plots are scatter plots of the spin alignment of the neutron with the magnetic field. The color represents time with $t = 0$ being dark blue and t_{end} being dark red.

farther distance to traverse the guide system and make multiple passes through the spin-transport magnetic field, except in the case of diffuse reflection reversing the projection of neutron velocity onto the guide axis.

The shape of the guide should also be addressed. In the simulation work presented, the guide geometry is a straight tube at a nominal height that feeds into the storage cell volume. The neutron guide system in the physical apparatus contains two 45° bends, providing an offset of the guide position in the y direction so that the guides can exit through the MSR penetration. The presence of these bends could affect the transmission of neutrons from the beginning of the guide into the cell volume, possibly changing the number of times a neutron traverses the spin-transport region. For the current simulation setup, one would expect the guide bends to have negligible effect on the final polarization because any reduction of transmission into the cell volume would be complimented by a reduced transmission of neutrons from the cell volume back into the spin-transport region. However, the proper guide geometry should be included for completeness. Precise knowledge of the material surface is key for accurate modeling of diffuse reflection and, therefore, transmission through the neutron guide.

The simulation includes a single neutron guide and storage cell, namely the upper guide and cell. The spin-transport efficiency results are assumed to apply to both the upper and lower sections of the apparatus, but there exists a vertical displacement between these two sections. Since the neutrons in the upper section will have more gravitational potential energy, the neutrons in the lower section are expected to have greater velocity. The potential energy due to the 0.47 m height difference between neutrons in the lower and upper guide is 47.94 neV. To accurately capture these energy effects, one should incorporate the full system of upper and lower guides and cells. This should include activating a single neutron source that feeds the upper and lower guides via a “Y” just downstream from the polarizing magnet. When considering energy effects, the Fermi potentials applied to the simulated materials should be assigned precisely for the coatings employed in the apparatus, i.e. nickel phosphorus and deuterated polystyrene. The initial kinetic energy distribution of the neutrons should match the distribution coming from the source rather than the distribution measured at the detector, allowing for the material interactions to generate the detected neutron energy distribution.

Modeling the guide in this way allows for neutrons to be generated across a period of time. All neutrons in the spin-transport simulation were generated at time $t = 0$. Thus, all the neutrons were free to propagate through the system for the full 25 second fill time. As discussed above, the expected fill time for the apparatus is ~ 50 seconds but not all neutrons will pass through the polarizing magnet the instant that the neutron beam valve is opened. The neutrons will continue to enter the system until the beam valve is closed. The simulation neutron source should replicate the time dependent neutron flux as closely as possible to accurately simulate the UCN interaction time with the spin-transport region. The UCN flux and initial energy spectrum at the LANL-nEDM beamline are discussed in [72].

A detailed spin-transport simulation that implements the suggested improvements can be combined with a Ramsey sequence and the introduction of an electric field to

construct a full-cycle simulation. A high fidelity simulation of the apparatus through a measurement cycle is a necessity for understanding and controlling systematic effects, such as gravitational depolarization [73]. Other sources of depolarization (wall collisions, magnetic impurities, leakage current in the HV electrodes, etc.) can be included in the simulation to produce an expected polarization at the detector P_{det} . PENTrack allows for the magnetic fields to be defined analytically. Therefore, the simulation can combine “perfect” magnetic fields with modeled or measured fields as a mechanism for selectively studying systematic effects related to a single magnetic field source.

4.4 Prototype coils

Single Layer Coil

A modified $\cos \theta$ coil was fabricated to validate the COMSOL models of the spin transport coils and demonstrate the efficacy of 3D-printed coil forms (see Fig. 4.15 for pictures). The prototype coil has a 20 cm diameter and 25 cm length. As it is a single layer coil with open end caps, the wires are wound only on the outer surface and the annulus of the cylindrical coil. The 3D printing technique allows for grooves to be constructed in the coil form, which allows for precise winding of complex wire patterns. A traditional $\cos \theta$ coil will produce a uniform field. This modified $\cos \theta$ coil is one coil in a set of four coils designed to produce a magnetic field which increases in magnitude across the length of the coil set—similar to the double $\cos \theta$ coil set presented in the previous section. The plot in Fig. 4.16 shows B_z along the axis of the coil, where z is the nominal field direction. The field produced by the coil (the blue scatter plot) agrees with the predicted field extracted from the COMSOL model (the black line). Notice that the field magnitude does not increase monotonically along the axis of the coil, which is expected since the full set of coils is not present.

Double Cos θ Prototype

A double $\cos \theta$ coil was fabricated to test the “self-shielding factor” and the spin-transport interface with the B_0 coil. The coil geometry is a cylindrical shell with inner radius $R_{in} = 3.4$ cm, outer radius $R_{out} = 4.6$ cm, and length $L = 30$ cm. The winding pattern for the prototype coil was produced using the magnetic scalar potential method in COMSOL as explained in Section 4.1. The self-shielding factor is defined as the ratio of the magnetic field magnitude on the axis of the cylindrical coil to the magnetic field magnitude 1 cm from the outer surface of the coil. The coil has open end caps, so the field magnitude decreases near the ends of the coil compared to the relatively uniform magnitude at the center. Fig. 4.17 shows a plot of the field magnitude along the coil axis and along a parallel line at a radius $R = R_{out} + 1$ cm. The average self-shielding factor between $z = -10$ cm and $z = 10$ cm, calculated by taking a ratio of the two data points at each z position, was found to be 181.

A gapped solenoid with a square cross section was used as a stand-in B_0 coil to test the spin-transport interface. Each square solenoid consists of four PCB panels with

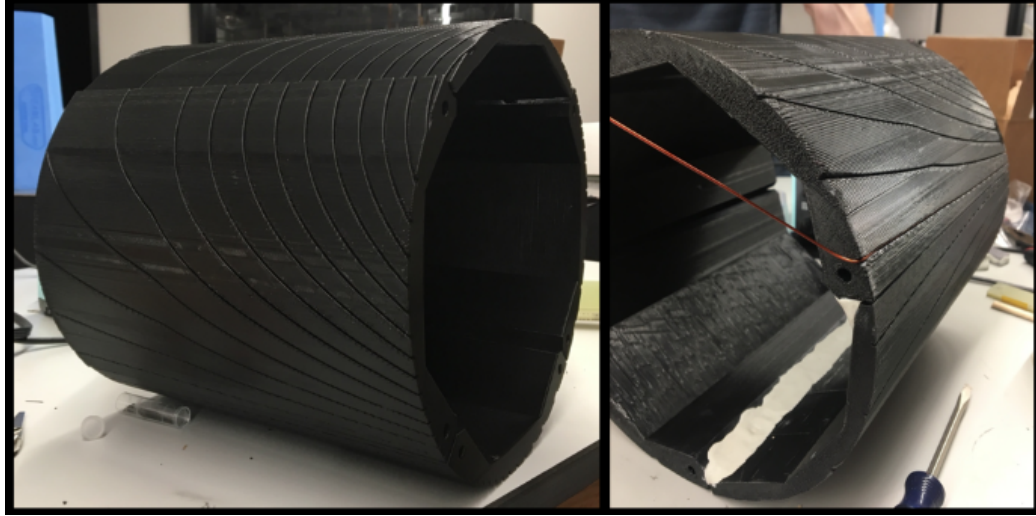


Figure 4.15: These images show the prototype modified $\cos \theta$ coil used to validate the design and fabrication techniques used for the spin-transport coils. The coil was wound using 20 gauge magnet wire placed in grooves to ensure precise placement. The coil was printed in quarters, divided into 90 degree sections. The left image features a misalignment of the upper most quadrant to illustrate the coil construction—note the resulting discontinuity in the groove pattern. In the right picture, a kink in the groove pattern is visible near the mid-plane of the cylinder. The source of the kink is the boundary condition enforced by the presence of a MSR shielding layer in the COMSOL model used to generate the winding pattern.

90° version of the compression B_0 corner connectors. Two square solenoids are stacked to form the gapped solenoid, with the coil axis aligned along z . A single face of the upper solenoid contains the rerouted winding pattern for the spin-transport interface, leaving a circular region void of traces. The winding pattern on the remaining PCB panels are horizontal traces. The prototype double $\cos \theta$ coil was attached to the gapped solenoid at the spin-transport interface position, i.e. the axis of the double $\cos \theta$ coil was centered on the circular rerouted winding region of the gapped solenoid face. The magnetic field was measured along a line parallel to the gapped solenoid axis at a distance of 2 cm from the spin-transport interface surface (see Fig. 4.18).

Without the rerouted current in the gapped solenoid, one would expect even symmetry in B_z and odd symmetry in B_x , using the center of the gapped solenoid as the origin. The rerouted current creates an asymmetry in these components, as seen in the red scatter plots in Fig 4.18. Exciting the double $\cos \theta$ coil with the proper current restores the symmetry to the magnetic field. Thus, the magnetic field produced inside the gapped solenoid by the rerouted gapped solenoid and double $\cos \theta$ coil is qualitatively equivalent to the field expected from a gapped solenoid without rerouted current. This testing justified further investigation into the design method of interfacing the spin-transport coils with the B_0 face in the LANL-nEDM apparatus. The quantitative support for the spin-transport interface efficacy is the modeled B_0 field uniformity and spin-transport efficiency using the combined B_0 and

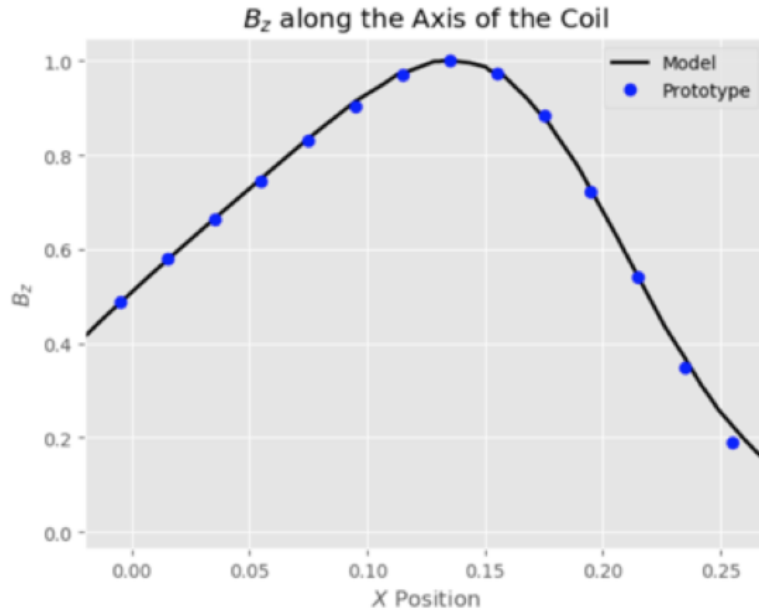


Figure 4.16: Plot of B_z along the axis of the prototype modified $\cos \theta$ coil shown in Fig. 4.15. The blue points are measurements of B_z collected via translation of a fluxgate magnetometer. The black line represents the expected result extracted from the COMSOL model of the prototype coil. The physical coil field profile is consistent with the COMSOL prediction.

Measured B field Magnitude from Double Cos θ Prototype

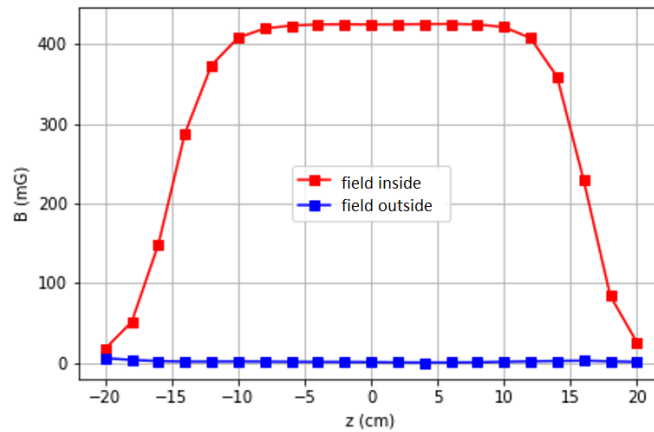


Figure 4.17: Plot of the double $\cos \theta$ prototype coil magnetic field magnitude [74]. The magnitude of the field along the coil axis (Red) is large compared to the field magnitude along a line parallel to the coil axis and 1 cm outside of the coil surface (Blue). The ratio of these two plots is the “self-shielding” factor of the coil. The average self-shielding factor from $z = -10$ cm to $z = 10$ cm is 181.

Magnetic Field Near the Spin-Transport Interface

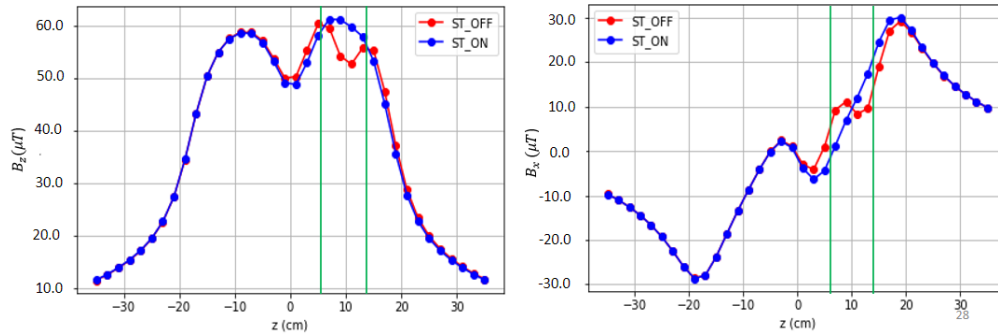


Figure 4.18: Plots of the magnetic field components near the spin-transport interface [74]. The vertical green lines centered around $z = 10$ cm represent the region spanned by the spin-transport diameter. The red scatter plot is the magnetic field from the stand-in B_0 coil. The blue scatter plot is the magnetic field from the B_0 and spin-transport coil system. The fluxgate magnetometer was translated parallel to the spin-transport interface surface with a 2 cm displacement from the coil surface.

spin-transport coil system to generate the modeled magnetic fields.

3D Printable Object Code

A python algorithm has been developed to generate 3D-printable coil forms with grooves for wire routing [75] such as the coils shown in Fig. 4.15. The code requires the user to input a folder of wire files (see Appendix B for an example wire file) and the PyMesh parameters to define the desired coil form. The first step in the process is to generate a mesh for the coil form, for example a cylindrical shell. PyMesh [76] is used to make this initial mesh as well as to perform Boolean operations on the mesh. The resolution of the mesh can be chosen based on the precision needed for the wire positions—this is intrinsically limited by the precision of the 3D printer employed. Next, the wire coordinates from each wire file are converted into a mesh. Since the inflated wires will later become the grooves in the coil form, a rectangular cross section is preferable for the wire mesh. Each coordinate in a given wire file is converted into a rectangle with the normal vector of the rectangle parallel to three dimensional path defined by the wire file, and the length of the rectangle is oriented along the normal vector of the coil form surface at that location. A re-sampling operation can be performed on the wire file to increase or decrease the resolution of the mesh generated. The wire meshes from the individual wire files are combined into a multi-wire mesh object using a Boolean union operation. Finally, the multi-wire mesh can be subtracted from the coil form to produce the grooves for the wires.

It may be desirable to create the coil form in multiple pieces to, for example, avoid potential print failure with long printing times or accommodate a smaller printing volume. The algorithm allows for the mesh to be divided along a defined plane for this purpose. For the clam-shell design implemented in the spin-transport coils shown above, the coils are separated into top and bottom halves. Alignment pegs are added

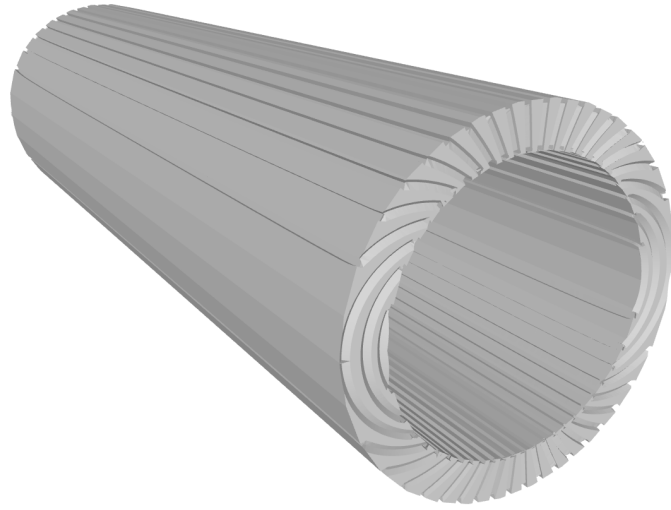


Figure 4.19: Example 3D coil object produced using the “Printable-coil” python algorithm [75].

to ensure that the two halves interface in a precise and predictable manner—this feature is recommended for all mating surfaces on a coil form.

Chapter 5 Conclusion

The LANL-nEDM experiment is one of several present generation neutron EDM searches occurring around the world. The success of the experiment relies on precise control of the magnetic field. This dissertation details the design work for two components of the LANL-nEDM magnetic field system—the B_0 coil and the spin-transport coils, including a subset of the prototyping work in support of the design effort for these coils.

The multi-split solenoid B_0 coil design has been shown, in FEA models, to meet the gradient specification of the LANL-nEDM experiment. Prototyping work has been completed to validate the design of novel features, e.g. the corner connectors allowing for modular assembly and the spin-transport interface. A half-scale B_0 prototype was fabricated and measured in a pre-existing MSR at LANL, which produced a linear gradient $\langle |\partial B_z / \partial z| \rangle < 0.3$ nT/m (scaling such that $|B_0| = 1$ μ T) along the axis of the coil. The full-scale coil has been fabricated and assembled within the apparatus, and analysis of the B_0 field profile is ongoing.

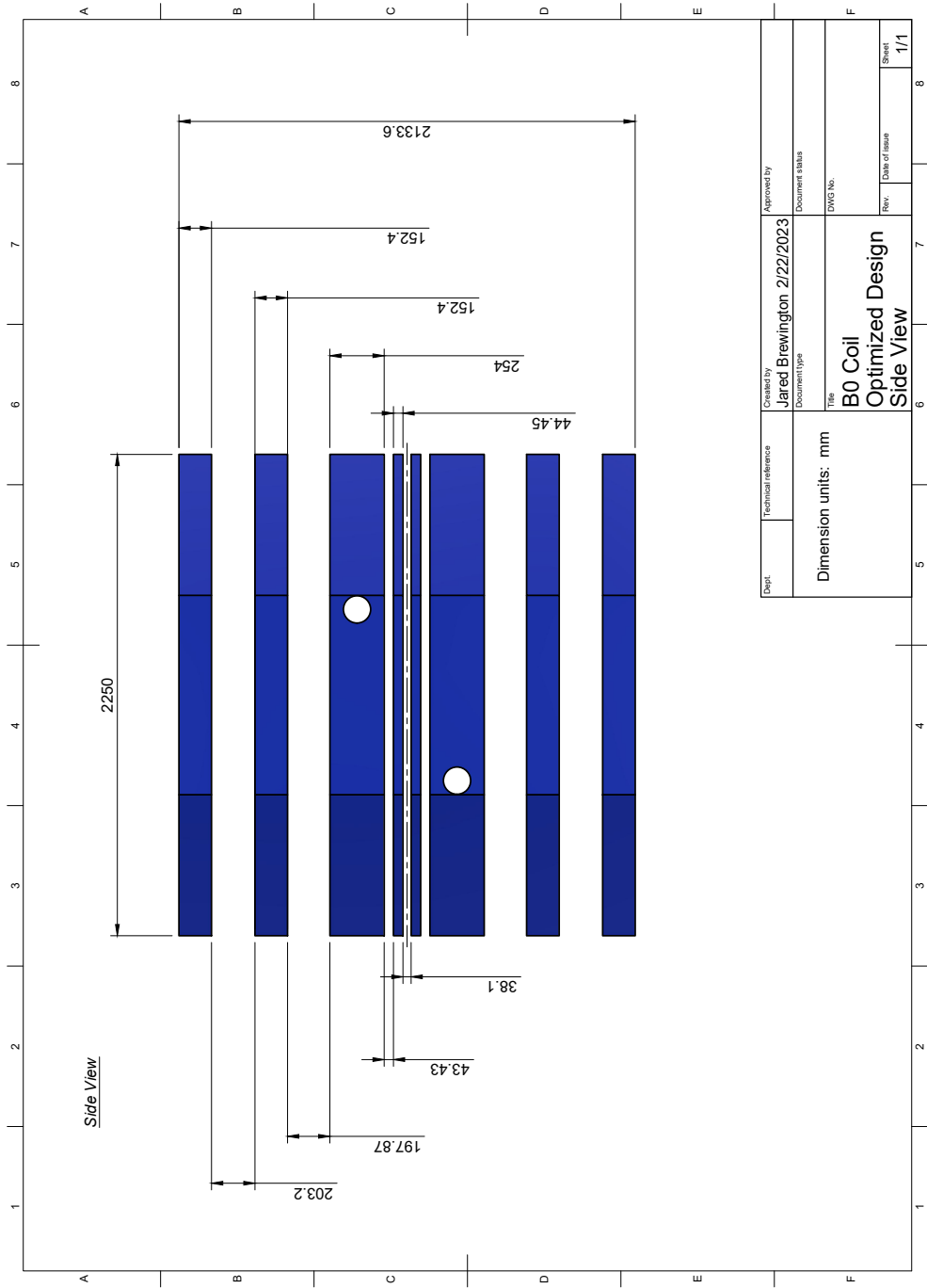
The spin-transport coil design has been validated in spin-tracking simulations using FEA to model the expected magnetic field. The simulation results show an 89.7% polarization transport efficiency, which would satisfy the polarization product specification $\alpha = AP_{det} > 0.8$ for analyzing power $A > 0.9$. An algorithm was developed using Python to create cylindrical coil forms with grooves for complex wire winding patterns. This algorithm was implemented to produce multiple prototype coils as well as the full-scale spin-transport coil system. The system of spin-transport coils has been installed in the LANL-nEDM apparatus, and the transport efficiency will be measured in the upcoming accelerator run cycle at LANL.

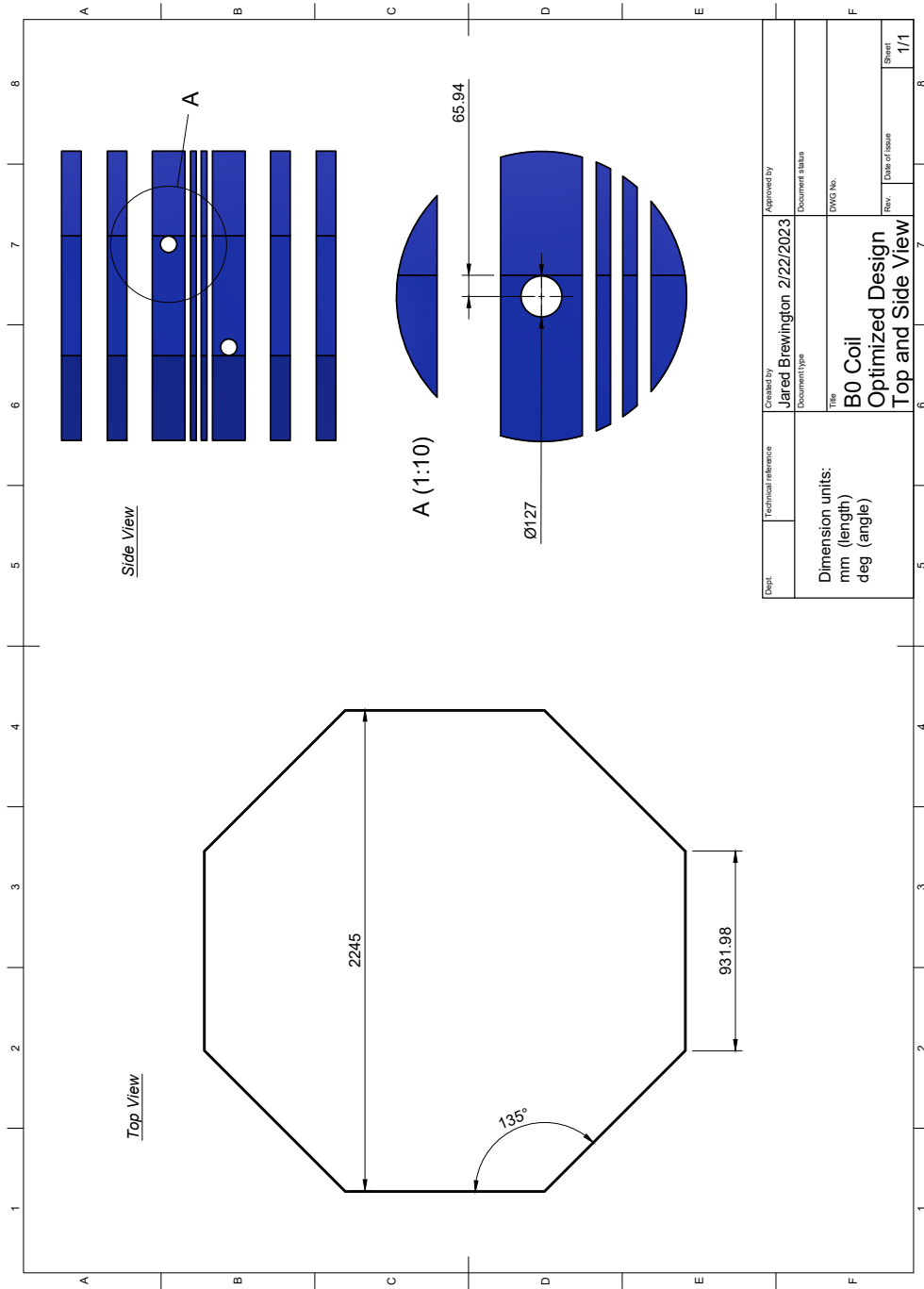
Future work associated with the B_0 coil and spin-transport coils will be completed by the research group at the University of Kentucky, led by Dr. Brad Plaster. This work will involve extensive mapping and analysis of the magnetic field produced by these coils, full-cycle particle-tracking simulations using modeled and measured magnetic field maps, and implementation of upgrades based on further modeling and experience operating the apparatus.

Appendices

Appendix A

Technical drawing of the optimized B_0 coil geometry.





Dept.	Technical reference	Created by	Approved by
		Lared Brewington 2/22/2023	
		Document type	Document status
		File	DWG No.
		B0 Coil	
		Optimized Design	
		Top and Side View	
		Rev.	Date of issue
			1/1
			Sheet
			1/1

Appendix B

Below is list of vertices from a wire file for Coil A. Such a file is used for all spin-transport wires to create current paths in FEA modeling and grooves in the 3D printed coil forms. The density of points has been decreased for the purposes of this example.

X	Y	Z
-0.750000	-0.035200	-0.046622
-0.750000	-0.034301	-0.049942
-0.750000	-0.033277	-0.052632
-0.750000	-0.031737	-0.055669
-0.750000	-0.030181	-0.058178
-0.750000	-0.027861	-0.061298
-0.750000	-0.025198	-0.064235
-0.750000	-0.022595	-0.066593
-0.748238	-0.020471	-0.068109
-0.744249	-0.020104	-0.068219
-0.740200	-0.020052	-0.068234
-0.736522	-0.020031	-0.068241
-0.732199	-0.020033	-0.068239
-0.728274	-0.020058	-0.068232
-0.723481	-0.020128	-0.068211
-0.719644	-0.020189	-0.068193
-0.715031	-0.020286	-0.068164
-0.710377	-0.020395	-0.068132
-0.705169	-0.020524	-0.068093
-0.700267	-0.020655	-0.068053
-0.695061	-0.020800	-0.068009
-0.689506	-0.020953	-0.067962
-0.684860	-0.021084	-0.067921
-0.680972	-0.021196	-0.067888
-0.676638	-0.021307	-0.067852
-0.673172	-0.021402	-0.067823
-0.669978	-0.021488	-0.067796
-0.666756	-0.021570	-0.067770
-0.663637	-0.021647	-0.067745
-0.659659	-0.021763	-0.067708
-0.655840	-0.021886	-0.067669
-0.652947	-0.022075	-0.067606
-0.650250	-0.022980	-0.067080
-0.650250	-0.025347	-0.065015
-0.650250	-0.027351	-0.062955
-0.650250	-0.029316	-0.060570
-0.650250	-0.031200	-0.057878

-0.650250	-0.032928	-0.054830
-0.650250	-0.034195	-0.052084
-0.650250	-0.035403	-0.048711
-0.650656	-0.036184	-0.045865
-0.653853	-0.036278	-0.045789
-0.657396	-0.036311	-0.045765
-0.660459	-0.036311	-0.045764
-0.663638	-0.036302	-0.045771
-0.667023	-0.036284	-0.045785
-0.670956	-0.036259	-0.045805
-0.675311	-0.036226	-0.045831
-0.679292	-0.036190	-0.045858
-0.684181	-0.036145	-0.045896
-0.690420	-0.036080	-0.045947
-0.694580	-0.036036	-0.045982
-0.698847	-0.035991	-0.046016
-0.703197	-0.035940	-0.046055
-0.707815	-0.035885	-0.046099
-0.712050	-0.035836	-0.046137
-0.715137	-0.035800	-0.046164
-0.718634	-0.035763	-0.046194
-0.721958	-0.035721	-0.046224
-0.725968	-0.035675	-0.046261
-0.730282	-0.035625	-0.046300
-0.734517	-0.035574	-0.046338
-0.738836	-0.035520	-0.046377
-0.742724	-0.035468	-0.046421
-0.747257	-0.035335	-0.046520
-0.750000	-0.035200	-0.046622

Copyright© Jared Brewington, 2023.

Bibliography

- [1] I. B. Khriplovich and A. R. Zhitnitsky. “What Is the Value of the Neutron Electric Dipole Moment in the Kobayashi-Maskawa Model?” In: *Phys. Lett. B* 109 (1982), pp. 490–492. DOI: 10.1016/0370-2693(82)91121-2.
- [2] C. Abel et al. “Measurement of the Permanent Electric Dipole Moment of the Neutron”. In: *Physical Review Letters* 124.8 (Feb. 2020). DOI: 10.1103/physrevlett.124.081803. URL: <https://doi.org/10.1103%5C%2Fphysrevlett.124.081803>.
- [3] E. M. Purcell and N. F. Ramsey. “On the Possibility of Electric Dipole Moments for Elementary Particles and Nuclei”. In: *Phys. Rev.* 78 (6 June 1950), pp. 807–807. DOI: 10.1103/PhysRev.78.807. URL: <https://link.aps.org/doi/10.1103/PhysRev.78.807>.
- [4] W. W. Havens, I. I. Rabi, and L. J. Rainwater. “Interaction of Neutrons with Electrons in Lead”. In: *Phys. Rev.* 72 (7 Oct. 1947), pp. 634–636. DOI: 10.1103/PhysRev.72.634. URL: <https://link.aps.org/doi/10.1103/PhysRev.72.634>.
- [5] J. H. Smith, E. M. Purcell, and N. F. Ramsey. “Experimental Limit to the Electric Dipole Moment of the Neutron”. In: *Phys. Rev.* 108 (1 Oct. 1957), pp. 120–122. DOI: 10.1103/PhysRev.108.120. URL: <https://link.aps.org/doi/10.1103/PhysRev.108.120>.
- [6] C. S. Wu et al. “Experimental Test of Parity Conservation in Beta Decay”. In: *Phys. Rev.* 105 (4 Feb. 1957), pp. 1413–1415. DOI: 10.1103/PhysRev.105.1413. URL: <https://link.aps.org/doi/10.1103/PhysRev.105.1413>.
- [7] T. D. Lee and C. N. Yang. “Question of Parity Conservation in Weak Interactions”. In: *Phys. Rev.* 104 (Oct. 1956), pp. 254–258. DOI: 10.1103/PhysRev.104.254. URL: <https://link.aps.org/doi/10.1103/PhysRev.104.254>.
- [8] Tanya S. Roussy et al. *A new bound on the electron’s electric dipole moment*. 2022. arXiv: 2212.11841 [physics.atom-ph].
- [9] E. Noether. “Invariante Variationsprobleme”. ger. In: *Nachrichten von der Gesellschaft der Wissenschaften zu Göttingen, Mathematisch-Physikalische Klasse* 1918 (1918), pp. 235–257. URL: <http://eudml.org/doc/59024>.
- [10] C. Geng and Leigeng. “SOME TESTS ON CPT INVARIANCE”. In: *Modern Physics Letters A* 22 (Nov. 2011). DOI: 10.1142/S0217732307023250.
- [11] David J Griffiths. *Introduction to Elementary Particles; 2nd rev. version*. Physics textbook. New York, NY: Wiley, 2008. URL: <https://cds.cern.ch/record/111880>.

- [12] Marco S Sozzi. *Discrete symmetries and CP violation: from experiment to theory*. Oxford graduate texts. New York, NY: Oxford Univ. Press, 2008. DOI: 10.1093/acprof:oso/9780199296668.001.0001. URL: <https://cds.cern.ch/record/1087897>.
- [13] R. E. Marshak. “The pain and joy of a major scientific discovery”. In: *Current Science* 63.2 (1992), pp. 60–64. ISSN: 00113891. URL: <http://www.jstor.org/stable/24095421> (visited on 04/19/2023).
- [14] R. P. Feynman and M. Gell-Mann. “Theory of the Fermi Interaction”. eng. In: *Physical review* 109.1 (1958), pp. 193–198. ISSN: 0031-899X.
- [15] J. H. Christenson et al. “Evidence for the 2π Decay of the K_2^0 Meson”. In: *Phys. Rev. Lett.* 13 (4 July 1964), pp. 138–140. DOI: 10.1103/PhysRevLett.13.138. URL: <https://link.aps.org/doi/10.1103/PhysRevLett.13.138>.
- [16] Gerhart Luders. “On the Equivalence of Invariance under Time Reversal and under Particle-Antiparticle Conjugation for Relativistic Field Theories”. In: *Kong. Dan. Vid. Sel. Mat. Fys. Med.* 28N5.5 (1954), pp. 1–17.
- [17] W Pauli. “Exclusion Principle, Lorentz Group, and reversal of space-time and charge”. In: *Niels Bohr and the Development of Physics, W. Pauli (ed.) New York: Pergamon* (1955).
- [18] O. W. Greenberg. “mml:math xmlns:mml=”<http://www.w3.org/1998/Math/MathML>” display=”inline”mml:miC/mml:mimml:miP/mml:mimml:miT/mml:mi/mml:mathViolation Implies Violation of Lorentz Invariance”. In: *Physical Review Letters* 89.23 (Nov. 2002). DOI: 10.1103/physrevlett.89.231602. URL: <https://doi.org/10.1103/physrevlett.89.231602>.
- [19] A. S. Beach et al. “Measurement of the Cosmic-Ray Antiproton-to-Proton Abundance Ratio between 4 and 50 GeV”. In: *Physical Review Letters* 87.27 (Dec. 2001). DOI: 10.1103/physrevlett.87.271101. URL: <https://doi.org/10.1103/physrevlett.87.271101>.
- [20] P. Barry. “The Hunt for Antihelium”. In: *Science News* 171 (2007), p. 296.
- [21] A. D. Sakharov. “Violation of CP Invariance, C asymmetry, and baryon asymmetry of the universe”. In: *Pisma Zh. Eksp. Teor. Fiz.* 5 (1967), pp. 32–35. DOI: 10.1070/PU1991v034n05ABEH002497.
- [22] T. William Donnelly et al. *Foundations of Nuclear and Particle Physics*. Cambridge University Press, 2017. DOI: 10.1017/9781139028264.
- [23] Hooman Davoudiasl and Rabindra N Mohapatra. “On relating the genesis of cosmic baryons and dark matter”. In: *New Journal of Physics* 14.9 (Sept. 2012), p. 095011. DOI: 10.1088/1367-2630/14/9/095011. URL: <https://doi.org/10.1088/1367-2630/14/9/095011>.
- [24] W-M Yao et al. “Review of Particle Physics”. In: *Journal of Physics G: Nuclear and Particle Physics* 33.1 (July 2006), pp. 1–1232. DOI: 10.1088/0954-3899/33/1/001. URL: <https://doi.org/10.1088/0954-3899/33/1/001>.

- [25] E. P. Shabalin. “THE ELECTRIC DIPOLE MOMENT OF THE NEUTRON IN A GAUGE THEORY”. In: *Sov. Phys. Usp.* 26 (1983), p. 297. DOI: 10.1070/PU1983v026n04ABEH004331.
- [26] T. E. Chupp et al. “Electric dipole moments of atoms, molecules, nuclei, and particles”. In: *Reviews of Modern Physics* 91.1 (Jan. 2019). ISSN: 1539-0756. DOI: 10.1103/revmodphys.91.015001. URL: <http://dx.doi.org/10.1103/RevModPhys.91.015001>.
- [27] Shahida Dar. “The Neutron EDM in the SM: A Review”. In: (Aug. 2000). arXiv: [hep-ph/0008248](https://arxiv.org/abs/hep-ph/0008248).
- [28] R. D. Peccei and Helen R. Quinn. “CP Conservation in the Presence of Instantons”. In: *Phys. Rev. Lett.* 38 (1977), pp. 1440–1443. DOI: 10.1103/PhysRevLett.38.1440.
- [29] P. A. R. Ade et al. “Planck2015 results”. In: *Astronomy Astrophysics* 594 (Sept. 2016), A13. ISSN: 1432-0746. DOI: 10.1051/0004-6361/201525830. URL: <http://dx.doi.org/10.1051/0004-6361/201525830>.
- [30] Brian D. Fields et al. “Big-Bang Nucleosynthesis after Planck”. In: *Journal of Cosmology and Astroparticle Physics* 2020.03 (Mar. 2020), pp. 010–010. DOI: 10.1088/1475-7516/2020/03/010. URL: <https://doi.org/10.1088/1475-7516/2020/03/010>.
- [31] John Ellis. “Theory of the neutron electric dipole moment”. In: *Nuclear Instruments and Methods in Physics Research Section A: Accelerators, Spectrometers, Detectors and Associated Equipment* 284.1 (1989), pp. 33–39. ISSN: 0168-9002. DOI: [https://doi.org/10.1016/0168-9002\(89\)90243-X](https://doi.org/10.1016/0168-9002(89)90243-X). URL: <https://www.sciencedirect.com/science/article/pii/016890028990243X>.
- [32] W. B. Dress et al. “Search for an Electric Dipole Moment of the Neutron”. In: *Phys. Rev. D* 15 (1977), p. 9. DOI: 10.1103/PhysRevD.15.9.
- [33] Edgard Pierre. “Development and optimisation of a ultracold neutron polarizing system in the framework of a new measurement of the neutron electric dipole moment.” In: (Mar. 2012).
- [34] G. L. Greene et al. “MEASUREMENT OF THE NEUTRON MAGNETIC MOMENT”. In: *Phys. Rev. D* 20 (1979), pp. 2139–2153. DOI: 10.1103/PhysRevD.20.2139.
- [35] M. Tanabashi et al. “Review of Particle Physics”. In: *Phys. Rev. D* 98 (3 Aug. 2018), p. 030001. DOI: 10.1103/PhysRevD.98.030001. URL: <https://link.aps.org/doi/10.1103/PhysRevD.98.030001>.
- [36] James Ryan Dadisman. “MAGNETIC FIELD DESIGN TO REDUCE SYSTEMATIC EFFECTS IN NEUTRON ELECTRIC DIPOLE MOMENT MEASUREMENTS”. In: *Theses and Dissertations—Physics and Astronomy* 53 (2018). URL: https://uknowledge.uky.edu/physastron_etds/53.
- [37] P. G. Harris. *The Neutron EDM Experiment*. 2007. DOI: 10.48550/ARXIV.0709.3100. URL: <https://arxiv.org/abs/0709.3100>.

- [38] T. M. Ito et al. “Performance of the upgraded ultracold neutron source at Los Alamos National Laboratory and its implication for a possible neutron electric dipole moment experiment”. In: *Physical Review C* 97.1 (Jan. 2018). DOI: 10.1103/physrevc.97.012501. URL: <https://doi.org/10.1103%5C%2Fphysrevc.97.012501>.
- [39] F.M. Gonzalez et al. “Improved Neutron Lifetime Measurement with UCN τ ”. In: *Physical Review Letters* 127.16 (Oct. 2021). DOI: 10.1103/physrevlett.127.162501. URL: <https://doi.org/10.1103%5C%2Fphysrevlett.127.162501>.
- [40] M. A.-P. Brown et al. “New result for the neutron β -asymmetry parameter A_0 from UCNA”. In: *Phys. Rev. C* 97 (3 Mar. 2018), p. 035505. DOI: 10.1103/PhysRevC.97.035505. URL: <https://link.aps.org/doi/10.1103/PhysRevC.97.035505>.
- [41] LANL-nEDM Collaboration. “Technical Progress Report for a Search for the Neutron Electric Dipole Moment at the Los Alamos National Laboratory Ultracold Neutron Source”. In: (2017).
- [42] B. Graner et al. “Reduced Limit on the Permanent Electric Dipole Moment of ^{199}Hg ”. In: *Physical Review Letters* 116.16 (Apr. 2016). DOI: 10.1103/physrevlett.116.161601. URL: <https://doi.org/10.1103%5C%2Fphysrevlett.116.161601>.
- [43] G. Ban et al. “Demonstration of sensitivity increase in mercury free-spin-precession magnetometers due to laser-based readout for neutron electric dipole moment searches”. In: *Nuclear Instruments and Methods in Physics Research Section A: Accelerators, Spectrometers, Detectors and Associated Equipment* 896 (July 2018), pp. 129–138. DOI: 10.1016/j.nima.2018.04.025. URL: <https://doi.org/10.1016%5C%2Fj.nima.2018.04.025>.
- [44] C. A. Baker et al. “Improved Experimental Limit on the Electric Dipole Moment of the Neutron”. In: *Physical Review Letters* 97.13 (Sept. 2006). DOI: 10.1103/physrevlett.97.131801. URL: <https://doi.org/10.1103%5C%2Fphysrevlett.97.131801>.
- [45] J. M. Pendlebury et al. “Revised experimental upper limit on the electric dipole moment of the neutron”. In: *Phys. Rev. D* 92 (9 Nov. 2015), p. 092003. DOI: 10.1103/PhysRevD.92.092003. URL: <https://link.aps.org/doi/10.1103/PhysRevD.92.092003>.
- [46] Z. Chowdhuri et al. “Experimental study of ^{199}Hg spin anti-relaxation coatings”. In: *Applied Physics B* 115.2 (Aug. 2013), pp. 257–262. DOI: 10.1007/s00340-013-5598-8. URL: <https://doi.org/10.1007%5C%2Fs00340-013-5598-8>.
- [47] J. M. Pendlebury et al. “Geometric-phase-induced false electric dipole moment signals for particles in traps”. In: *Phys. Rev. A* 70 (3 Sept. 2004), p. 032102. DOI: 10.1103/PhysRevA.70.032102. URL: <https://link.aps.org/doi/10.1103/PhysRevA.70.032102>.

- [48] Alina Aleksandrova. “Magnetic Field Monitoring in the SNS Neutron EDM Experiment”. In: *Theses and Dissertations—Physics and Astronomy* 68 (2019). URL: https://uknowledge.uky.edu/physastron_etds/68/.
- [49] Norman F. Ramsey. “Resonance Transitions Induced by Perturbations at Two or More Different Frequencies”. In: *Phys. Rev.* 100 (4 Nov. 1955), pp. 1191–1194. DOI: 10.1103/PhysRev.100.1191. URL: <https://link.aps.org/doi/10.1103/PhysRev.100.1191>.
- [50] Douglas D. McGregor. “Transverse relaxation of spin-polarized ^3He gas due to a magnetic field gradient”. In: *Phys. Rev. A* 41 (5 Mar. 1990), pp. 2631–2635. DOI: 10.1103/PhysRevA.41.2631. URL: <https://link.aps.org/doi/10.1103/PhysRevA.41.2631>.
- [51] V.I. Luschnikov and Yu.V. Taran. “On the calculation of the neutron adiabatic spin-flipper”. In: *Nuclear Instruments and Methods in Physics Research Section A: Accelerators, Spectrometers, Detectors and Associated Equipment* 228.1 (1984), pp. 159–160. ISSN: 0168-9002. DOI: [https://doi.org/10.1016/0168-9002\(84\)90025-1](https://doi.org/10.1016/0168-9002(84)90025-1). URL: <https://www.sciencedirect.com/science/article/pii/0168900284900251>.
- [52] Dmitry Budker and Michael Romalis. “Optical magnetometry”. In: *Nature Physics* 3.4 (Apr. 2007), pp. 227–234. DOI: 10.1038/nphys566. URL: <https://doi.org/10.1038%5C%2Fnphys566>.
- [53] John David Jackson. *Classical electrodynamics*. 3rd ed. New York, NY: Wiley, 1999. ISBN: 9780471309321. URL: <http://cdsweb.cern.ch/record/490457>.
- [54] David J Griffiths. *Introduction to electrodynamics*. Pearson, 2013.
- [55] Milan Wayne Garrett. “Axially Symmetric Systems for Generating and Measuring Magnetic Fields. Part I”. In: *Journal of Applied Physics* 22.9 (1951), pp. 1091–1107. DOI: 10.1063/1.1700115. eprint: <https://doi.org/10.1063/1.1700115>. URL: <https://doi.org/10.1063/1.1700115>.
- [56] M.J. Cunningham. “Gapped solenoid as a means of producing a highly uniform magnetic field over an extended volume”. English. In: *Proceedings of the Institution of Electrical Engineers* 121 (12 Dec. 1974), 1589–1593(4). ISSN: 0020-3270. URL: <https://digital-library.theiet.org/content/journals/10.1049/piee.1974.0329>.
- [57] Y. Sakamoto et al. “Development of high-homogeneity magnetic field coil for ^{129}Xe EDM experiment”. In: *Hyperfine Interactions* 230.1-3 (Apr. 2015), pp. 141–146. DOI: 10.1007/s10751-014-1109-5.
- [58] P. Hammond. “Electric and magnetic images”. English. In: *Proceedings of the IEE - Part C: Monographs* 107 (12 Sept. 1960), 306–313(7). ISSN: 0369-8904. URL: <https://digital-library.theiet.org/content/journals/10.1049/pi-c.1960.0047>.

- [59] Aritro Pathak. “An elementary argument for the magnetic field outside a solenoid”. In: *European Journal of Physics* 38.1 (Nov. 2016), p. 015201. DOI: 10.1088/0143-0807/38/1/015201. URL: <https://doi.org/10.1088%5C%2F0143-0807%5C%2F38%5C%2F1%5C%2F015201>.
- [60] Pasquale Arpaia et al. “Magnetic characterization of Mumetal[®] for passive shielding of stray fields down to the nano-Tesla level”. In: *Nuclear Instruments and Methods in Physics Research Section A: Accelerators, Spectrometers, Detectors and Associated Equipment* 988 (2021), p. 164904. ISSN: 0168-9002. DOI: <https://doi.org/10.1016/j.nima.2020.164904>. URL: <https://www.sciencedirect.com/science/article/pii/S0168900220313012>.
- [61] S. Sgobba. “Physics and measurements of magnetic materials”. In: (2011). DOI: 10.48550/ARXIV.1103.1069. URL: <https://arxiv.org/abs/1103.1069>.
- [62] N. Nouri and B. Plaster. “Systematic optimization of exterior measurement locations for the determination of interior magnetic field vector components in inaccessible regions”. In: *Nuclear Instruments and Methods in Physics Research Section A: Accelerators, Spectrometers, Detectors and Associated Equipment* 767 (2014), pp. 92–98. ISSN: 0168-9002. DOI: <https://doi.org/10.1016/j.nima.2014.08.026>. URL: <https://www.sciencedirect.com/science/article/pii/S0168900214009541>.
- [63] Palamure P.A. “LANL nEDM half scale B_0 prototype design and test of the field gradient inside a MSR at LANL”. 2021 Fall Meeting of the APS Division of Nuclear Physics. 2021. URL: <https://meetings.aps.org/Meeting/DNP21/Session/FE.2>.
- [64] C. B. Crawford. “The physical meaning of the magnetic scalar potential and its use in the design of hermetic electromagnetic coils”. In: *Review of Scientific Instruments* 92.12 (2021), p. 124703. DOI: 10.1063/5.0063054. eprint: <https://doi.org/10.1063/5.0063054>. URL: <https://doi.org/10.1063/5.0063054>.
- [65] M. Maldonado-Velázquez et al. “Magnetic field devices for neutron spin transport and manipulation in precise neutron spin rotation measurements”. In: *Nuclear Instruments and Methods in Physics Research Section A: Accelerators, Spectrometers, Detectors and Associated Equipment* 854 (May 2017), pp. 127–133. DOI: 10.1016/j.nima.2017.02.066. URL: <https://doi.org/10.1016%5C%2Fj.nima.2017.02.066>.
- [66] N. Nouri and B. Plaster. “Comparison of magnetic field uniformities for discretized and finite-sized standard cos, solenoidal, and spherical coils”. In: *Nuclear Instruments and Methods in Physics Research Section A: Accelerators, Spectrometers, Detectors and Associated Equipment* 723 (2013), pp. 30–35. ISSN: 0168-9002. DOI: <https://doi.org/10.1016/j.nima.2013.05.013>. URL: <https://www.sciencedirect.com/science/article/pii/S016890021300538X>.

- [67] W. Schreyer et al. “PENTTrack—a simulation tool for ultracold neutrons, protons, and electrons in complex electromagnetic fields and geometries”. In: *Nuclear Instruments and Methods in Physics Research Section A: Accelerators, Spectrometers, Detectors and Associated Equipment* 858 (June 2017), pp. 123–129. DOI: 10.1016/j.nima.2017.03.036. URL: <https://doi.org/10.1016%5C%2Fj.nima.2017.03.036>.
- [68] S. Ahmed et al. “First ultracold neutrons produced at TRIUMF”. In: *Phys. Rev. C* 99 (2 Feb. 2019), p. 025503. DOI: 10.1103/PhysRevC.99.025503. URL: <https://link.aps.org/doi/10.1103/PhysRevC.99.025503>.
- [69] S. Wločka et al. *Consistent description of UCN transport properties*. 2017. DOI: 10.48550/ARXIV.1701.07431. URL: <https://arxiv.org/abs/1701.07431>.
- [70] F. Lekien and J. Marsden. “Tricubic interpolation in three dimensions”. In: *International Journal for Numerical Methods in Engineering* 63.3 (2005), pp. 455–471. DOI: <https://doi.org/10.1002/nme.1296>. eprint: <https://onlinelibrary.wiley.com/doi/pdf/10.1002/nme.1296>. URL: <https://onlinelibrary.wiley.com/doi/abs/10.1002/nme.1296>.
- [71] Valentine Bargmann, Louis Michel, and VL Telegdi. “Precession of the polarization of particles moving in a homogeneous electromagnetic field”. In: *Physical Review Letters* 2.10 (1959), p. 435.
- [72] D. K. -T. Wong et al. *Characterization of the new Ultracold Neutron beamline at the LANL UCN facility*. 2022. DOI: 10.48550/ARXIV.2209.00003. URL: <https://arxiv.org/abs/2209.00003>.
- [73] P. G. Harris, J. M. Pendlebury, and N. E. Devenish. “Gravitationally enhanced depolarization of ultracold neutrons in magnetic-field gradients”. In: *Phys. Rev. D* 89 (1 Jan. 2014), p. 016011. DOI: 10.1103/PhysRevD.89.016011. URL: <https://link.aps.org/doi/10.1103/PhysRevD.89.016011>.
- [74] P.A. Palamure. personal communication. Jan. 10, 2023.
- [75] Jared Brewington. *printable_coil*. Version 1.0.0. Feb. 2022. URL: https://github.com/jaredBrewington/printable_coil.
- [76] PyMesh Development Team. *PyMesh*. 2022. URL: <https://github.com/PyMesh/PyMesh>.

Vita

Personal Information

Name: Jared Brewington
Place of Birth: Louisville, KY

Educational Institutions

M.S. Physics
University of Kentucky
November 2018

B.A Physics, Mathematics, and Psychology
Transylvania University
May 2016

Professional Positions

SCGSR Awardee
Department of Energy
Office of Science
November 2020 - November 2021

Graduate Research Assistant
University of Kentucky
Department of Physics and Astronomy
May 2017 - May 2022

Graduate Teaching Assistant
University of Kentucky
Department of Physics and Astronomy
August 2016 - December 2017